Subambient Passive Cooling Enabled by Polyethylene Aerogels

by

Arny Leroy

S.M. Mechanical Engineering
Massachusetts Institute of Technology, 2017

B.E. Mechanical Engineering
Polytechnique Montréal, 2015

Submitted to the Department of Mechanical Engineering in
Partial Fulfillment of the Requirements for the
Degree of Doctor of Philosophy in Mechanical Engineering
at the
MASSACHUSETTS INSTITUTE OF TECHNOLOGY
September 2021

©2021 Massachusetts Institute of Technology 2021
All rights reserved.

Author .....
Department of Mechanical Engineering
August 6th, 2021

Certified by .....
Evelyn N. Wang
Department Head of Mechanical Engineering
Thesis Supervisor

Accepted by .....
Nicolas Hadjiconstantinou
Professor of Mechanical Engineering
Chairman, Committee on Graduate Students

Subambient Passive Cooling Enabled by Polyethylene Aerogels

by

Arny Leroy

Submitted to the Department of Mechanical Engineering on August 6th, 2021
in Partial Fulfillment of the Requirements for the Degree of Doctor of Philosophy

Abstract

Subambient cooling is vital for promoting human health and well-being, driving sustainable economic growth, and minimizing food waste. Providing these benefits however, comes with major energetic and environmental costs. The over 1.6 billion air conditioning units currently in use around the world today already consume over 2000 TWh/year of electricity, or the equivalent of half the United States yearly electricity consumption, straining existing electrical systems and contributing to 3% of global CO_2 emissions. With growing space cooling demand stemming from economic and population growth in hot and developing parts of the world, more efficient air-conditioning and refrigeration systems are urgently needed.

One promising solution to help address existing and future global cooling challenges is to use passive cooling solutions such as passive radiative or evaporative cooling to provide electricity-free subambient refrigeration for food produce or to improve the efficiency of existing air conditioners and refrigerators. Passive radiative cooling relies on the rejection of naturally occurring infrared radiation emission of terrestrial objects to the cold (3 K) outer space through earth's transparent atmospheric spectral window (8-13 μm) to achieve passive cooling to subambient temperatures. On the other hand, evaporative cooling leverages the large enthalpy of vaporization of water, and the difference in water vapor concentration between a liquid surface and the ambient to generate high cooling power and subambient cooling. While promising, the cooling performance of these systems has traditionally suffered from important parasitic solar absorption during the day and parasitic heat gain from the warmer ambient air when operating at subambient temperatures. In this work, we propose to tackle these two longstanding challenges by optimizing and using polyethylene aerogel, a solar reflecting, infrared transparent, and vapor permeable thermal insulator, as a cover for radiative and evaporative coolers.

We first present the development, characterization, and optimization of polyethylene aerogels to achieve a low thermal conductivity material with high solar reflectance and infrared transmittance. We then

theoretically and experimentally investigate the benefits of using polyethylene aerogel covers in outdoor radiative coolers exposed to direct sunlight. We demonstrate significant passive cooling below the ambient temperature and high subambient cooling power over a continuous 24h period. Next, we show how ZnS nanoparticles inside polyethylene aerogel covers can help increase the solar reflectance of the cover, improving the daytime cooling performance of radiative coolers. Next, we propose a hybrid cooling architecture combining passive evaporative and radiative cooling, leveraging heat rejection mechanisms of both approaches to achieve lower subambient and higher cooling power passive cooling. Finally, we explore the potential impact of our proposed hybrid evaporative-radiative cooler in applications such as off-grid food produce storage and building air-conditioning and refrigeration systems. We show that our passive hybrid cooler can meaningfully extend the lifetime of perishable fruit and vegetables and provide important energy savings for cooling and refrigeration in commercial buildings across the United States with low water consumption. Successful development and commercialization of our hybrid cooling structure have the potential to reduce food-related wastes in developing countries while reducing building cooling energy and water consumption, and CO_2 emissions.

Thesis Committee:

Thesis Supervisor: Professor Evelyn N. Wang, Department of Mechanical Engineering

Professor Gang Chen, Department of Mechanical Engineering

Professor Leon Glicksman, Department of Mechanical Engineering

Professor Asegun Henry, Department of Mechanical Engineering

Acknowledgments

My years here at MIT as a PhD candidate have been a formidable time in my life from which I will keep many good memories. My experience here would however not have been the same or even possible without the support and help from all the people here at MIT and back home in Montréal. For that, I would like to express my sincere gratitude.

Evelyn N. Wang has been a formidable advisor and mentor to me throughout my six years at MIT. I cannot express how much she has contributed to my personal development, well-being, and success, making my time in the Device Research Laboratory such a memorable experience. Throughout the years, Evelyn always had the right balance between motivating and pushing me to do better and work harder and maintaining a healthy physical and mental health. And while she was always incredibly busy due to her dedication and commitment to the department and its students, Evelyn would always make time for her students showing how deeply she cared about us, our health, and our development. I could not have wished for a better advisor, and I am greatly thankful towards Evelyn for all what she has done.

My work would not have been possible without the valuable help, comments, and feedback from my thesis committee members Prof. Gang Chen, Prof. Leon Glicksman and Prof. Asegun Henry. I am grateful for their time and feedback during our committee meetings but also for their help outside the meetings. They often challenged my work and assumptions, forcing me to think more about the problems at hand and work hard to find solutions, which I think greatly helped improve the quality of my work.

Throughout my master's and PhD, Bikram Bhatia has been an exceptional mentor as well as a great friend. Bikram has dedicated a lot of his time towards the development of my critical thinking, my research skills, and my writing skills. Through our in-person meetings and more recently through our online Zoom meetings, Bikram has and continues to provide feedback and help on my work, significantly contributing to the success of my work and teaching me a lot of valuable personal and professional lessons. Without his mentorship, I would not have achieved and succeeded nearly as much, and for this, I am forever thankful. I truly believe that Bikram will make an excellent and successful professor and advisor.

Although not directly participating in this work, Michel Bernier was my research advisor during my undergraduate studies at Polytechnique Montréal. I am forever indebted to Michel for first believing in my potential, developing my research skills, mentoring me throughout my undergraduate studies, pushing me towards applying to graduate school at MIT, and guiding me through the admission process to the MIT graduate program.

I would also like to thank all the people in the Device Research Laboratory. Our interactions and discussions have greatly contributed to my personal development and the way I approach problems. Their invaluable advice, comments and questions have greatly helped me improve my work and my personal development and will certainly help me thrive in the future. Aside from lab work, they have also contributed to making some of my best memories here during the lab outings, camping trips, track workouts, and BBQs. Most notably, I would like to acknowledge David Bierman, Dion Antao, Kyle Wilke, Daniel John Preston, Yangying Zhu, Lin Zhao, Elise Strobach, Kyle Wilke, Colin Clancy Kelsall, Lenan Zhang, Geoffrey Vaartstra, Jay Sircar, Alina LaPotin, Chad Wilson, Cody Jacobucci and Carlos Diaz.

Playing in the MIT Hockey team with coaches Nick Sisler and Dave Hunter was another source of positive memories of my time here at MIT and gave me the opportunity to express my true Canadian self. I thank them for all their time, their patience, and the skills they have thought me.

The work presented in this thesis would not have been possible without the funding sources. I would like to acknowledge the support from the Singapore-MIT Alliance for Research and Technology (SMART), the MIT International Science and Technology Initiatives (MIST) and the Solid-State Solar Thermal Energy Conversion (S3TEC) Center, an Energy Frontier Research Center funded by the U.S. Department of Energy, Office of Science, Basic Energy Sciences under Award No. #DE-FG02-09ER46577.

I would also like to thank all my friends outside the lab. Peter Ascoli has been an awesome and understanding friend which whom I have shared many memorable experiences including our weekly chicken wings and beer, our raclette dinners, trips, and projects. Anna Rogers, Marlis Denk-Lobnig, Quantum Wei and Albert Gnadt were always there to support me, and I keep many good memories from our ski trips, raclette dinners, parties, and trips together. Finally, I would like to express my sincere gratitude to my friends back home in Montréal who were always supportive, interested, and excited about my work, giving me the motivation to continue and work harder.

Finally, most importantly, I owe everything I am to my family. All my life, my grandparents, my dad, my mom, and my brother have filled me with love and provided me with the support and guidance that I needed to reach my goals. My brother, through his exceptional intelligence, hard work, sense of humor and successes, has always been an example to me, and I am sure will continue to be. My dad has always pushed me to do better and work hard while supporting me. Baloo has been a nonstop source of love and comfort, and she has helped me remain healthy with her near infinite source of energy. After over ten years together, Maria continues to impress me and has been a source of inspiration, love, and comfort to me. Her hard work, her devotion, support, and understanding have helped myself and our relationship

through the most difficult times and she motivates me to pursue my objectives and succeed in life. Finally, my mom, aside from being the most caring, supporting, and loving parent, has thought me so many things in my life such as generosity, the importance of friends, love, caring for others and to always keep positive and smile. Throughout the years, she was always there for me, supporting and cheering me up while also showing interest in my life and my work, even giving suggestions for possible research paths. I could not have wished for a better mom, and for that I thank her. She will be forever missed, but I comfort myself in knowing that her positive energy and love will always remain.

Table of Contents

List of Figures

List of Tables

Chapter 1

1. Introduction

1.1. MOTIVATION

Subambient cooling is vital for minimizing food shortage, promoting human well-being, and driving sustainable economic growth. Yet, air-conditioning and refrigeration adoption in developing countries, where the need for cooling is often the highest, is still severely lacking compared to richer countries due to the high costs of such systems and the lack of reliable access to electricity [1]. And where air-conditioning is prevalent, the energy and environmental cost of using such systems is high, with no signs of waning down.

1.1.1. Space Cooling in Buildings

Today, over 1.6 billion air-conditioning systems are currently in use, bringing benefits to users' health, well-being and economic productivity [1]. Unfortunately, most of these air conditioners are inefficient, resulting in an annual worldwide electricity consumption of over 2000 TWh (half of current US total electricity consumption) and CO_2 emissions of over 1000 $MtCO_2$/year (3% of global CO_2 emissions) (see Figure 1a). With growing demand stemming from economic and population growth in hot and developing parts of the world, space cooling energy consumption is on a path to increase over three-fold by 2050 under existing and announced policies and energy efficiency targets (Figure 1a; dark blue line), while related CO_2 emissions are expected to double (Figure 1a; orange dotted line). Fortunately, more efficient air conditioners and policies encouraging the use and development of such units have the potential to cut the electricity consumption and global CO_2 emissions related to space cooling in half (Figure 1a; light blue line). But total electricity consumption and CO_2 emissions are not the only problems related to space cooling. The rising demand for space cooling also significantly impacts peak electricity loads. In the United States, where air conditioners are ubiquitous, space cooling accounts for around 29% of the peak load demand (Figure 1b). To meet this peak demand, power system operators must build and maintain sufficient power generation, transmission, and distribution capacity, even if that peak load only happens for a few hours every year. Diesel generators, gas-fired turbines or storage are typically used for this peaking capacity, but they lead to significant increases in electricity costs due to their low usage. And while solar photovoltaics (PV) can help match that peak cooling load, the intermittency of solar PV

means that PV alone cannot meet the total space cooling energy unless it is coupled with additional electrical energy generation from other sources (gas, wind, nuclear, hydro) or with storage.

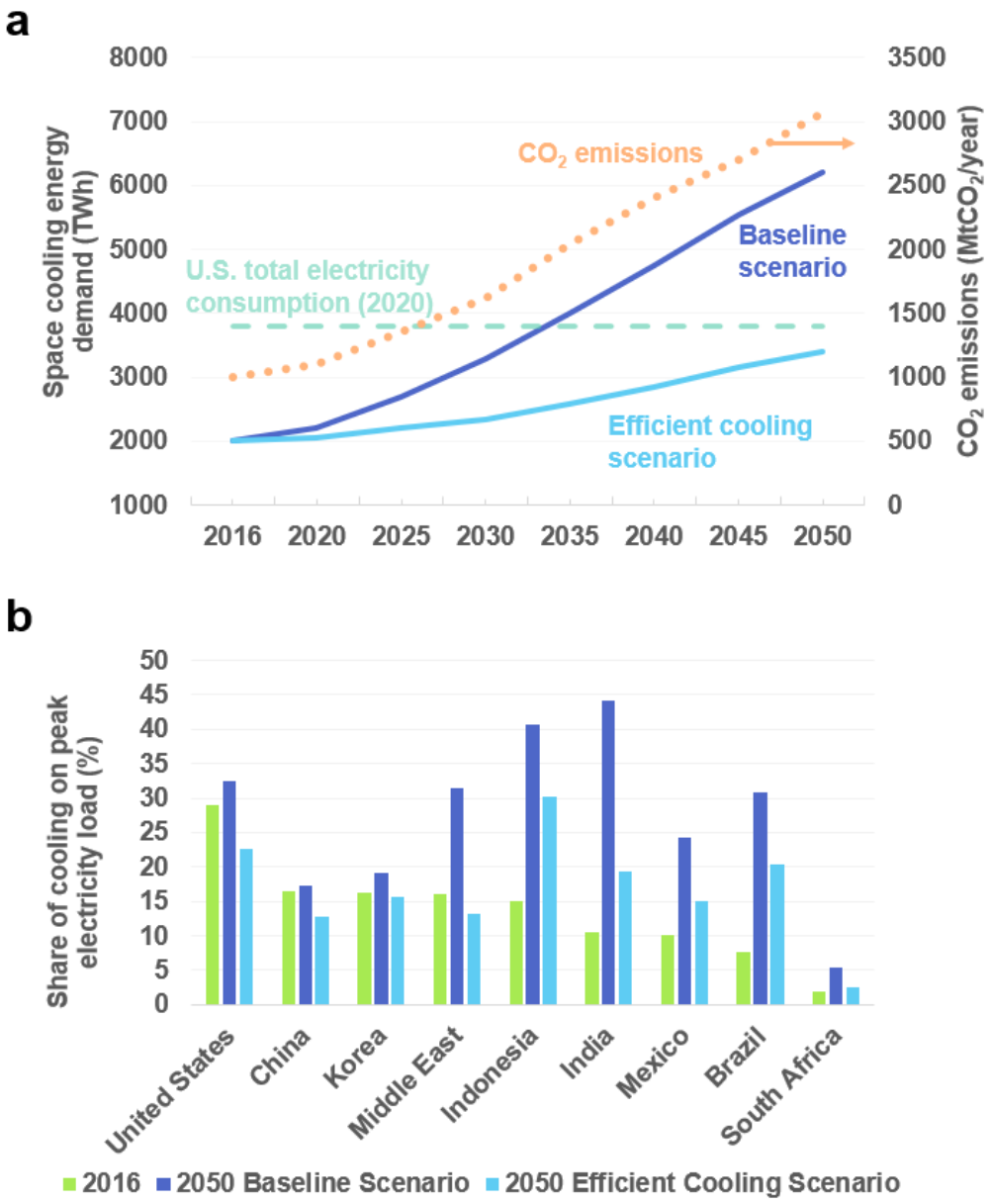

Figure 1 – ***Space cooling around the world****. (a) Current and predicted space cooling energy demand and related CO_2 emissions in the world* [1]*. The baseline scenario accounts for future predicted growth, as well as existing and announced policies and energy efficiency targets. The efficient cooling scenario assumes more efficient air-conditioning equipment and tighter regulations. For reference, the 2020 U.S. total electricity consumption (3082 TWh* [2]*) is shown in a dashed line. The space cooling CO_2 related emissions (dotted line) are also shown on the secondary vertical axis, currently accounting for 3% of global CO_2 emissions and trending upward. (b) The share of space cooling on peak electricity load in different regions. Based on IEA data from IEA (2018) The Future of Cooling, www.iea.org/statistics, All rights reserved; as modified by Arny Leroy.*

Aside from global standards and more stringent policies on buildings energy efficiency, more efficient air conditioners and refrigerators will be crucial in reducing future energy consumption, maximum peak electricity load and CO_2 related emissions.

1.1.2. Food Produce Storage

Meeting the world's growing food needs remains one of the greatest challenges of the twenty-first century. While 690 million people were undernourished in 2019, around one third of the food produced on earth was being wasted [3], [4]. This is particularly a problem in the developing world, where more than 15% of the post-harvest food is lost because of improper storage conditions [5], accentuating food insecurity, reducing farmer's income and depleting natural resources while causing unnecessary greenhouse gases emissions.

A major factor that controls the shelf-life of food produce is their storage temperature. For most fruit and vegetables, the deterioration rate increases by a factor of 2-3× for every 10 °C in temperature increase [6]–[9]. To reduce food spoilage, farmers typically harvest early in the morning, when the temperature is the lowest. But without access to refrigerated storage units, farmers in hot developing regions of the world are faced with significant post-harvest losses when the temperature rises during the daytime. Providing even a few degrees of cooling for food produce could go a long way into reducing post-harvest losses.

Cooling technologies such as gas-driven and solar refrigeration exist, but they rely on a steady supply of costly and polluting fuel or on expensive solar modules subject to theft and limited battery life. Alternative cooling technologies such as evaporative cooling and clay pot coolers are promising due to their low-cost and passive nature [10], but their efficacy is limited and they are limited to lower humidity climates. Developing new or improving existing low-cost passive cooling technologies for the storage of post-harvest food produce could significantly help reduce food losses in developing regions while improving economic development and food security.

One promising solution to help address existing and future global cooling challenges is to use passive cooling solutions such as passive radiative or evaporative cooling to provide electricity-free subambient cooling for food produce or to improve the efficiency of existing air conditioners and refrigerators. In the next sections, we will introduce and review the two passive cooling techniques and highlight the current challenges that these technologies face.

1.2. BACKGROUND ON EVAPORATIVE COOLING

In this section, we briefly introduce evaporative cooling and recent literature work on using hydrogels for thermal management of electronics, food and pharmaceutical products and buildings.

Evaporative cooling relies on the net vaporization of a liquid water phase into a vapor phase. When going through the liquid to vapor phase change, a large amount of energy (*i.e.*, the enthalpy of vaporization of water [$h_{fg} \approx 2440$ kJ/kg]) is removed from the liquid water layer, thus cooling it. The evaporation mass flux is driven by the difference in vapor density at the liquid surface ρ_0 and in the surrounding ambient air ρ_{amb}. Similar to a heat transfer process with conduction and convection, the evaporative flux needs to overcome two transport resistances – the first being the mass diffusion resistance governed by Fick's law in any diffusion-limited layer of thickness L with diffusion coefficient D and the second being the mass convection resistance (g_m) at the layer/air interface. Accounting for both resistances, we obtain the evaporative flux j_{evap} [11]:

$$j_{\text{evap}} = -\frac{(\rho_{amb}-\rho_0)}{\frac{L}{D}+\frac{1}{g_m}}. \quad (1)$$

An energy balance on the mass transfer process then requires that the evaporative cooling heat flux equals $q_{evap} = j_{evap} h_{fg}$.

One main advantage of evaporative cooling is that because it relies on the difference in vapor density, as opposed to temperature difference for air cooling, it allows cooling down to the wet-bulb temperature, which is always below or equal to the ambient dry-bulb temperature. In hot and dry climates, the wet-bulb temperature can be as low as 20 °C below the ambient dry-bulb temperature while in colder and more humid environment the wet-bulb temperature may be less than 5°C below the ambient dry-bulb.

While evaporative cooling is a ubiquitous process in nature and in mammals for temperature regulation, more recent works have tried to leverage it using hydrogels in novel applications such as buildings [12], [13], food and pharmaceutical supplies [11], [14], [15], and electronics thermal management [16]–[20]. Among the most common types of hydrogels, we find polyacrylamide [11], [12], [16], [20], polyvinyl alcohol [17], sodium polyacrylate [19] and thermoresponsive poly(N-isopropylacrylamide) (PNIPAM) [13], [14] hydrogels. The advantages of using hydrogels in passive cooling applications are numerous. Hydrogels can hold a large amount of water per mass of polymer and can provide a solid yet flexible support for water. Hydrogels can thus be fabricated and bent in any desired shape, whether it is a simple sheet that can easily be handled and installed on an object to cool, or in more complicated shapes to wrap around food or pharmaceutical products. Hydrogels can also be impregnated with salts such as $CaCl_2$ [16] or LiBr [20] to allow self-recharging by absorption during lower temperature operation or to decrease the

water effective vapor pressure to control the evaporation rate at a target operating temperature. Aside from hydrogels, recent work by the MIT D-Lab has also been exploring the use of clay pot coolers in sub-Saharan Africa [15], [21]. The clay pot coolers consist in a pot-in-pot design where one smaller clay pot is inserted into a slightly larger clay pot and where the remaining gap is filled with sand and water. After diffusing through the sand and the clay pot walls, water evaporates on the outside wall to the ambient, cooling the whole storage unit and the food produce stored inside. Their results, using only locally available materials, showed that they could provide an average subambient cooling around 8 °C below the ambient, extending the lifetime of specific vegetables by 2-4×.

Recent work has shown impressive passive evaporative cooling performance, but technical challenges still remain in specific applications. First, past work using hydrogel for passive cooling of buildings have severely suffered from solar absorption. In fact, using the hydrogel on small-scale buildings enabled a temperature reduction of 10 °C -25 °C under solar irradiance compared to an uncovered reference rooftop, but the hydrogel was still significantly above the ambient temperature. For large clay pot coolers, a solar cover must also be built specifically to minimize solar heating of the cooler, increasing costs and system size. Second, high water consumption leading to fast (few hours to few days) depletion of water in the hydrogel layer or clay pot cooler remains another challenge that limits how long cooling can be sustained. Current progress to address this challenge includes using a vapor permeable aerogel insulation layer to minimize parasitic heat gain while decreasing water consumption [11], or to use salts inside the hydrogel for self-recharging [16], [20]. The former solution however decreases the cooling performance due to added mass transport resistance while the latter decreases the water vapor pressure (lower cooling heat flux at a given temperature) while also causing a heating effect during the absorption process. Lastly, evaporative coolers cannot cool below the wet-bulb temperature, which limits their use in food and pharmaceutical products storage to lower humidity regions. New vapor permeable and insulating covers with a lower ratio of thermal conductivity to water vapor diffusion coefficient than that of air could help tackle this limitation [11].

1.3. BACKGROUND ON RADIATIVE COOLING

In this section, we first introduce the reader to radiative cooling, then review recent literature work, and finally end with technical challenges in radiative cooling systems.

Passive radiative cooling relies on the rejection of infrared radiation of terrestrial objects to the cold (4 K) outer space through earth's transparent atmospheric spectral window (8-13 μm). More commonly, radiative cooling by the earth's surface, clouds and atmosphere regulates earth's temperature by balancing absorption of solar radiation (Figure 2). But while naturally occurring radiative cooling can significantly

cool down the ambient temperature during the night (*e.g.*, a cold summer night in the desert), solar absorption during the day means that objects and the atmosphere tend to heat up rather than cool down during the day.

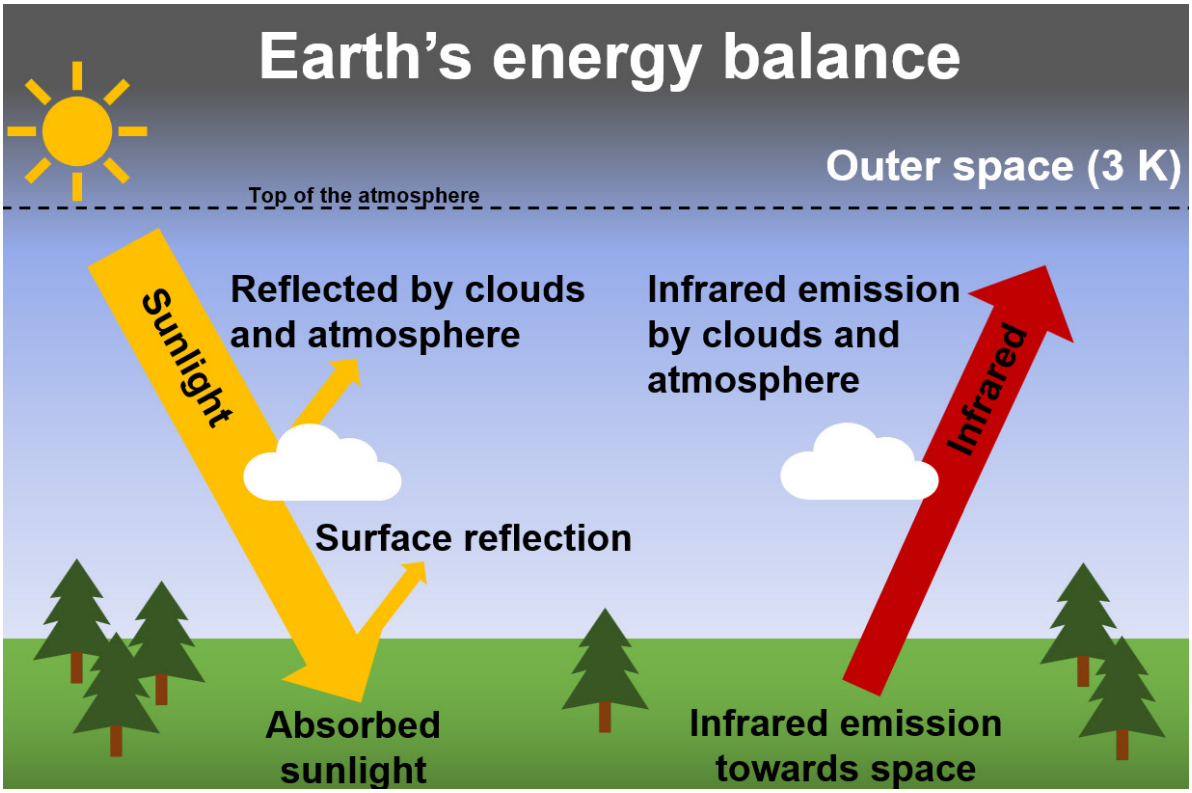

Figure 2 – ***Earth's energy balance****. Earth is constantly exposed to the sun's irradiance. Some of that light gets absorbed by the ground and terrestrial objects causing a net heating effect, while the rest gets reflected by clouds, the atmosphere, and the surface. This heating effect is compensated by a cooling effect (radiative cooling). The ground, terrestrial objects, clouds, and the atmosphere naturally emit infrared heat towards the cold outer space, provide a net cooling effect. The fine balance between solar heating and radiative cooling on earth ensures a stable temperature, year over year.*

We can estimate the net heat flow or cooling power P_{cool} of a surface facing the sky (referred to as an emitter or selective emitter) by performing an energy balance on it. The infrared heat rejected by the emitter P_{rad} is balanced by the downward atmospheric infrared radiation P_{atm}, parasitic heat gain from the ambient air $P_{\text{parasitic}}$ and solar absorption P_{sun}.

$$P_{cool}(T) = P_{rad}(T) - P_{atm}(T) - P_{parasitic}(T) - P_{sun}, \tag{2}$$

where

$$P_{rad}(T) = A \int d\Omega cos\theta \int_0^{\infty} I_{BB}(T,\lambda)\epsilon_{emitter}(\lambda,\theta)d\lambda, \tag{3}$$

$$P_{atm}(T_{amb}) = A \int d\Omega cos\theta \int_0^\infty I_{atm}(T_{amb}, \lambda)\epsilon(\lambda, \theta)\epsilon_{atm}(\lambda, \theta)d\lambda, \quad (4)$$

$$P_{parasitic}(T) = Ah_{eff}(T_{amb} - T), \quad (5)$$

and

$$P_{sun} = A\int_0^\infty E_{sun}(\lambda)\epsilon(\lambda, \theta_{sun})d\lambda. \quad (6)$$

In Eqs. (2)-(6), T is the emitter temperature, A is the emitter surface area, Ω is the solid angle, θ is the angle with the normal of the surface, λ is the wavelength of radiation, ε is the emissivity, I_{atm} is the temperature dependent spectral radiance of the atmosphere, E_{sun} is the spectral solar irradiance and the subscripts *atm*, *emitter*, *amb* and *sun* refer to the atmosphere, the emitter, the ambient and the sun respectively. When referring to the optical properties of the emitter in the solar spectrum, we will often use interchangeably $\rho_{solar} = 1 - \varepsilon_{emitter}$. The atmosphere's angular emissivity is estimated by $\varepsilon_{atm}(\lambda, \theta) = 1-\tau_{atm}^{1/\cos\theta}$ where τ_{atm} is the zenith angle atmospheric transmittance [22].

By optimizing the optical properties of an emitter facing the sky, one can theoretically radiatively cool it down to more than ~50 °C below the ambient or achieve cooling power $P_{cool} \approx 120$ W/m² at ambient temperature. However, experimentally achieving such subambient cooling or cooling power under direct sunlight (global horizontal irradiance [GHI] ~1000 W/m²) has proven challenging due to high solar absorption and parasitic heat gain from the ambient air.

Work on passive radiative cooling started more 50 years ago by Félix Trombe [23]. Since then, researchers have leveraged advances in photonics and materials science to develop optically selective materials that can achieve very high solar reflectance (ρ_{solar} = 94-99%) as well as high mid-infrared emissivity (ε_{IR} = 60-98%) that has enabled cooling up to 10.6 °C below ambient under direct sunlight [24]. These performance enhancements were achieved primarily through the proposed use of 1-D [25]–[27], 2-D [28], [29] and 3-D [30] photonic structures, metamaterials [24], [31]–[33], hierarchically porous polymeric materials [34], [35], pigmented paints [36]–[38] and even gases such as C_2H_4 [39] and NH_3 [40]. While new selective emitters are being proposed almost every day in the literature, the combination of optical properties, cost and scalability have mostly reached a plateau over the last several years, with several selective emitters showing all-day passive cooling and scalable fabrication process for commercialization.

In addition, several approaches to reduce parasitic heat transfer $P_{parasitic}$ between the cold emitter and its warmer surrounding environment while still allowing for infrared heat rejection by the emitter have been proposed. These include infrared transparent convection covers such as thin polyethylene films [24], [25], [29], [36], [39], [41]–[43], solar reflecting thin [44], [45] and thick [46] porous polyethylene covers, thick

solar reflecting and thermally insulating BaF_2 or ZnS covers [47], corrugated structures [48] and meshes [49], as well as ZnSe [50], CdS [51], Ge [52] or Si [52] windows placed over the emitter. Plain and porous polyethylene films have generally been preferred in the literature as they are cheap, scalable, and easily accessible. Their lack of robustness however makes them less adequate for practical applications. As an alternative, a more robust spectrally selective convection shield combining a polyester fabric with porous polyethylene has recently been proposed [53]. Practicality aside, a vacuum chamber was also recently used to suppress almost all parasitic heat gain, achieving a record low h_{eff} = 0.2-0.3 W/m²K and subambient cooling up to 42 °C below the ambient temperature [26]. While these results were impressive and experimentally demonstrated the full potential of radiative cooling, the use of a vacuum chamber is not scalable and very expensive. Overall, we find that while research on selective emitters is becoming saturated, research on convection covers still has some way to go in terms of scalability, optical and thermal performance, and robustness.

Recent developments in the field of radiative cooling have enabled all-day subambient cooling, even under direct sunlight, which was not possible in the past. Yet, the best performing radiative coolers presented in the literature still have a long way to go to reach the full potential of passive radiative cooling. In Figure 3, we compare the theoretical limit of cooling power vs emitter temperature drop ΔT in standard weather conditions with experimental results from past literature work. We note that literature works typically only report the maximum temperature drop (at P_{cool} = 0 W/m²) and the ambient cooling power (P_{cool} at ΔT = 0 K). Despite the recent advances presented earlier with selective emitters and covers, solar absorption (2-5%) at the emitter during the day and high parasitic heat gain (typical h_{eff} = 3-10 W/m²K for non-vacuum systems) still limit the minimum achievable temperature to around ~10 °C below ambient in practical demonstrations.

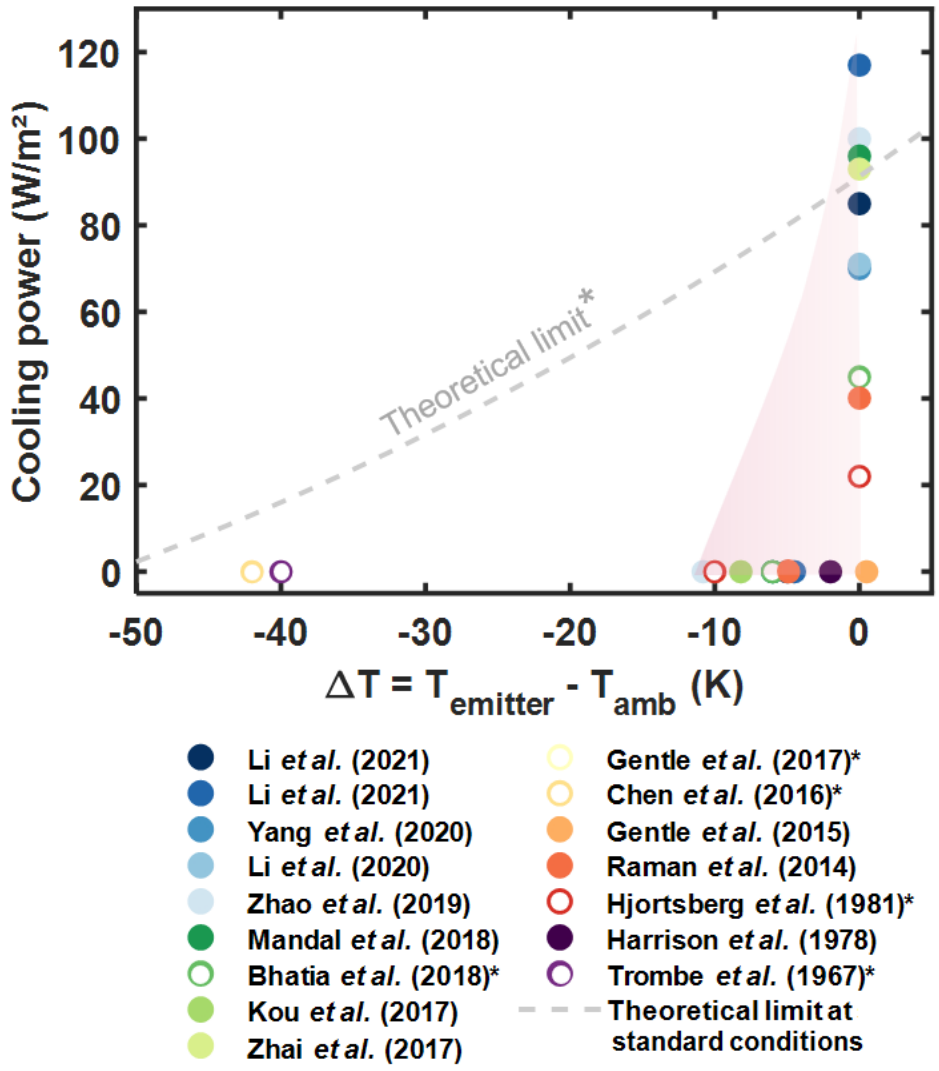

Figure 3 – ***Radiative cooling performance in the literature****. We note a large gap between the theoretical potential and experimental demonstrations, encouraging further innovations in radiative cooling. The open dots refer to experiments with indirect sunlight, while the solid dots were done under direct sunlight. The references for this figure are presented in the legend in this specified order:* [23], [25], [43], [46], [54]–[57], [26], [27], [34]–[37], [39], [41]. *Theoretical limit is valid only for: Ideal selective emitter (ε = 1 between 8-13 μm and ε = 0 elsewhere), U.S. Standard Atmosphere 1976, T_{amb} = 20°C, Precipitable Water Vapor (PWV) = 14 mm. Higher cooling power are possible for other emitters, higher T_{amb} and lower PWV.*

To explain the large difference between experimental demonstrations and the ideal radiative cooler, we quantitatively illustrate in Figure 4 the importance of solar absorption and parasitic heat gain for a perfectly insulated emitter and an ideal selective emitter, respectively. We observe (Figure 4a) that as little as 3% of solar absorption can reduce the cooling power by 30 W/m² and decrease the maximum subambient cooling from ΔT = -50 K to ΔT = -30 K. On the other hand, even a small h_{eff} = 2 W/m²K can reduce the maximum temperature drop from ΔT = -50 K to ΔT = -21.8 K (Figure 4b). When non-ideal

solar reflectance and parasitic heat gain both coexist such as is the case in real practical systems, we quickly realize that passive cooling of 10 K or more below the ambient temperature becomes very challenging. As we think about how we can bridge the gap between real and ideal radiative coolers, finding solutions that address both solar absorption and parasitic heat gain will be critical.

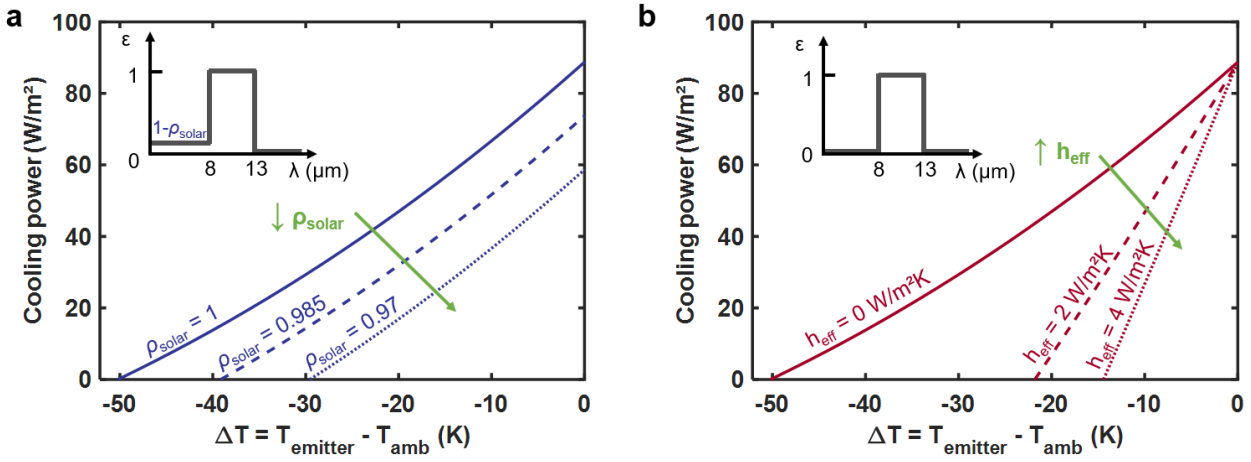

*Figure 4 – **Challenges in subambient radiative cooling**. (a) Influence of solar reflectance ρ_{solar} on the subambient cooling power of a perfectly insulated selective emitter under a GHI = 1000 W/m². (b) Influence of parasitic heat gain heat transfer coefficient h_{eff} on the subambient cooling power of an ideal selective emitter.*

1.4. THESIS OBJECTIVES AND OUTLINE

The objective of this thesis is to propose and optimize new passive cooling architectures that can achieve lower subambient temperatures and higher cooling power to enable new applications such as passive refrigeration of food produce and passive cooling of buildings. Details about the content of this thesis are outlined below:

In Chapter 1, we discussed the motivation for improving space cooling energy efficiency and the importance of refrigeration in post-harvest food losses. We also reviewed the current work on passive evaporative and radiative cooling, and identified important challenges associated with achieving low subambient temperatures and high cooling powers.

In Chapter 2, we present polyethylene aerogel as potential material candidate for passive cooling applications. We cover its fabrication, its optical, thermal and water vapor transport properties, its contact angle with water, as well as modeling for radiative transfer inside the material.

In Chapter 3, we propose to combine polyethylene aerogel with existing radiative cooling systems to minimize parasitic solar absorption and ambient heat gain, demonstrating improved subambient cooling performance over traditional radiative coolers.

In Chapter 4, we explore how ZnS nanoparticles in polyethylene aerogel covers can help increase the cover optical selectivity and evaluate its impact on the performance of daytime radiative coolers.

In Chapter 5, we propose a hybrid cooling architecture combining passive evaporative cooling with radiative cooling to achieve higher cooling power and lower stagnation temperature than previous standalone evaporative or radiative coolers.

In Chapter 6, we evaluate the potential impact of the hybrid cooling architecture on the storage of food produce and on the energy consumption of air conditioners and refrigerators in commercial buildings in the United States.

Chapter 2

2. Polyethylene Aerogels

Polyethylene aerogels (PEAs) were first publicly introduced around 2014-2015 by two independent research groups [58], [59]. More specifically, PEA is a low-density, high-porosity and open-cell porous material made of polyethylene and characterized by micrometer-sized pores (Figure 5a). The porous structure, composed of polyethylene lamellae, causes strong scattering of light in the solar spectrum (~0.25-2.5 μm wavelength range), giving rise to PEA's characteristic high solar reflectance and white appearance (Figure 5b; left). In the mid-infrared however, PEAs are semi-transparent due to low absorption by the polyethylene backbone and weak scattering by features much smaller than the radiation wavelength (Figure 5b; right). Furthermore, its low density (typically 10-50 kg/m^3) and microporous structure allow its conductive-convective thermal conductivity to be comparable to that of air (~0.03 W/(mK)) – making it an excellent thermal insulator. In previous works, it was suggested that possible applications of PEAs could include oil spillage recovery, filtration, controlled release of substances, electronics packaging, as well as thermal and sound insulation. In the next chapters of this thesis, we will however propose and demonstrate how PEAs' unique optical and thermal properties can be used to improve the performance of passive radiative and evaporative cooling systems. But before we jump into that, we will first dig deeper into the fabrication of PEA, its optical properties, how to model radiative transfer in PEA to predict its optical properties and estimate the radiative heat flux, and finally, characterize its thermal conductivity as well as the individual components composing it.

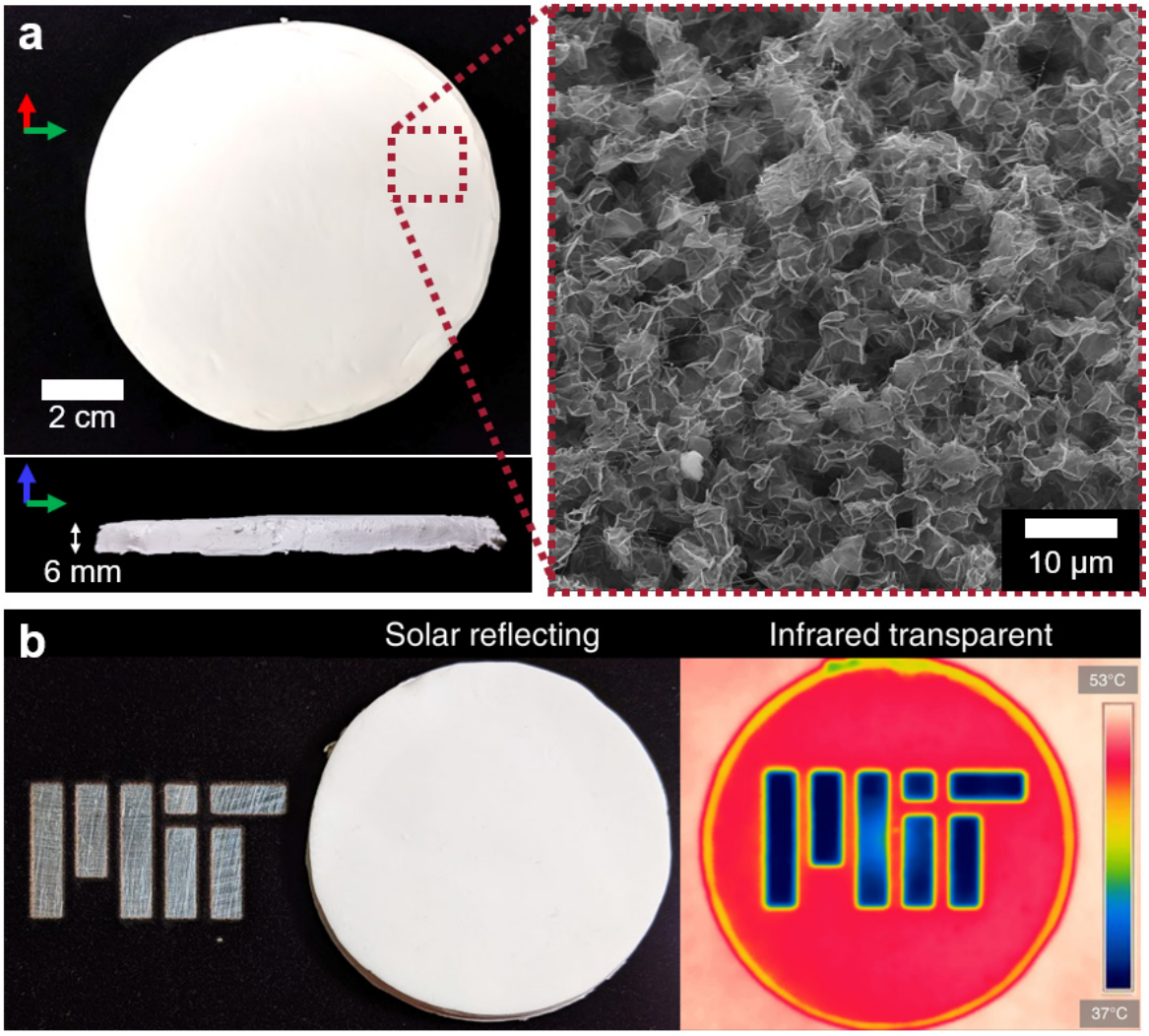

*Figure 5 – **Polyethylene aerogel.** (a) A picture of a 10-cm diameter and 6-mm thick PEA, as well as a scanning electron microscope image of its porous structure are shown. (b) Picture of a 4-cm diameter PEA sample in the visible spectrum (left; white opaque) and in the infrared (right; transparent).*

2.1. FABRICATION OF POLYETHYLENE AEROGELS

The fabrication process for polyethylene aerogels in this work follows the method proposed by earlier works [58], [59], which is based on the thermally induced phase separation (TIPS) of a polymer-solvent solution followed by supercritical CO_2 solvent extraction. A summary of the fabrication steps is presented in Figure 6. The process starts by mixing ultra-high molecular weight polyethylene (429015, Sigma-Aldrich; polymer) with paraffin oil (76235, Sigma-Aldrich; solvent) and butylated hydroxytoluene (W218405, Sigma-Aldrich; antioxidant) in a sealed beaker at room temperature. The solution is then heated in a silicone oil bath at 160 °C and mixed using a magnetic stirrer. After complete dissolution of the polymer in the solvent (~30 min), a homogeneous and transparent solution is formed and then poured

in an aluminum mold (13.5 cm diameter and 10 mm depth). The mold is then inserted in a water bath (5 °C), initiating the thermally induced phase separation and gelation of the polymer. Next, the paraffin oil is removed using an anti-solvent (miscible with the solvent, but not with the polymer) in a three-step solvent exchange with hexane. Another three-step solvent exchange in ethanol is then also performed to remove the hexane, a necessary step to ensure chemical compatibility with the last step of our process, the critical point drying. Finally, the gel is dried using a critical point dryer (Automegasamdri®-938, Tousimis) which replaces the ethanol from the gel with CO_2 while preventing collapse of the porous structure. In this work, the initial polymer concentration in the solvent was varied from 0.3 wt. % to 5 wt. % to maximize solar reflectivity and infrared transmittance while still achieving high sample fabrication yield and structural integrity of the gel and final aerogel. A 3:10 mass ratio of antioxidant to polymer was also used for all samples. The aerogel thickness was chosen as a compromise between number of samples needed for the experiments to achieve the desired thicknesses and fabrication time (*i.e.*, solvent exchange and critical point drying are diffusion limited processes). We note that while the mold was 10-mm thick, shrinking of the gel during the gelation, solvent exchange and critical point drying led to a final aerogel thickness around 30-50% thinner.

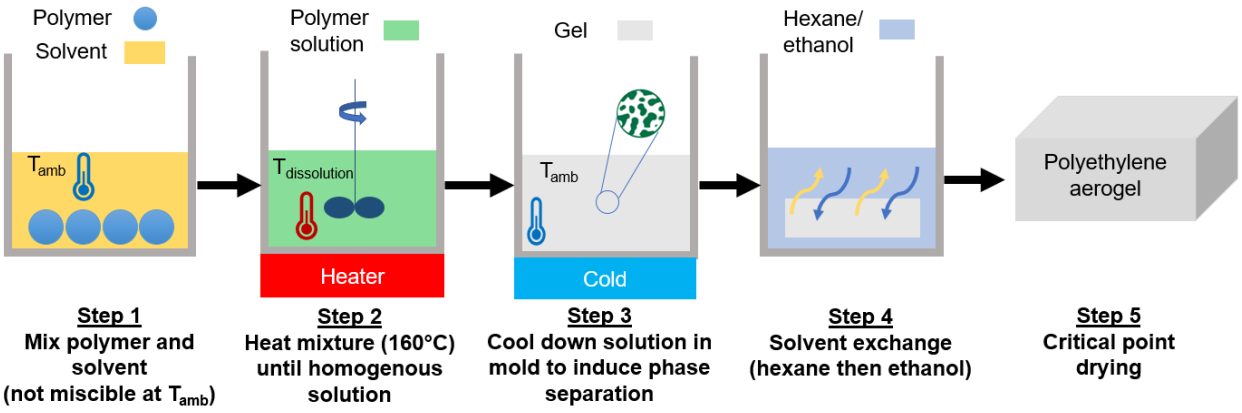

*Figure 6 – **Fabrication process of polyethylene aerogels**. Polyethylene powder is mixed in a solvent at high temperature to form a homogeneous solution. A gel is then formed by thermally induced phase separation (TIPS) of the polymer-solvent solution. After, the solvent is extracted by hexane and ethanol. Finally, we remove the ethanol from the gel using CO_2 supercritical drying.*

2.2. OPTICAL PROPERTIES OF POLYETHYLENE AEROGELS

Following the fabrication of the PEA samples, their optical transmittance and reflectance were measured using an ultraviolet–visible–near-infrared spectrophotometer (Cary 4000, Agilent) and Fourier Transform Infrared spectrometer (Nicolet 6700, Thermo Scientific). Integrating spheres (Internal DRA-2500, Agilent and Mid-IR IntegratIR™, Pike Technologies, respectively) were also used to measure the hemispherical

(direct + diffuse light) transmittance and reflectance of the samples. In Figure 7, we present the hemispherical (a) transmittance and (b) reflectance of five 5-mm thick PEA samples prepared with an initial polyethylene concentration of 0.3 wt. %, 0.5 wt. %, 1 wt. %, 2.5 wt. % and 5 wt. % with respect to the solvent. The density of the samples was measured to be 13 kg/m³, 18 kg/m³, 26 kg/m³, 52 kg/m³ and 80 kg/m³, respectively. We first observe that all samples show some optical selectivity, meaning that they achieve high solar reflectance and high infrared transmittance. While all samples with 0.5 wt. % or more of polyethylene achieve low solar transmittance (<10.3% vs 17.7% for the 0.3 wt. % sample), we however observe a more significant drop in infrared transmittance – 60% and 44% hemispherical transmittance between 8-13 μm for the 2.5 wt. % and 5 wt. % samples respectively, due to strong absorption and scattering. On the other hand, the 0.3 wt. % sample shows the highest infrared transmittance (92%) but was much more difficult to fabricate due to a weaker gel that was prone to breaking during solvent exchange and handling. As such, we used the recipe based on 0.5 wt. % of polyethylene in our experimental demonstrations presented later in this work, unless specified, as it provides good optical selectivity (10.3% solar transmittance and 88% infrared transmittance for a 5-mm thick sample) and can be fabricated reliably. We also note strong absorption peaks around 3.5, 6.8 and 13.8 μm, which are characteristic to polyethylene and are due to asymmetric stretching, bending and wagging of CH_2 molecules [60].

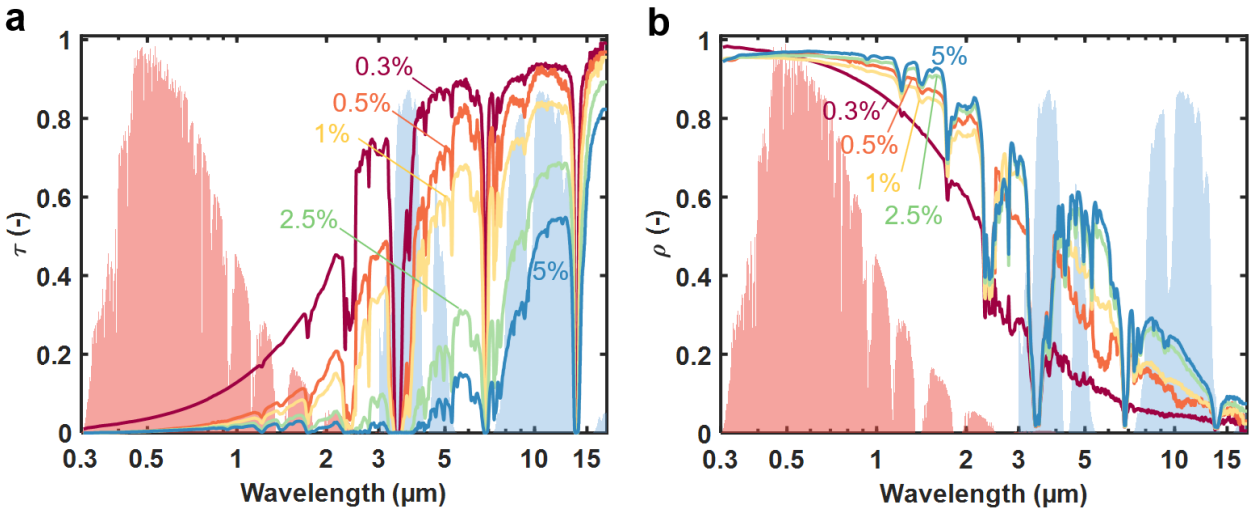

*Figure 7 – **Optical properties of polyethylene aerogels**. Hemispherical (a) transmittance and (b) reflectance of 5-mm thick polyethylene aerogel samples of various density.*

2.3. MODELING RADIATIVE TRANSPORT IN POLYETHYLENE AEROGELS

Modeling how light interacts with the PEA is an important step in predicting the material's performance in devices wherein the material interacts with light, radiation, or temperature gradients. The modeling of

radiative transfer in porous and aerogel materials has been realized at varying levels of complexity using different assumptions. Simpler models represent the porous structure as a series of parallel opaque planes [61] or assume an optically thick medium (Rosseland diffusion approximation [62], [63]), while more robust models account for absorption and emission of radiation by solving the radiative transfer equation (RTE) in scattering [64] or non-scattering media [65].

Due to the varying intensity of absorption and scattering of radiation across the solar and infrared spectrum in PEA (semi-transparent medium), detailed accounting of emission, absorption and scattering within the material, as is possible with the RTE, is necessary to appropriately model radiative transfer. The need for detailed modeling of radiative transfer is further accentuated by the wide range of optical depths – thin and low-density samples versus thick and high-density samples, and the different optical boundary conditions – low emissivity versus high emissivity, investigated throughout our work. We thus use the RTE to solve for the diffuse intensity of unpolarized light and consequently the radiative heat flux within a stationary medium of constant refractive index that experiences absorption, emission and scattering as a function of its temperature, optical properties (scattering albedo ω, extinction coefficient β and scattering phase function p), and boundary conditions. An excellent book by Stamnes et al. introduces the RTE and proposes methods to solve it while avoiding numerical errors [66]. The azimuthally symmetric 1-D spectral RTE with thermal emission is given by:

$$\mu \frac{dI_\lambda(\tau_\lambda, \mu)}{d\tau_\lambda} = I_\lambda(\tau_\lambda, \mu) - \frac{\omega_\lambda}{2}\int_{-1}^{1} d\mu' p_\lambda(\mu, \mu') I_\lambda(\tau_\lambda, \mu) - (1-\omega_\lambda) B_\lambda[T(\tau_\lambda)] - \frac{\omega_\lambda}{4\pi} F_\lambda^s p_\lambda(\mu, \mu'), \tag{7}$$

where λ is the wavelength of light, I_λ is the diffuse spectral radiance along direction $\mu = cos(\theta)$ at an optical depth $\tau_\lambda = \beta_\lambda x$ where x is the sample depth, θ is the polar angle (Figure 10) and B_λ is the spectral blackbody intensity at a temperature T and optical depth τ_λ, and F_λ^s is the spectral direct beam source (*i.e.*, unit beam source for calculating the transmittance or reflectance, or direct solar irradiation when calculating the radiative cooling power of an emitter). In this model, the PEA sample is subject to the following boundary conditions:

$$I_\lambda(0, -\mu) = \epsilon_{1,\lambda} B_\lambda(T_1) + 2\int_0^1 d\mu'\, \mu' (1-\epsilon_{1,\lambda}) I_\lambda(0, \mu), \tag{8}$$

$$I_\lambda(\tau_{\lambda,tot}, \mu) = \epsilon_{2,\lambda} B_\lambda(T_2) + 2\int_0^1 d\mu'\, \mu' (1-\epsilon_{2,\lambda}) I_\lambda(\tau_{\lambda,tot}, -\mu) + \frac{F_\lambda^s}{\pi} e^{-\tau_{\lambda,tot}(1-\epsilon_{2,\lambda})}, \tag{9}$$

where ε_i is the boundary emissivity, T_i is the boundary temperature and i represents the boundary index as per Figure 8. The first term of the right-hand side of the boundary equations represents the diffusion emission from that boundary. The second term refers to the diffuse reflection of diffuse light at that boundary while the third term accounts for the diffuse reflection of the beam source. Based on the system to model, we note that some of these terms might be dropped or changed. For example, we will later model radiative transfer within the aerogel when exposed to the ambient atmosphere. In that particular case, the boundary diffusion emission will be replaced by the angular-dependent sky radiance as modeled by MODTRAN®6.0 [67] using standard or experimental weather conditions (location, time, temperature and humidity). More details on the atmospheric modeling are provided in Section 2.3.1.

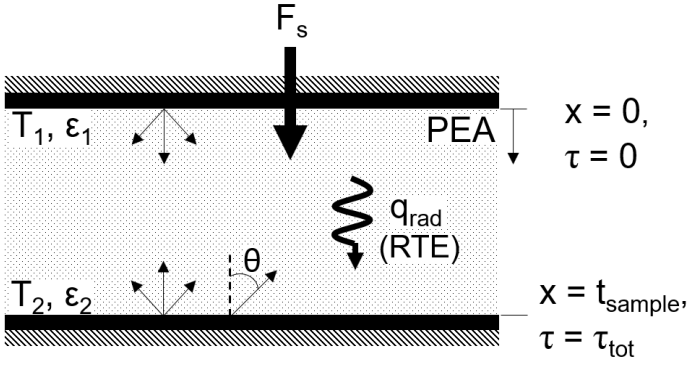

Figure 8 – ***Boundary conditions and coordinates system for solving the radiative transfer equation****.*

We solve the RTE in MATLAB using the discrete ordinate method [66] which transforms the RTE into a linear set of differential equations by discretizing the angular domain in $2N$ streams. We divide the medium into L layers to account for the spatially varying temperature and consequently blackbody intensity (B_λ) within the PEA. To calculate the diffuse transmittance and reflectance, we assume a unit beam source and integrate the diffuse intensity of light over the full hemisphere at both ends of the medium (in a direction normal to the medium). The hemispherical transmittance is then calculated by summing up the diffuse and direct (unattenuated) components. Finally, the radiative heat flux is calculated by integrating the spectral diffuse intensity over all wavelengths and angles:

$$q_r(x) = 2\pi \int_0^\infty \int_1^{-1} I_\lambda(\tau_\lambda(x), \mu)\mu d\mu d\lambda + \int_0^\infty F_\lambda^S \, e^{-\tau_\lambda} d\lambda \tag{10}$$

The spectral optical properties (scattering albedo ω, extinction coefficient β and scattering phase function p) of PEA were determined experimentally based on a previously validated method [68]. The method assumes that a unique set of optical properties exists (ω, β and p) for a given set of transmittances

(hemispherical and direct) and reflectance (hemispherical) of a sample of known thickness. By measuring the transmittance (hemispherical and direct), reflectance (hemispherical) and thickness of a PEA sample, it is therefore possible to evaluate the set of three primary optical properties which in turn can be used to model the transmittance and reflectance of similar samples with different thicknesses. For this method to work, we expressed the scattering phase function p as a function of a single parameter g, known as the Henyey-Greenstein scattering phase function [66],

$$p_{HG}(cos\Theta) = \frac{1-g^2}{(1+g^2-2gcos\Theta)^{\frac{3}{2}}}, \tag{11}$$

where Θ is the scattering angle. In Figure 9, we show the measured transmittances and reflectance (Figure 9a) as well as the thickness dependent hemispherical transmittance and reflectance of PEA in the solar and mid-infrared (8-13 μm) spectrum calculated using the PEA optical properties (Figure 9b).

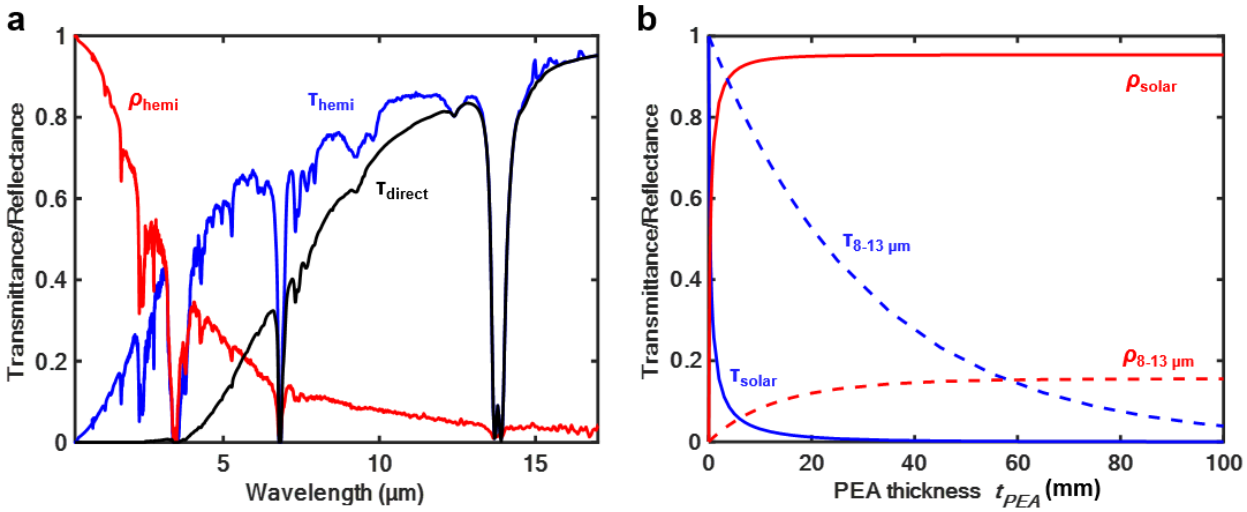

*Figure 9 – **Modeling polyethylene optical properties at various thicknesses.** (a) The measured optical hemispherical (blue) and direct (black) transmittance (τ) and hemispherical reflectance (ρ, red) of a 6-mm thick PEA sample. (b) Predicted solar (solid lines) transmittance/reflectance and infrared (8-13 μm, dashed lines) transmittance/reflectance as a function of PEA thickness.*

2.3.1. A Note on Atmospheric Transmittance Modeling

The atmospheric transmittance and irradiance for our modeling work was done using MODTRAN®6.0 [67]. Four approaches were used in this work, depending on the system to be modeled (*e.g.*, comparing with experimental results, modeling for a select city or modeling for standard conditions) and on the availability of the atmospheric weather data for modeling the atmospheric optical properties.

2.3.1.1. Standard Conditions

The *U.S. Standard Atmosphere 1976* atmospheric model available in MODTRAN®6.0 represents a standard model of atmosphere based on time-averaged altitude dependent temperature, pressure, density, viscosity and gas constituents. As a standard model, it serves as a good representation of the atmosphere although it might not offer an accurate representation of the atmospheric transmittance in specific locations.

2.3.1.2. Modified Standard Conditions

To account for the effect of temperature (T_{amb}) and precipitable water vapor on the atmospheric transmittance, we use a modified version of the *U.S. Standard Atmosphere 1976*. More specifically, we apply the altitude dependent temperature ($T_{\text{U.S. standard}}$) and atmospheric pressure ($P_{\text{U.S. standard}}$) profiles from the *U.S. Standard Atmosphere 1976* but we change the relative humidity profile $RH_{\text{U.S. standard}}$ in a different way based on the input precipitable water vapor. Our modified $RH_{\text{U.S. standard}}$ value is calculated using a correlation between total precipitable water vapor in the atmosphere and the ground level dew point [69]:

$$PWV = 10exp\left(0.1133 - ln(2.89 + 1) + 0.0393\left(\frac{9}{5}T_{dew\ point} + 32\right)\right), \qquad (12)$$

where PWV is the precipitable water vapor in mm, $T_{\text{dew point}}$ is the dew point temperature in °C, and the factor 2.89 corresponds to an average factor for the United States. $RH_{\text{U.S. standard}}$ is calculated from the dew point temperature. We note that $RH_{\text{U.S. standard}}$ may differ from the ground level relative humidity. This approach enables to capture the total amount of water vapor in the atmosphere, rather than considering only the relative humidity at the ground level, which is not representative of the water vapor content at higher altitudes. This approximation was used for the building level simulations in Chapter 6, using the hourly local precipitable water vapor as the input.

2.3.1.3. City Based Modeling Based on Radiosonde Weather Data

Radiosonde weather data consists of altitude dependent temperature, pressure and RH values for a given geographical location and time. Several organizations, such as the University of Wyoming, maintain post-processed databases of radiosonde weather data for a few cities around the world. When available, radiosonde weather data can thus be used to accurately model the atmospheric transmittance in MODTRAN®6.0with real altitude and time-dependent weather data. These atmospheric models are more accurate than other approaches but are not always available for the locations to model.

2.3.1.4. City Based Modeling Based on Long-Term Time-Average Global Data

When the radiosonde weather data is not available for a given city as is the case for Cambridge, MA where our experiments were performed, another approach can be used. The National Oceanic and

Atmospheric Administration (NOAA) maintains a publicly available long-term time-averaged altitude-dependent weather database that covers the surface of the Earth in a 2.5 degrees longitude by 2.5 degrees latitude grid. Weather data averaged over the past decades can then be used in MODTRAN®6.0with the built-in atmospheric generator toolbox (AGT) to estimate a representative atmospheric transmittance at given geographical coordinates and at a given time.

2.4. THERMAL CONDUCTIVITY OF POLYETHYLENE AEROGELS

The thermal conductivity of PEA can play an important role in applications requiring high thermal resistance such as radiative cooling. Yet, aside from broad values of thermal conductivity, thermal transport in PEA has not been studied much but could provide pathways for decreasing its thermal conductivity without compromising its optical properties.

In this section, we characterize thermal transport in PEAs, elucidating contributions of different heat transfer mechanisms and identifying pathways to further improve their thermal insulation performance. We first develop a theoretical framework that couples solid, gaseous, and radiative thermal transport. We then compare our modeling results with experimental characterization of thermal conductivity measured using a custom-built guarded-hot-plate thermal conductivity setup. Experimental measurements were performed using PEA samples with densities ranging from 12.0-82.2 kg/m^3 in three different gas environments (argon, nitrogen, and carbon dioxide) at a range of pressures below atmospheric pressure. Our results demonstrate that the thermal transport within the PEA is dominated by gas conduction as well as radiation when surrounded by high emissivity boundaries. In addition, we show that reducing the PEA pore size, adding opacifiers or controlling the gas environment (by evacuating samples or replacing air with low-thermal conductivity gases such as argon and carbon dioxide) could significantly improve the thermal resistance of PEAs. We believe the insights into thermal transport within a highly porous infrared-transparent medium from this work could help improve the performance of sub-ambient radiative cooling and lead to the development of better thermal insulation materials in general.

2.4.1. Thermal Modeling

Thermal transport in PEA can be decomposed into three components: solid conduction along the polyethylene backbone, gaseous conduction within the pores and radiative transfer through the PEA. Convection within the PEA pores (1-10 μm in size [46], [70]) is neglected due to the dominance of viscous forces over gravitational forces (small Rayleigh number) – consistent with previous work that demonstrated negligible convection in pores of diameter $\lesssim$1 mm [71], [72]. In this section, we present our

modeling framework that elucidates heat transfer through the PEA by coupled radiative transfer and conduction within the gas and solid phases (Figure 10).

2.4.1.1. Solid Conduction

Several different modeling approaches have been proposed in the literature to model solid conduction within aerogel and porous materials. While some approaches comprise of empirical models that correlate the material's density to solid conductivity [63], several others rely on equivalent circuit models [73]–[76] based on periodic arrays of intersecting spheres or rods with square or cylindrical cross-sections. In addition, past work has explored the influence of particle size in interconnected particle networks using finite element analysis and molecular dynamics simulations [77] as well as the influence of interfacial resistance between nanoparticles forming the backbone of the aerogel by exploring phonon scattering mechanisms [78]. A review of several of these approaches applied to aerogel and foam materials is presented by He *et al*. [79]. In this work, we use Glicksman's model [74], which accurately predicts the thermal conductivity of polymeric foams as shown in past studies [72], [80]–[82], to model heat transfer through the solid backbone of PEA. The model assumes that the material is made of gas-filled cubic cells formed by uniformly thick walls that are connected using struts. Heat flows only through the four wall faces and struts (parallel to the temperature gradient) of the cubic cell, and the local gas temperature is the same as the adjacent cell wall temperature. Based on this model, the solid conductivity can be expressed as:

$$k_s = k_{PE}(1-\phi)(\frac{2}{3}-\frac{f_s}{3}), \tag{13}$$

where k_{PE} is the thermal conductivity of the polyethylene backbone, ϕ is the porosity and f_s is the mass fraction of struts in the cubic cell. In this work, we use $k_{PE} = 0.53$ W/mK based on prior work that reported polyethylene crystallinity in PEA [59] and thermal conductivity of polyethylene with different crystallinities [83]. Furthermore, we use $f_s = 1$ based on literature results for low-density polymeric porous materials [81], [84]. The porosity is calculated from the PEA density (ρ_{PEA}), relative to polyethylene density (ρ_{PE}):

$$\phi = 1 - \rho_{PEA}/\rho_{PE} \tag{14}$$

2.4.1.2. Gaseous Conduction

The thermal conductivity of a dilute gas is commonly evaluated using the kinetic theory of gases. According to the kinetic theory, the thermal conductivity of a gas at a given temperature is independent of gas number density since the increase (decrease) in heat transfer due to more (less) gas molecules is cancelled by the corresponding decrease (increase) in the average collision distance (mean free path) between gas molecules. However, when constrained to a volume with a characteristic length smaller than

the mean free path, the gas molecules predominantly collide with the container walls – leading to gaseous thermal conductivity being proportional to the number of gas molecules or gas pressure. In porous materials such as PEA, gas conduction in the 1-10 μm pores can thus be strongly suppressed by decreasing the gas pressure. In this work, we used Kaganer's model [85] which accounts for this pressure-dependent gas conduction suppression in porous materials. Based on this model, the pressure dependent gaseous component of thermal conductivity k_g in a porous network with pores of diameter D can be estimated by:

$$k_g = \frac{\phi k_{g0}}{1+2\zeta Kn}, \tag{15}$$

where k_{g0} is the free space gas thermal conductivity, ζ is a coefficient that depends on the gas accommodation coefficient α and adiabatic coefficient γ, Kn is the Knudsen number defined as the ratio of the gas mean free path l_g and PEA pore diameter D. The gas mean free path is given by:

$$l_g = \frac{k_b T}{\sqrt{2}\pi d_g^2 P}, \tag{16}$$

where k_b is the Boltzmann constant, T is the gas temperature, d_g is the gas molecule diameter and P is the gas pressure. In this work, three gases are investigated: nitrogen, argon and carbon dioxide. The properties used for these gases are presented in Table 1. Coupling between the solid and gaseous conductivities is neglected which, as shown later, is a reasonable assumption due to the high porosity of the samples and the low thermal conductivity of the gases relative to the polyethylene backbone [86], [87].

Table 3 – Properties of gases investigated in this work at T = 20 °C and P = 101.325 kPa. k_{g0} is the thermal conductivity of the gas, d_g is the gas molecule diameter, α is the accommodation coefficient, γ is the adiabatic coefficient of the gas, and ζ is the gas dependent factor [87], [88].

Gas	k_{g0} (W/(mK))	d_g (Å)	α (-)	γ (-)	ζ(-)
Nitrogen (N_2)	0.0255	3.2	1	1.40	1.55
Argon (Ar)	0.0175	3.6	1	1.67	1.84
Carbon dioxide (CO_2)	0.0162	4.6	1	1.29	1.42

2.4.1.3. Radiative Transfer

Radiative transfer was modeled according to Section 2.3 with diffusely emitting boundaries and no direct beam source.

2.4.1.4. Total Thermal Conductivity

As radiative and conductive heat transfer are independent processes with different temperature dependence, it is necessary to account for their interaction and solve for the combined radiative and

conductive (solid + gas) heat transfer in semi-transparent media such as PEAs. We couple radiative and conductive heat transfer across the PEA by solving the heat equation [89]:

$$\frac{d}{dx}\left(-\left(k_s + k_g\right)\frac{dT}{dx} + q_r\right) = 0 \tag{17}$$

The heat equation is solved iteratively by varying the temperature profile in the PEA, similar to past work [64], [70], until the divergence of the radiative and conductive (solid + gaseous) heat fluxes converge. The total thermal conductivity k_{tot} of the sample can then be calculated by:

$$k_{tot} = \frac{\left(-\left(k_s+k_g\right)\frac{dT(x=0)}{dx}+q_r(x=0)\right)}{T_1-T_2} t_{sample}, \tag{18}$$

and the radiative component of thermal conductivity k_r is given by:

$$k_r = k_{tot} - k_s - k_g \tag{19}$$

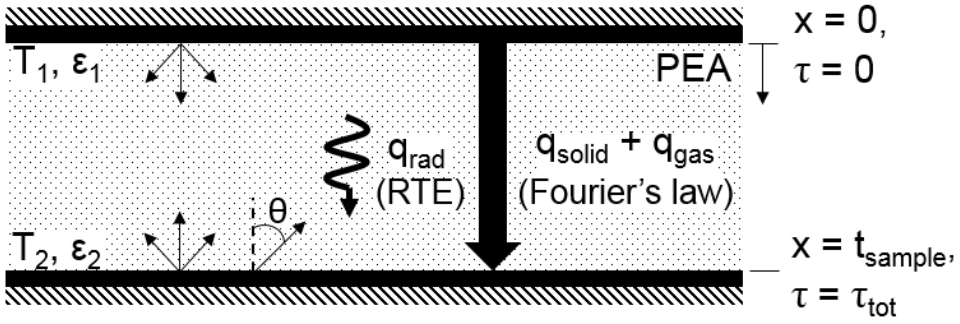

Figure 10 – ***Modeling framework for thermal transport in polyethylene aerogels****. Thermal transport in PEA comprising simultaneous radiative transfer (modeled using RTE: radiative transfer equation), and gas and solid conduction (modeled using Fourier's law).*

2.4.2. Material and Methods

We fabricated ~10-cm diameter PEA samples with densities ranging from 12.0 kg/m³ to 82.2 kg/m³. The samples were prepared according to the process presented in Section 2.1 by mixing 0.35 wt. %, 0.5 wt. %, 1 wt. %, 2.5 wt. % and 5 wt. % of polyethylene in paraffin oil to obtain samples of different densities. Details of the fabricated PEA samples are summarized in Table 2.

Table 4 – List of fabricated samples and corresponding boundary emissivity for experimental characterization.

Sample #	Density (kg/m³)	Thickness (mm)	Boundary emissivity (-)
1	12.0	5.3	0.94
2	15.6	5.7	0.94
3	24.3	8.9	0.94
4	52.6	7.5	0.94
5	81.0	8.3	0.94
6	14.8	4.1	0.03
7	18.2	5.8	0.03
8	26.7	8.1	0.03
9	54.2	7.3	0.03
10	82.2	8.1	0.03

The thermal conductivity of the fabricated PEA samples was measured using a custom-built guarded-hot-plate thermal conductivity setup (Figure 11) operated in the single-sided mode based on the ASTM C1044 – 16 standard [90]. The setup was equipped with a 65 mm diameter metering thin-film heater surrounded by a 140 mm diameter guard thin-film heater. The heaters were sandwiched between two 3.18-mm thick copper plates. A water-cooled aluminum cold plate was used for the cold-side boundary. The surfaces of the cold plate and heaters were painted with commercially available black paint or covered with aluminized mylar to provide high and low emissivity boundaries respectively (Figure 11C). The copper plates encasing the heaters and the cold plate included embedded thermocouples (type K) that were used to measure their temperature. The temperature difference between the hot and cold plates was measured using a three-junction-pair thermopile, and between the metering and guard heaters was measured using a single-junction-pair thermopile. All experiments were performed with a temperature difference of 20°C with T_1 = 12°C and T_2 = 32°C. The metering heater was connected to a power supply (2425, Keithley) in a four-wire configuration while the guard heaters were connected in a two-wire configuration to another power supply (2230-30-1, Keithley).

The guarded-hot-plate thermal conductivity setup was installed inside a 0.3 × 0.3 × 0.3 m environmental chamber to enable measurements at different pressures – from vacuum to ambient pressure, and in different gas environments – nitrogen (NI UHP300; Airgas), argon (AR UHP300; Airgas) and carbon dioxide (CD BD300S; Airgas). Gas pressure inside the chamber was measured using pressures sensors

(925 MicroPirani Transducer, MKS and PX319-030A5V, Omega). All data acquisition and control of the heaters was done using a custom LabVIEW program. The thermal conductivity uncertainty was calculated based on the uncertainty of the main heater area, the main heat power supply, the PEA sample thickness inside the setup, and the thermopile temperature difference. The PEA density uncertainty was determined from the uncertainty of the sample thickness, diameter, and mass.

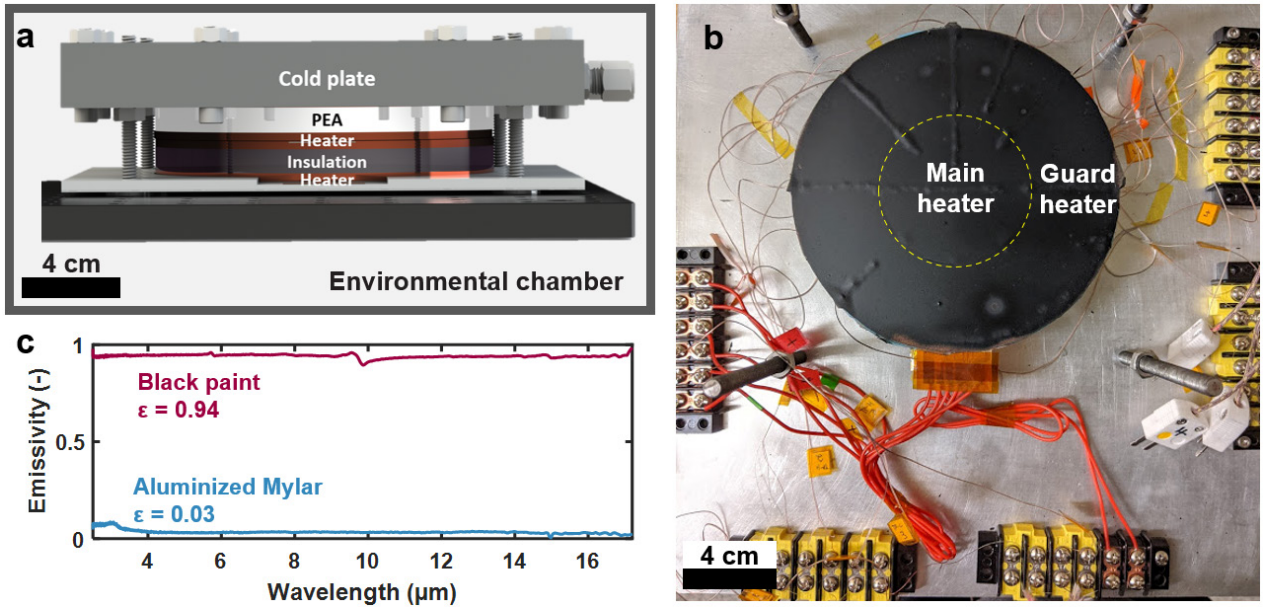

*Figure 11 – **Guard-hot-plate thermal conductivity setup**. (a) Rendering of guarded-hot-plate thermal conductivity setup. (b) Top view of the main and guard heaters painted with high emissivity black paint. (c) Spectral emissivity of the boundaries used in thermal conductivity measurements measured using Fourier-Transform Infrared spectroscopy.*

2.4.3. Results and Discussion

We experimentally characterize thermal transport in PEA using our custom-built guarded-hot-plate thermal conductivity setup. Experimental measurements were performed using the ten PEA samples presented in Table 2, in three different gas environments (argon, nitrogen, and carbon dioxide) at a range of pressures below atmospheric pressure and for two boundary emissivities (low and high emissivity). Finally, we estimate the contribution of the three components of thermal conductivity (solid, gas and radiative) in our PEA samples using a combination of our experimental and theoretical work.

2.4.3.1. Influence of Gas Type and Pressure

We measured the thermal conductivity of a low density (15.6 kg/m³) PEA sample (sample #2) with different gases and at a range of pressures using the guarded-hot-plate thermal conductivity setup with high emissivity boundaries. The corresponding experimental and theoretical results, depicted in Figure

12, show good agreement. The sample's effective pore diameter, evaluated by fitting the experimental gaseous thermal conductivity in nitrogen to the model [91], is estimated to be 5.6 µm – consistent with SEM observations and prior work [46]. At low gas pressures, measurements in all three gases converge towards the same value of 0.0253 W/(mK) representing heat flow via conduction through the solid polyethylene backbone and by radiative transfer. As gas pressure increases, we observe an expected increase in thermal conductivity as the mean free path of the gas molecules becomes smaller than the pore diameter. This increase in thermal conductivity with pressure is however different for different gases due to their distinct particle diameters d_g and coefficient ζ which, as per Eqs. 3 and 4, tend to shift the typical *S*-shaped thermal conductivity-versus-pressure curve towards higher pressures for smaller d_g or larger ζ, and vice versa. At ambient pressure, the sample's thermal conductivity strongly depends on the type of gas inside its porous structure; a reduction of around 0.010 W/mK (~20%) can be achieved by replacing nitrogen with lower thermal conductivity gases such as argon and carbon dioxide. While significant reduction in thermal conductivity is possible by decreasing the gas pressure, the results show that a pressure <10^3 Pa is required to suppress most of the gaseous conduction. Overall, these results show that significant reduction in thermal conductivity is possible by filling the PEA pores with a lower thermal conductivity gas, by reducing the gas pressure or by reducing the pore size.

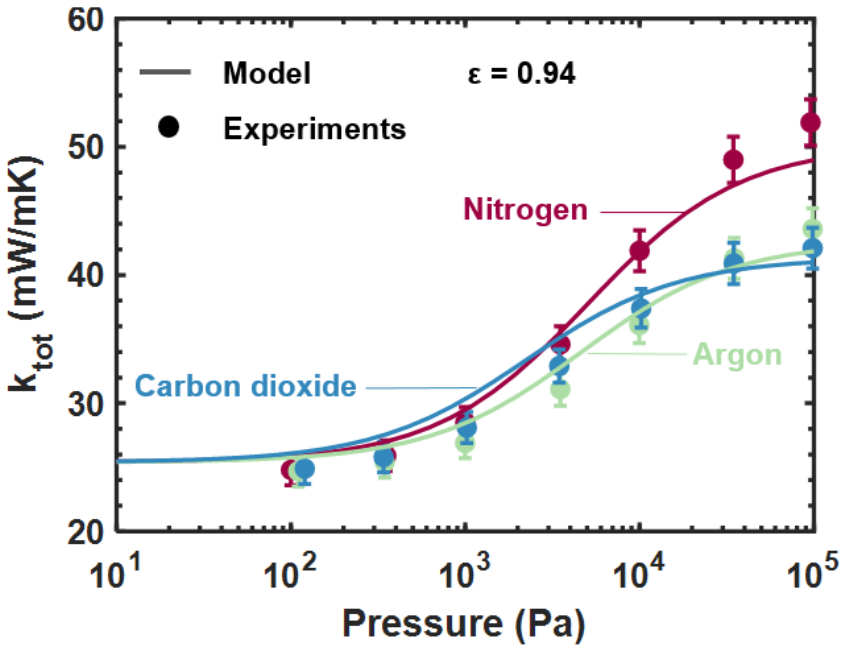

Figure 12 – ***Influence of gas type and pressure on thermal conductivity of polyethylene aerogels****. Measured and modeled thermal conductivity of a 15.6 kg/m³ density PEA sample filled with three different gases at pressures ranging from vacuum (10^{-3} Pa) to atmospheric pressure (10^5 Pa) with high emissivity (ε = 0.94) boundaries. The thermal conductivity at 10^{-3} Pa, not shown here, was measured equal to 0.0253 W/(mK).*

2.4.3.2. Influence of Boundary Conditions

Since PEAs are mostly transparent in the mid-infrared (Figure 7a), we expect their thermal conductivity to vary significantly with boundary emissivity which alters the radiative heat transfer contribution. In this work, we seek to distinguish the solid and gaseous components of thermal conductivity from the radiative component since several applications (such as atmospheric radiative cooling and indoor radiant cooling) require materials with low solid and gaseous conductivity but high infrared transmittance (*i.e.*, high radiative thermal conductivity). Figure 13 shows the experimental and theoretical thermal conductivity of low density (15.6 and 18.2 kg/m^3; sample # 2 and 7) PEA samples in nitrogen sandwiched between high (black paint; $\varepsilon = 0.94$) and low (aluminized Mylar; $\varepsilon = 0.03$) emissivity boundaries. In vacuum, the sample's thermal conductivity with low emissivity boundaries – characterized by conduction through the solid polyethylene backbone and negligible radiative transfer through the weakly absorbing/emitting material – approaches 0.0031 W/(mK). On the other hand, with high emissivity boundaries, we see a drastic increase in thermal conductivity in vacuum (0.0253 W/(mK)) stemming from the increased radiative transfer between the boundaries through the semi-transparent material. We however note that, as expected, the gas pressure dependence of thermal conductivity exhibits a similar behavior for both boundary emissivities. These results show that for applications requiring low solid and gaseous thermal conductivity alone, heat transfer through the material can be nearly completely suppressed by reducing the gas pressure to below 10^3 Pa. For other applications requiring low radiative conductivity as well (*i.e.*, typical thermal insulation), the results suggest that the addition of low emissivity boundaries or infrared opacifiers could reduce the total thermal conductivity significantly. Overall, the semi-transparent nature of PEA makes the material's thermal conductivity highly dependent on the boundary conditions which should be clearly specified and carefully considered for target applications (*e.g.*, PEA cover for radiative cooling with high emissivity boundary versus PEA for typical insulation with low emissivity boundary).

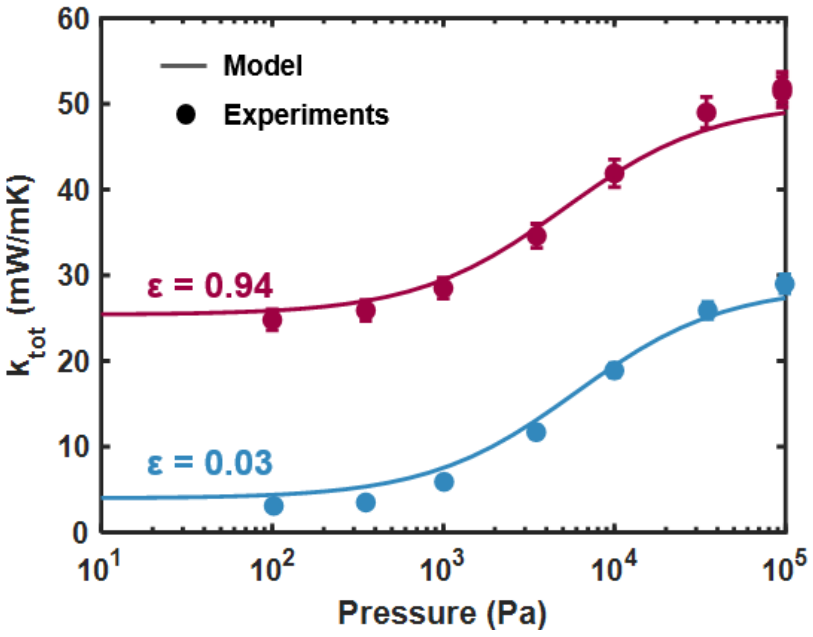

Figure 13 – ***Influence of boundary emissivity on the thermal conductivity of polyethylene aerogels in nitrogen.*** *Sample #2 (5.7 mm thick and density 15.6 kg/m³) was tested with high emissivity boundaries (ε = 0.94) and sample #7 (5.8 mm thick and density 18.2 kg/m³) was tested with low emissivity boundaries (ε = 0.03).*

2.4.3.3. Influence of PEA Density

Next, we investigate the influence of density on the total thermal conductivity of PEA in nitrogen with low (Figure 14a) and high (Figure 14b) emissivity boundaries. We notice that the inflection points of the *S*-curves in Figure 14a and Figure 14b shift slightly towards higher gas pressures for denser samples, suggesting smaller pore sizes. We also observe that, in general, higher density samples have higher thermal conductivity due in part to an increase in solid conduction through the polyethylene backbone. While the effect of density on thermal conductivity is clear for the low emissivity boundaries measurements (Figure 14a), a more complex behavior is observed for the measurements with high emissivity boundaries (Figure 14b). In the next section, we use our model to decouple different components of the experimentally determined thermal conductivities and show that gaseous conduction as well as radiative transfer between the high emissivity (ε = 0.94) boundaries dominate the total heat transfer in PEA.

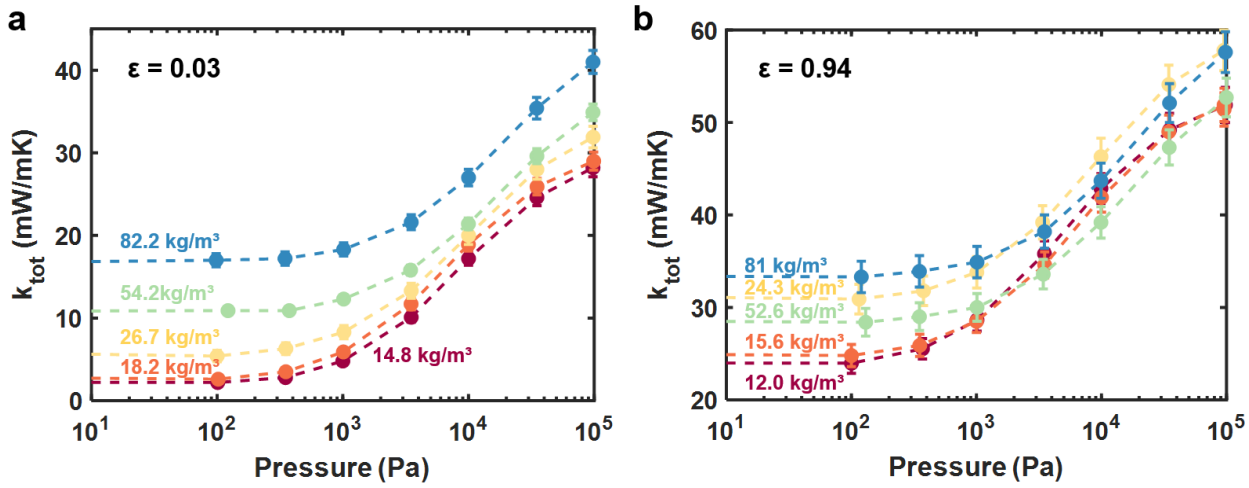

*Figure 14 – **Influence of density on the thermal conductivity of polyethylene aerogels.** Measured thermal conductivity of PEA samples with different densities in nitrogen as a function of gas pressure (10^2 to 10^5 Pa) for (a) low emissivity (ε = 0.03) and (b) high emissivity (ε = 0.94) boundaries. The thermal conductivity was also measured at 10^{-3} Pa but is not shown here for clarity and due to the negligible difference with results at 10^2 Pa. Dashed lines are guides to the eye.*

2.4.3.4. Decomposing Different Thermal Conductivity Contributions

Using our modeling framework, we delineate the three components of thermal conductivity from experimentally measured thermal conductivity and optical properties of PEA samples.

Figure 15a shows the pressure dependent gaseous component of thermal conductivity k_g for PEA samples measured with high emissivity boundaries. k_g is evaluated by subtracting the total thermal conductivity k_{tot} from the total vacuum thermal conductivity (k_{tot} at 10^{-3} Pa). We estimate the effective pore diameter by fitting the model to the data – as was done in Figure 12. As discussed in Section 2.4.3.3, higher density samples have smaller pore sizes resulting in lower gas thermal conductivity at a given pressure.

Next, we use our radiative transfer model to estimate the radiative component of thermal conductivity k_r for each sample based on their thickness and optical properties, and the experimental boundary conditions. Figure 15b shows the results plotted for the two boundary emissivities and for samples with different thicknesses. Higher k_r is observed for high emissivity boundaries than for low emissivity boundaries due to radiative transfer between boundaries through the semi-transparent PEA. Opposite trends are however observed with respect to PEA density for the low and high emissivity boundaries. For the high emissivity case, a decrease in k_r with increasing density is observed due to a reduction in PEA infrared transmittance, which inhibits radiative transfer between the two boundaries. For the low emissivity case, the boundaries are almost perfect reflectors and therefore do not contribute much to k_r. But as the PEA density increases, the sample absorption and emission increase in the infrared, therefore increasing the radiative transfer (k_r). We note that k_r also depends on the boundary temperatures and

sample thickness (as represented by the shaded areas in Figure 15b), and that k_r would fall to zero if we increased the optical depth of the sample to infinity.

Finally, we calculate the solid component of thermal conductivity k_s by subtracting k_r from the total thermal conductivity in vacuum (k_{tot} at 10^{-3} Pa). Figure 15c shows the modeled and experimental k_s values for different PEA densities. As expected, the solid conductivity increases with density and is relatively low ($\leq$ 0.005 W/(mK)) for densities smaller than 30 kg/m³.

Overall, decomposing the total thermal conductivity into its three components reveals that at ambient conditions, gaseous conduction and radiative transfer typically dominate heat transfer through PEA, while solid conduction contribution is generally negligible at low densities.

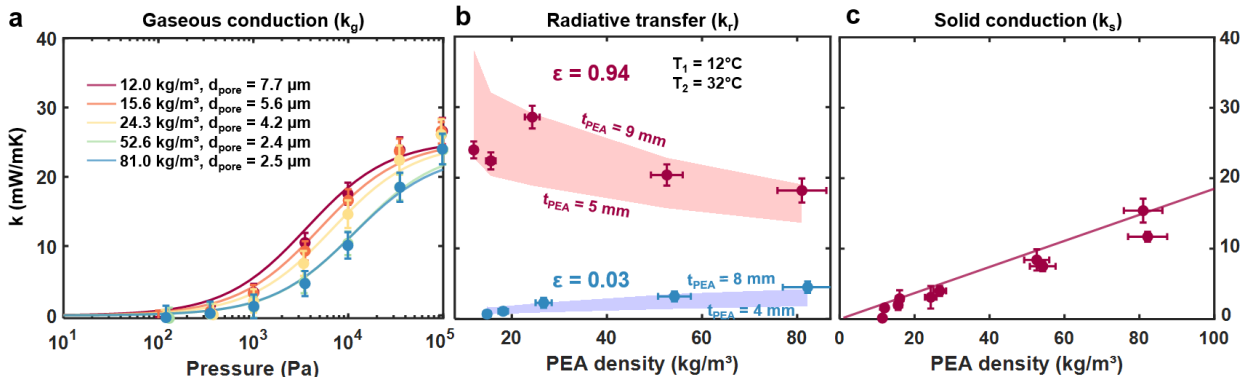

Figure 15 – ***Contribution of the three components of thermal conductivity.*** *(a) gaseous (in nitrogen; only high emissivity boundary measurements are shown for clarity), (b) radiative and (c) solid. The shaded areas in (b) represent the modeled range of k_r for different PEA thicknesses to account for the variable thickness of the experimentally tested samples.*

The experimental data and modeling results provide insights on ways to reducing PEA thermal conductivity and improving insulating properties. First, we note from Figure 15a that pores inside PEA are too large relative to the gas mean free path to provide any significant reduction in gas thermal conductivity at ambient pressure. Reducing PEA pore size could help reduce the most important contributor to the material's thermal conductivity by shifting the thermal conductivity-versus-pressure *S*-curve towards higher pressure, reducing PEA thermal conductivity at any given pressure – similar to past observations with other types of aerogels [63]. Second, replacing nitrogen (or air) with a lower thermal conductivity or smaller molecular diameter gas could also reduce the gaseous component of thermal conductivity – by up to 36% for carbon dioxide at ambient pressure. Third, reducing the gas pressure inside PEA by sealing it could completely eliminate gaseous conductivity. However, sealing the aerogel for long periods of time, ensuring the mechanical stability of PEA under one atmosphere of pressure, or using infrared transparent sealants (required for radiative cooling applications) will likely be challenging. Fourth, for applications other than atmospheric radiative cooling or indoor radiant cooling, the radiative

component of thermal conductivity k_r can be significantly reduced by using opacifiers. Finally, solid conduction can be minimized ($\leq$ 0.005 W/(mK)) by maintaining the PEA density below 30 kg/m^3.

2.5. OTHER PROPERTIES OF POLYETHYLENE AEROGELS

2.5.1. Contact Angle

Polyethylene aerogels were observed to be hydrophobic when pouring water on top of it. We validated this by performing a water contact angle measurement (Figure 16), measuring an advancing contact angle of 141° and receding contact angle of 105°. A high contact angle is promising for repelling rainwater and to clean the PEA surface from dirt during outdoor exposure.

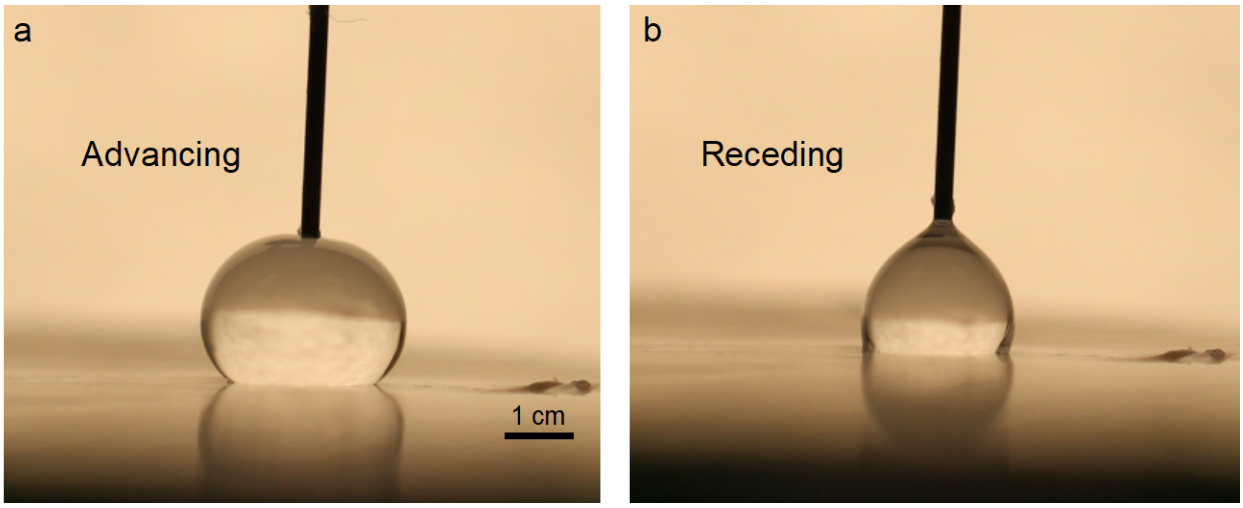

*Figure 16 – **Dynamic contact angles.** (a) Water advancing contact angle on PEA is 141±2°. (b) Water receding contact angle on PEA is 105±10°. Credit: Zhengmao Lu, Massachusetts Institute of Technology.*

2.5.2. Water Vapor Diffusion Coefficient

The diffusion coefficient of water vapor in PEA was determined as D_{PEA} = 0.18±0.02 cm^2/s at 24 °C using the wet cup method following ASTM E96 [92] (Credit: Zhengmao Lu, Massachusetts Institute of Technology). For reference, at standard temperature and pressure, the diffusion coefficient of water vapor in air is 0.28 cm^2/s.

2.6. SUMMARY

In this chapter, we first introduced polyethylene aerogels (PEAs) as a low-density and highly porous open-cell material with high solar reflectance, infrared transmittance, and low thermal conductivity. We

described the fabrication process of the material and then characterized the optical properties of PEA at various densities. We then presented a radiative transfer model that will be used throughout the rest of this thesis that allows to model the transmittance (hemispherical and direct), reflectance (hemispherical) and the radiative heat flux through the PEA based on a set of boundary conditions and a temperature profile within the material. Finally, we presented a detailed study of the thermal conductivity of PEAs in which we decomposed the total thermal conductivity into solid, gaseous, and radiative components. Our modeling framework, supported by experimental results, was then used to provide pathways to increasing the thermal resistance of PEAs, suggesting decreasing the pore size, using lower thermal conductivity gases, operating at lower gas pressures, adding infrared opacifiers, and using lower density sample as possible solutions. In the following sections, we will see how polyethylene aerogels and their unique set of thermal and optical properties can enable higher cooling performance in applications such as passive radiative and evaporative cooling.

Chapter 3

3. All-Day Passive Subambient Radiative Cooling Using Polyethylene Aerogels

3.1. INTRODUCTION

Most of the recent work in the field of radiative cooling has focused on either reducing solar absorption (*i.e.*, selective emitters) or reducing parasitic heat gain at the emitter. Yet, a solution that addresses both these challenges could enable simpler and higher performance subambient radiative cooling. In this chapter, we propose using optically selective and thermally insulating (OSTI) emitter covers to simultaneously tackle these two challenges, as presented in Figure 17 [47], [93]. By taking advantage of the cover's added thermal resistance between the emitter and the ambient (*i.e.*, reduced h_{eff}) as well as its selective reflectance and transmittance (*i.e.*, high solar reflectivity ρ_{solar} and infrared transmittance $\tau_{8\text{-}13\mu m}$), higher subambient cooling power and colder stagnation temperatures may be achieved. Inspired by this approach, we theoretically and experimentally demonstrate deep subambient radiative cooling using custom-fabricated polyethylene aerogel (PEA), a thermally insulating, solar reflecting and infrared transmitting material. Using experimentally determined optical properties of the fabricated PEA and a robust theoretical model that accounts for radiative and conductive transport within the PEA, we then show that the approach has the potential to achieve sub-ambient cooling of up to 7 °C under 1000 W/m² of direct sunlight and *U.S. Standard Atmosphere 1976* [67], beating a selective emitter alone by more than 4 °C. We also demonstrate that using PEA enables the use of simpler emitters due to the optical selectivity of the cover, while opening up a wide regime of subambient temperatures and cooling powers that were not previously achievable. Finally, using a proof-of-concept experimental setup and the fabricated PEA, we report a maximum ambient temperature daytime cooling power of 96 W/m² and a sub-ambient cooling as high as 13 °C around solar noon (1123 W/m² GHI), a more than 22% increase in emitter sub-cooling under direct sunlight over previously reported work [24] operating under similar experimental conditions (around solar noon under direct sunlight or without a solar shade casting a shade on the emitter and in air). These theoretical and experimental results demonstrate the potential of OSTI covers for simple and high-performance radiative cooling, that could improve the performance of existing radiative coolers as well as enable next-generation passive cooling systems.

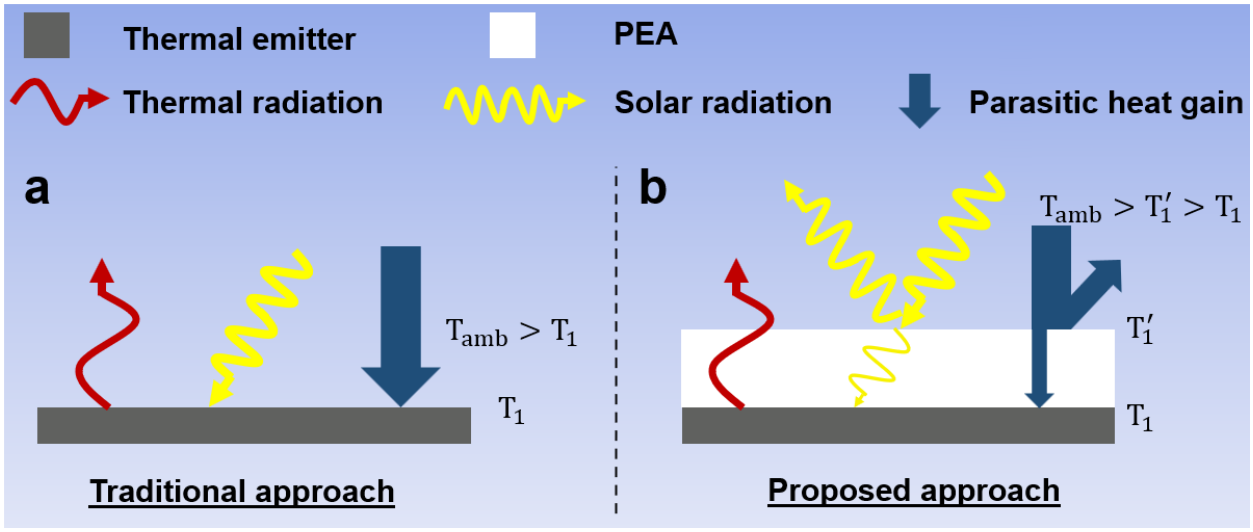

Figure 17 – ***Schematic of the proposed approach.*** *(a) Traditional approach to radiative cooling. An emitter facing the sky is exposed to solar irradiation and parasitic heat gain from the ambient air due to convection. (b) Proposed approach where an optically selective and thermally insulating (OSTI) cover is placed on top of the emitter. This insulation reduces parasitic heat gain as well as the solar irradiation reaching the emitter, enabling lower emitter temperatures and higher sub-ambient cooling power.*

3.2. POLYETHYLENE AEROGEL COVERS

In past work, thin (<100 μm) polyethylene [60] and nanoporous polyethylene [45] films have been widely used as convection covers due to their low cost and good infrared transmittance. However, their high density has precluded the use of thicker films that could provide additional thermal insulation to the emitter due to dominant infrared absorption. By combining the advantages of polyethylene with that of aerogels, a class of materials with high porosity, ultra-low thermal conductivity and density, PEA could thus offer the possibility of a highly insulating and infrared-transparent cover for radiative cooling. The PEA samples used in this chapter were prepared as per Section 2.1. On average the samples were measured to have a low density of 15 ± 2 kg/m³ and a low thermal conductivity (solid + gas components only) of 28 ± 5 mW/mK, nearly equal to that of air (k_{air} = 26 mW/mK) due to negligible solid heat transfer through the polymer. At a thickness of 6 mm, the PEA showed high transmittance ($\tau_{8\text{-}13\mu m}$ = 0.799) in the atmospheric transparency spectral window (8-13 μm), while still achieving high solar reflectance (ρ_{solar} = 0.922) due to strong scattering by its porous structure at shorter wavelengths (0.3-2.5 μm). Due to its characteristic porous structure and ultra-low density, PEA possesses exceptional optical and thermal properties ideal for high-performance sub-ambient radiative cooling, and even at large thicknesses (~ cm) which was not possible with previous materials such as nanoporous polyethylene.

3.3. MODELING THE COOLING POTENTIAL OF AN EMITTER COUPLED WITH PEA

To accurately evaluate the performance of an emitter coupled with PEA, both conductive and radiative thermal transport must be simultaneously considered. In fact, the thicker the PEA, the more it absorbs, emits and scatters light, which in turn affect the temperature profile within it and the corresponding conductive heat flux (*i.e.*, parasitic heat gain $P_{\text{parasitic}}$). The contribution of the conductive and radiative heat fluxes as well as their interactions therefore affect the total heat flux at the emitter (*i.e.*, emitter cooling power P_{cool}). To account for both effects, we numerically solved the steady-state 1-D heat transfer equation (HTE) within the PEA,

$$\frac{d}{dx}\left(-k_{PEA}\frac{dT}{dx}+q_r\right)=0, \tag{20}$$

where k_{PEA} is the PEA thermal conductivity (solid and gaseous components only), x is the spatial coordinate along the thickness of the PEA, T is the spatial PEA temperature profile and q_{r} is the spatial radiative heat flux. The simplified HTE (Eq. (20)) states that for energy to be conserved, the spatial rate of change of the conductive and radiative heat flux are of equal magnitude (but of different sign). Whereas the conductive term can easily be calculated from Fourier's law, the evaluation of the radiative term is more complex due to absorption, emission and multiple scattering, all occurring within the PEA and impacting the radiative flux at the emitter. We thus evaluated the radiative heat flux q_{r} within the PEA by numerically solving the radiative transfer equation (RTE) using the discrete ordinate method (*37*) as per Section 2.3. To solve Eq. (20), we start by splitting the PEA into L layers and then take an initial guess on the temperature profile T within the PEA. Each of the L layers is assumed to have a linear temperature profile within it. We then independently solve for the conductive and radiative terms at each of these layers and then update T to minimize the difference between the divergence of the radiative and conductive heat fluxes. Upon convergence of the temperature profile, the model allows calculation the PEA steady state temperature profile as well as conductive and radiative heat flux at all positions within the PEA. We summarize the modeling framework in Figure 18.

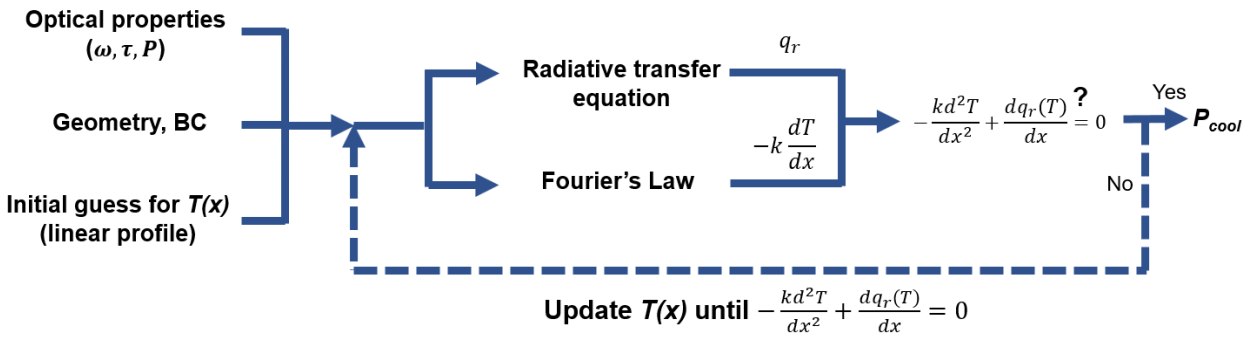

Figure 18 – ***Iterative process for cooling power modeling.*** *Iterative process for solving for the cooling power P_{cool} at the emitter for combined radiative and conductive heat transfer in the PEA.*

Finally, the emitter cooling power P_{cool} is calculated by summing the contribution of the conductive and radiative heat flux at the PEA/emitter boundary.

$$P_{cool} = q_r(x = t_{PEA}) + q_{cond}(x = t_{PEA}) \tag{21}$$

We note that the cooling power represented by Eq. (21) assumes no parasitic heat transfer to the bottom of the emitter, and as such only accounts for heat transfer of the emitter with the ambient air and atmosphere.

Convection with the ambient air, solar irradiation and atmospheric emission towards the emitter were implemented as boundary conditions at the top of the PEA while a diffusely emitting and reflecting emitter at $T_{emitter}$ were set as boundary conditions at the bottom of the PEA. When modeling our experimental systems, we estimated the convection heat transfer coefficient h_{conv} based on the wind speed at the time of our experiments using the empirical relation $h_{conv} = 5.7 + 3.8V$ as proposed by Ezekwe [94]. In the following sections, we use this model to predict the cooling performance of a radiative cooler with various PEA thickness and in different weather conditions.

3.4. COOLING PERFORMANCE ENHANCEMENT USING PEA

Using the developed model and experimentally determined optical properties of the PEA, we predict the cooling power of any given emitter (with known spectral optical properties and temperature), ambient conditions (that include ambient temperature, spectral atmospheric transmittance, solar irradiation and convection coefficient with ambient air) and PEA thickness. Figure 19 shows the theoretical daytime (Figure 19) and nighttime (Figure 19b) cooling power of a typical stepwise selective emitter ($\rho_{solar} = 1\text{-}\alpha_{solar} = 0.97$; $\varepsilon_{IR} = 0.9$) facing a standard atmosphere (*U.S. Standard Atmosphere 1976*) at different temperatures $\Delta T = T_{emitter} - T_{amb}$ combined with PEA of varying thickness t_{PEA}. Results show that

in the absence of PEA (t_{PEA} = 0 mm), significant subambient temperatures ($\Delta T \lesssim 0$ °C) are not achievable (*i.e.*, $P_{cool} < 0$ W/m²) due to dominant solar heating and parasitic heat gain. However, increasing t_{PEA} reduces solar absorption and parasitic heat gain at the emitter, enabling lower temperatures (up to ΔT = -7 °C and ΔT = -11 °C for daytime and nighttime respectively) and higher cooling powers. A maximum cooling power (indicated by the dot symbol) is also observed for each ΔT curves, highlighting the compromise between the decreasing infrared transmittance and increasing solar reflectance and thermal insulation associated with thicker PEA. Furthermore, an increasing t_{PEA} for $\Delta T > 0$ °C decreases P_{cool} as convection now positively contributes to the emitter cooling. In general, similar trends are observed between daytime and nighttime operation, although the nighttime performance allows us to decouple solar absorption in the PEA and emitter from the thermally insulating property of the PEA. It is also important to recognize that results presented in Figure 19 can be strongly influenced by the atmospheric conditions specific to a location and time such as the amount of precipitable water vapor, solar irradiance, cloud cover, surrounding objects or buildings, and these conditions should therefore be accounted for [55]. We thus show that lower subambient temperatures and higher subambient cooling powers are possible for both daytime and nighttime operation when using an OSTI cover such as PEA.

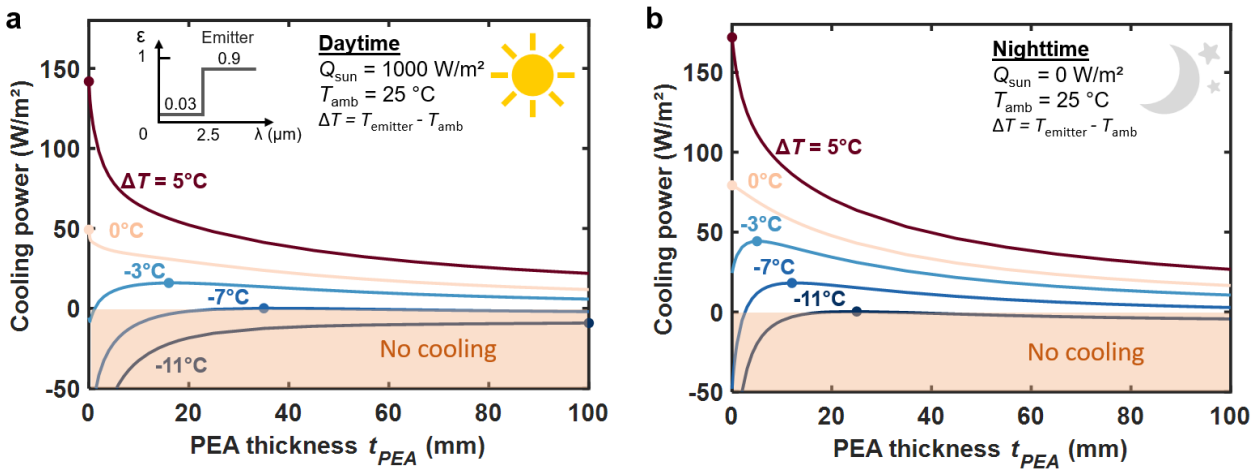

Figure 19 – ***Performance of radiative coolers with PEA.*** *(a) Daytime cooling performance of a semi-ideal selective emitter (ρ_{solar} = 1 - α_{solar} = 0.97 and ε_{IR} = 0.9) at different temperatures ($\Delta T = T_{emitter} - T_{amb}$). The maximum cooling power is shown by a solid point for each emitter temperature curve. An optimal aerogel thickness exists to achieve the maximum cooling power at a given emitter temperature. The results shown were calculated based on the U.S. Standard Atmosphere 1976. Atmospheric conditions specific to a location and time such as humidity and cloud cover can significantly affect the results and should be accounted for accordingly* [55]. *(b) Results for nighttime cooling performance. Higher cooling power and lower emitter temperatures can be achieved due to the absence of solar irradiation.*

3.5. EXPERIMENTAL SETUP AND METHODS

We designed a proof-of-concept experimental setup (Figure 20[a-c]) to simultaneously compare the performance of two radiative coolers – one with PEA and one without.

Each radiative cooler possessed an identical 10-cm diameter two-part selective emitter made from a 3M Enhanced Specular Reflector (ESR) film on top of polished aluminum ($\rho_{solar} = 0.942$; $\varepsilon_{8\text{-}13\ \mu m} = 0.893$; see Figure 20d for optical properties). The two parts of the emitter consisted of a 5 cm diameter *main* emitter in the center, surrounded by a 10 cm diameter *guard* emitter with a separation gap of 0.5 mm. The separation of the emitter in two parts is a similar approach to the one used in the guarded-hot-plate thermal conductivity measurement standard test method [90]. This approach limits any 2D heat transfer effects to the *guard* emitter and ensures 1D heat transfer at the *main* emitter, thus replicating the performance of a large-scale device not affected by side losses. Heaters (custom fabricated from Inconel sheet cut on the water jet) as well as T-type thermocouples (TT-T-40-SLE-25, Omega) were attached to the back of the (*main* and *guard*) emitters to enable control and measurement of their temperature. The thermocouples were connected to a DAQ enclosed in a reflective aluminum box to minimize temperature gradients between the thermocouple junctions and the DAQ cold junction sensors. The thermocouples were also calibrated before the experiments in an ethylene glycol solution using a chiller (A25, Thermo Scientific) and a resistance temperature detector (RTD) (P-M-A-1/4-3-1/2-PS-12, Omega) which resulted in an uncertainty of ± 0.3°C. Power supplies (2425, Keithley; 2440, Keithley and 2230-30-1, Keithley) were used in a 4-wire and 2-wire configuration at the *main* and *guard* heaters respectively for accurate control of their temperature and measurement of their power consumption. A 0.5-mm thick thermally conductive copper plate was also placed between each heater and emitter to minimize temperature gradients at the emitter. The emitter/heater assembly rested on top of a highly insulating vacuum insulation panel (VIP; Thermal Vision THRESHHOLD™; 23 × 23 × 5 cm; $k_{VIP} = 2.9$ mW/mK) which in turn sat at the bottom of a polystyrene foam (FOAMULAR® 150) box (30 × 30 × 15 cm), minimizing the parasitic heat gains at the backside of the emitter. The horizontal surfaces of the setups were covered with Tefzel™ coated aluminum to minimize parasitic solar heating of the box, and the inner vertical walls of the polystyrene foam box were covered with polished aluminum sheets to maximize the view factor between the emitter and the sky. Different thicknesses of PEA were achieved by stacking standard 6-mm thick samples.

During our outdoor experiments, a Campbell Scientific CS215 probe was used to measure the ambient temperature (accuracy of ± 0.4°C between 5° to 40°C) and relative humidity (accuracy of ± 4% between 0% to 100%). The wind speed was measured using an anemometer (034B, Met One) with an uncertainty of 0.1 m/s within the wind speed range of our experiment. The GHI solar irradiance was measured using a

pyranometer (CMP6, Kipp & Zonen) with an uncertainty of ± 2.3%. A rotating shadowband radiometer (RSR2, Campbell Scientific equipped with LI-200R, LI-COR photovoltaic pyranometer) was also used as a backup irradiance measurement system and was in excellent agreement with the pyranometer. All instruments were connected to a datalogger (CR1000, Campbell Scientific). All weather data was sampled every three seconds and averaged every minute.

The data acquisition of all instruments and PID control of the heaters in the experiments was done using LabVIEW.

The uncertainty of the emitter temperature was determined from the thermocouple and ambient temperature sensor accuracy as well as their fluctuations during the averaging period (two-minute average after stabilization of the emitter temperature for the cooling power experiments or the 30-minute averaging period for stagnation temperature). The cooling power uncertainty was determined after accounting for the accuracy of the *main* emitter area measurement and of the power supplies, the *main* heater power fluctuations during the averaging period as well as the small parasitic lateral heat transfer between the *main* and *guard* emitters. Specifically, we performed an indoor measurement to characterize the lateral heat transfer coefficient between the *main* and *guard* emitters and found it to be 24.5 W/m²K, meaning that for every degree in temperature difference, an effective change in cooling power of 24.5 W/m² was observed at the *main* emitter. This effect was however only found to be important near the stagnation temperature of the devices. In fact, due to higher parasitic heat gain and low cooling power close to the stagnation temperature, the *guard* temperature was higher than the *main* emitter, causing heat transfer between the two emitters and giving rise to additional 2-D parasitic heat gains at the *main* emitter. Since all other data points and the model assume 1-D heat transfer at the *main* emitter, the cooling power data point at the stagnation temperature of both devices was removed.

With two identical devices in which the PEA thickness can be controlled, we can directly evaluate the benefits of PEA for radiative cooling and validate our theoretical model.

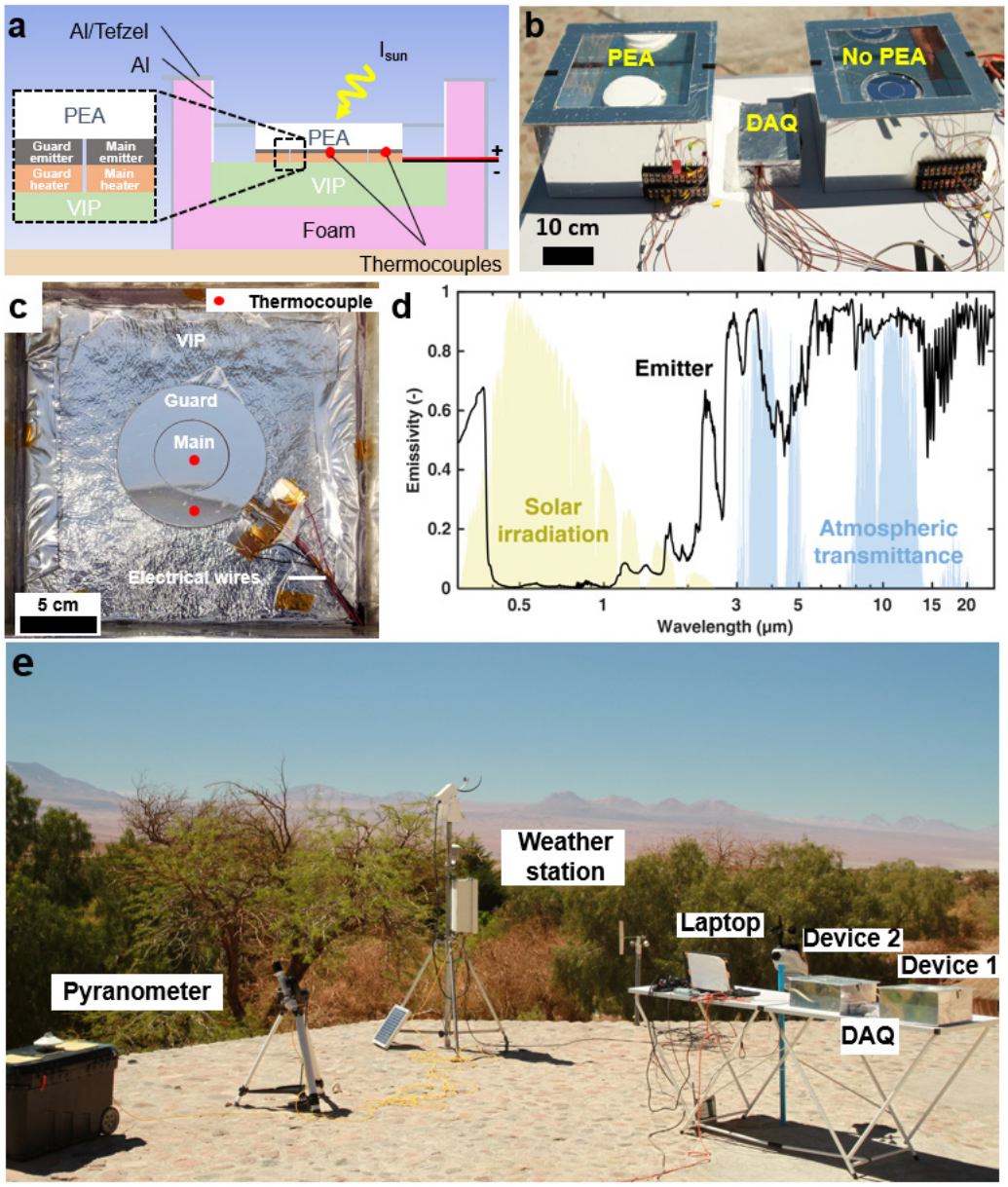

*Figure 20 – **Experimental setup**. (a) Schematic of the radiative cooler. A PEA/emitter/heater assembly is placed on top of a vacuum insulation panel (VIP) which sits inside a thermally insulating foam (FOAMULAR® 150) box. The box is covered with Tefzel™ coated polished aluminum sheets to minimize solar heating. The emitter/heater consists of two separate parts – the main emitter/heater and the guard emitter/heater (see inset). (b) Picture of the setup consisting of two identical devices (left: device with PEA, right: device with no PEA). A DAQ (enclosed in an aluminum box) is also visible. (c) Top view of a radiative cooling device showing the main and guard emitters, the VIP, electrical wires for the heaters and thermocouples as well as the location of the thermocouples beneath the emitters. (d) Emitter emissivity. A 3M Enhanced Specular Reflector (ESR) film was attached to a polished 0.5 mm thick aluminum sheet using an optically clear adhesive (Thorlabs OCA8146-2). The emitter was measured to have a solar weighted reflectivity ρ_{solar} = 0.942, and an emissivity of $\varepsilon_{8\text{-}13\mu m}$ = 0.878 within the atmospheric spectral window (e) The experiments were done in early October 2018 in San Pedro de Atacama, Chile at an altitude of 2476 m. The picture shows the location of the experiment along with solar (pyranometer and rotating shadowband radiometer) and weather monitoring equipment, the data acquisition system and the radiative coolers.*

3.6. EXPERIMENTAL RESULTS

Our first experiment focused on measuring the minimum stagnation temperature of the two devices – one with 12-mm thick PEA and one without PEA – over a full 24-h cycle, demonstrating both the daytime and nighttime benefits of PEA. Both devices were placed next to each other and exposed to direct sunlight as shown in Figure 20b. Figure 21a shows the temperature of both devices (*PEA* and *No PEA*) as well as the ambient (T_{amb}) temperature during the 24-h cycle. Figure 21b also shows the corresponding wind speed and solar global horizontal irradiance (GHI) measured during the experiment. During that 24-h period, the temperature of both devices closely tracked the ambient temperature and solar irradiance. However, the emitter with the PEA constantly maintained a much lower temperature than the uninsulated emitter due to the solar reflecting and thermally insulating nature of the PEA. Around solar noon (30-minute average around 13:22) at an average solar irradiance of 1123 W/m², a temperature difference with the ambient of ΔT = -13.0 °C was measured for the *PEA* device while the *No PEA* device only achieved ΔT = -1.7 °C. Similarly, around midnight, the *PEA* device achieved ΔT = -18.3 °C while the *No PEA* device reached ΔT = -8.4 °C. Moreover, the *No PEA* emitter temperature was more strongly influenced by wind than the *PEA* emitter (see temperature fluctuations in Figure 21a and the corresponding wind speed variations in Figure 21b), indicating the effectiveness of the PEA to reduce parasitic heat gain by adding an extra thermal resistance between the emitter and the ambient air. The combined high solar reflectance (modeled R_{solar} = 0.944 for 12 mm thick PEA) and added conduction thermal resistance (~ t_{PEA}/k_{PEA}) of the PEA enabled significantly lower emitter stagnation temperatures during both the day and night compared to an uninsulated high-performance selective emitter.

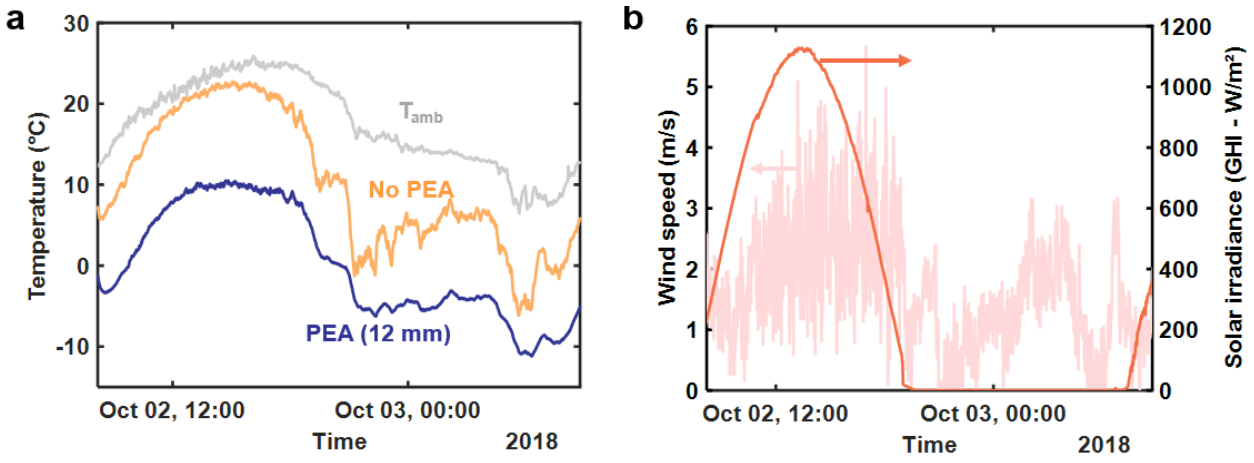

*Figure 21 – **Stagnation temperature of radiative cooler.** (a) Stagnation temperature of two devices (12-mm thick PEA and no PEA) over a 24-h period in early October in San Pedro de Atacama, Chile. The device with the PEA achieves 13°C sub-ambient cooling around solar noon (30-minute average around 13:22; GHI = 1123 W/m²) compared to 1.7°C without the PEA. (b) Wind speed and solar irradiation during the stagnation temperature experiment.*

We performed a second set of experiments to evaluate and compare the useful daytime cooling power at different PEA thicknesses. In one of these experiments (Figure 22[a-b]), we compare two extreme cases, an emitter covered with a thick (18 mm) layer of PEA (*PEA*) against an emitter without PEA (*No PEA*). In another similar experiment (Figure 22c), we compare two intermediate thicknesses (*6 mm PEA* vs *12 mm PEA*), demonstrating the variation in cooling performance with PEA thickness. We started the experiments by allowing the emitters to cool down to near steady-state conditions (see the *PEA* and *No PEA* emitter temperature in Figure 22a. We then increased the temperature of the (*main* and *guard*) emitters in a stepwise manner using the PID controlled heaters at their back side. At the same time, we measured the heater power at both *main* emitters as well as the ambient conditions (ambient temperature and humidity, wind speed and solar irradiance). The experimental cooling power was then obtained by normalizing the heater power, averaged over 2 minutes, by the *main* emitter area at every temperature step.

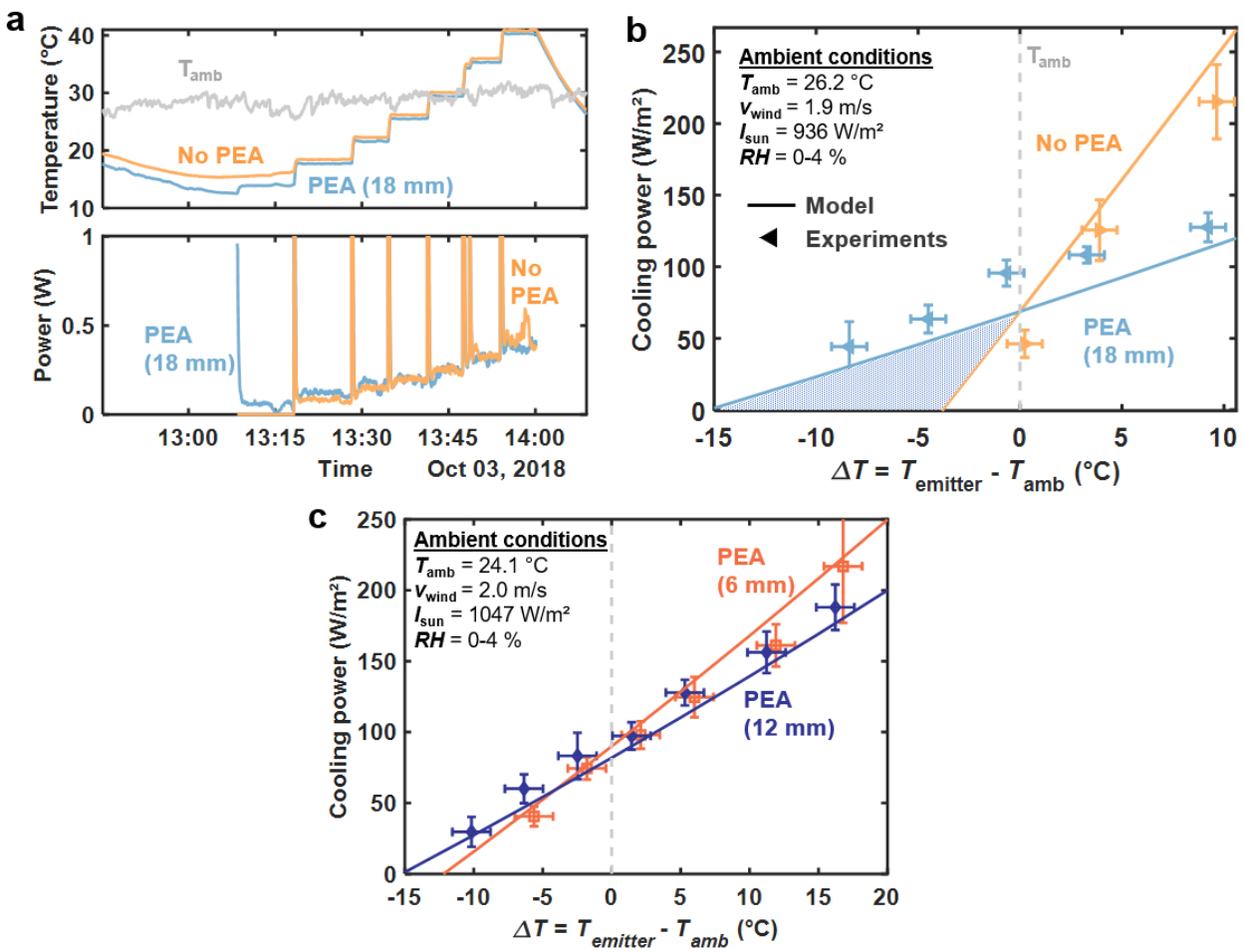

Figure 22 – ***Cooling performance of radiative cooler.*** *(a) Measured emitter temperature of two devices (18 mm thick PEA and no PEA) as well as the corresponding heater power and ambient temperature during the cooling power experiment. (b) Cooling power of the two devices as a function of the emitter sub-cooling in San Pedro de Atacama, Chile. The shaded area represents the range of cooling power and sub-ambient temperatures made accessible by the PEA compared to an uninsulated emitter. (c) Comparing the cooling power of two radiative coolers with different PEA thickness (6 mm vs 12 mm). Thicker PEA enables lower sub-ambient temperature and higher cooling power at sub-ambient temperatures. An intersection of the theoretical cooling power curves at ΔT = -4°C is observed, highlighting the necessity to optimize the PEA thickness for a given operation temperature.*

Figure 22b shows the theoretical (solid lines) and experimental (data points) emitter cooling power versus the emitter sub-cooling for the two devices (*PEA* and *No PEA*). The theoretical results were obtained using the model presented earlier and the atmospheric transmittance modeled based on the geographical location and the average weather conditions (see inset in Figure 22b) during the time of the experiments [67]. Experimentally, the cooling power of the 18 mm thick *PEA* device was 96 ± 9 W/m² near the ambient temperature ($\Delta T = -0.6 \pm 0.8$ °C) when the average solar irradiance was 936 W/m², compared to a cooling power of 46 ± 10 W/m² ($\Delta T = 0.2 \pm 0.8$ °C) for the *No PEA* device. Similar to the stagnation temperature experiment, the device with PEA also enabled lower sub-ambient temperatures (maximum

cooling up to ΔT = -15 °C compared to ΔT = -3.8 °C for the *No PEA* emitter according to the model) due to the added solar reflectance and thermal insulation. More specifically, by adding 18 mm of PEA on top of the emitter, we were able to reduce h_{eff} from 12.9 W/m²K to 1.4 W/m²K while the cover provided an additional solar reflectance R_{solar} = 0.948 as per our model. Overall, the experimental and theoretical results are in good agreement, demonstrating the potential of the model to predict the performance of a radiative cooler with PEA.

Differences between the experimental and theoretical results can be explained by the uncertainty in the measurements, the fluctuations in the ambient conditions, heat transfer from the emitter to the VIP and the theoretical model approximations including assuming 1D heat transfer (infinitively large emitter and PEA) and the azimuthally symmetric radiative heat transfer which requires the solar irradiation to be normal to the emitter. The uncertainty of the emitter temperature was determined from the thermocouple and ambient temperature sensor accuracy as well as their fluctuations during the averaging period (two-minute average after stabilization of the emitter temperature for the cooling power experiments or the 30-minute averaging period for stagnation temperature). The cooling power uncertainty was determined after accounting for the accuracy of the *main* emitter area measurement and of the power supplies, the *main* heater power fluctuations during the averaging period as well as the small parasitic lateral heat transfer between the *main* and *guard* emitters. Specifically, we performed an indoor measurement to characterize the lateral heat transfer coefficient between the *main* and *guard* emitters and found it to be 24.5 W/m²K, meaning that for every degree in temperature difference, an effective change in cooling power of 24.5 W/m² was observed at the *main* emitter. This effect was however only found to be important near the stagnation temperature of the devices. In fact, due to higher parasitic heat gain and low cooling power close to the stagnation temperature, the *guard* temperature was higher than the *main* emitter, causing heat transfer between the two emitters and giving rise to additional 2-D parasitic heat gains at the *main* emitter. Since all other data points and the model assume 1-D heat transfer at the *main* emitter, the cooling power data point at the stagnation temperature of both devices was removed.

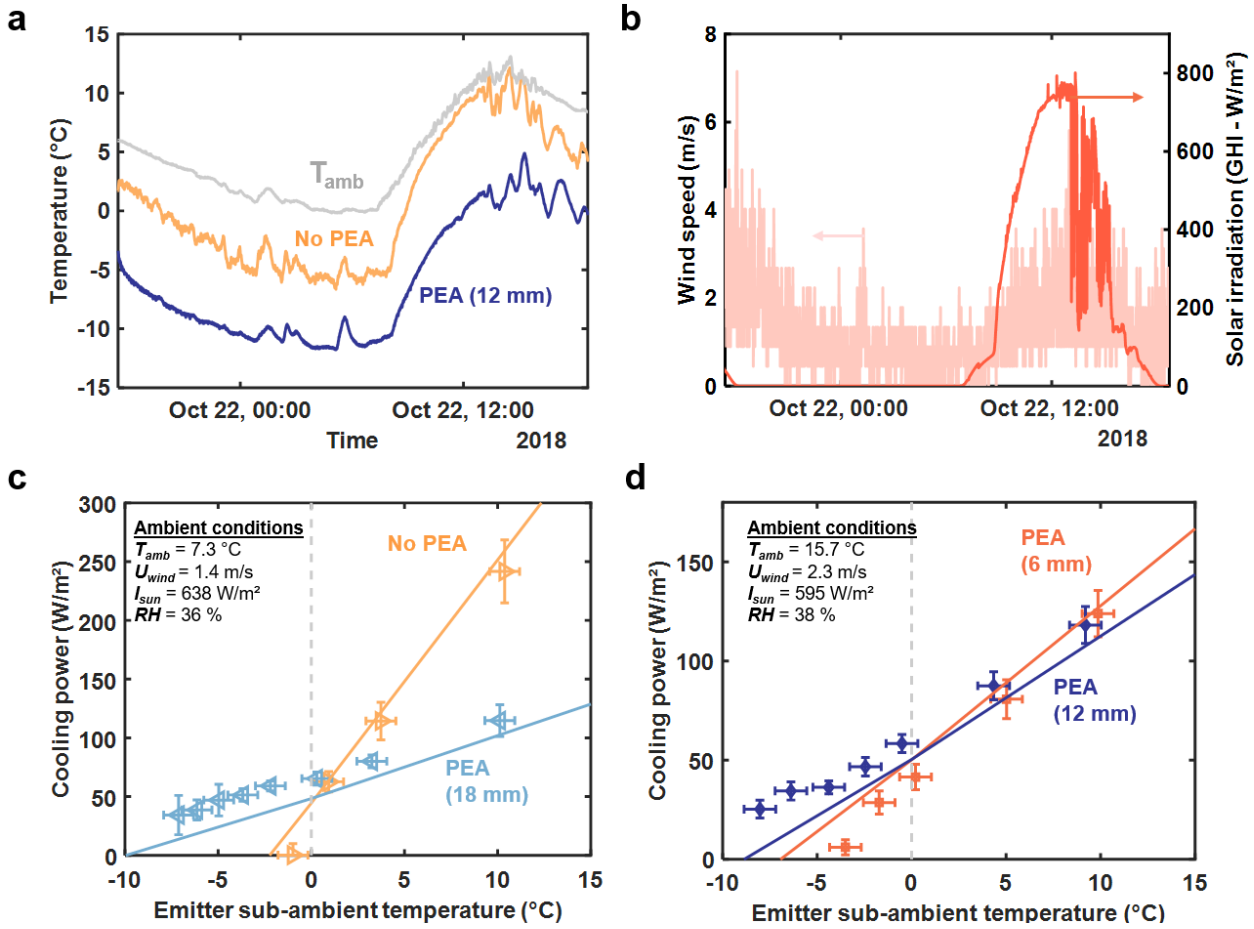

Figure 23 – ***Cooling performance of radiative cooler in Cambridge, Massachusetts.*** *(a) Stagnation temperature of two devices (12 mm thick PEA and no PEA) over a 24-h period in late October in Cambridge, Massachusetts. The device with the PEA achieves 9.8 °C sub-ambient cooling around solar noon (30-minute average around 12:43; GHI = 747 W/m²) compared to 1.1°C without the PEA. (b) Wind speed and solar irradiation during the stagnation temperature experiment. (c) Cooling power of two devices (18 mm thick PEA and no PEA) as a function of the emitter sub-cooling in Cambridge, Massachusetts. (d) Cooling power of two devices (6 mm thick PEA and 12 mm thick PEA) as a function of the emitter sub-cooling in Cambridge, Massachusetts.*

By using PEA in a radiative cooling device, we demonstrated higher subambient cooling power and operation at much lower temperatures than with an uninsulated selective emitter, opening up a wide regime of operation (shaded area in Figure 22b) that enables access to cooling powers and subambient temperatures that were previously not accessible.

3.7. DECOUPLING COOLING PERFORMANCE FROM EMITTER SOLAR REFLECTIVITY

A further advantage of using a PEA cover is that it relaxes the requirement to use a potentially complex and costly near-ideal solar reflecting emitter to achieve daytime radiative cooling. In fact, adding a 20 mm thick PEA to a black emitter reduces solar absorption by 98.9% (see Figure 24), which is better or comparable to state-of-the-art selective emitters. Furthermore, when combined with that same thickness of PEA, increasing the emitter solar reflectivity R_{solar} from 0 to 0.97 (typical of existing selective emitters) only reduces solar absorption at the emitter by a further 0.5%, meaning that the optical selectivity of the emitter is no longer critical when combined with PEA. Using a PEA cover or other type of optically selective cover could thus enable the use of simpler and lower cost emitters such as commercially available paints without compromising performance.

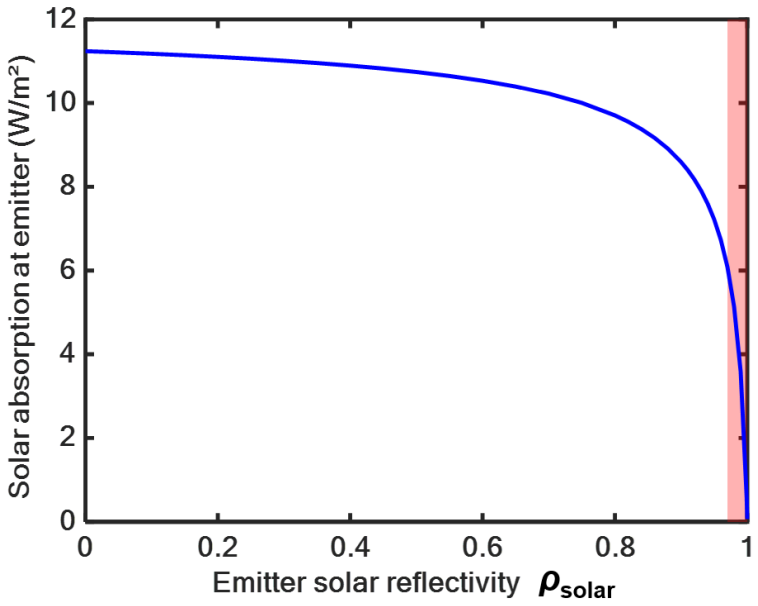

*Figure 24 – **Solar absorption at the emitter**. Absorption of incident solar irradiance (E_{sun} = 1000 W/m²) at an emitter with solar weighted reflectivity ρ_{solar} and with a 20 mm thick PEA. For a black emitter (ρ_{solar} = 0), the PEA reduces solar absorption at the emitter by 98.9% as compared to an emitter having no PEA. Higher ρ_{solar} further reduces solar absorption at the emitter from 11.2 W/m² at ρ_{solar} = 0, to 6.1 W/m² at ρ_{solar} = 0.97 to 0 W/m² at ρ_{solar} = 1. In practice, selective emitters typically have $R_{solar} \leq 0.97$ ($\rho_{solar} > 0.97$ shown by red area), meaning that the emitter solar reflectivity is mostly irrelevant due to the optical selectivity of the PEA.*

The advantage of using the solar reflectance of PEA to decouple solar absorption at the emitter from its optical properties is further demonstrated in outdoor experiments (see Figure 25). In these experiments, we show the influence of the emitter solar reflectance (black vs selective emitter) on the radiative cooling performance (temperature and cooling power) when covered with 18-mm thick PEA. Both devices

achieved similar subambient cooling throughout the day and night (see Figure 25[c-d]), demonstrating a difference of only 1.5 °C around solar noon (30-minute average around 12:43; GHI = 948 W/m²) and 0.6 °C around midnight (30-minute average around 0:00). Similarly, both devices showed similar cooling power and good subambient cooling due to strong suppression of solar irradiation by the PEA on top of the emitters (see Figure 25e). Finally, when the PEA cover was removed from the black emitter (Figure 25f), we observed a rapid increase in temperature from slightly below the ambient to around 50°C, again highlighting the solar reflecting properties of PEA.

These results further show good agreement with the model in two different regions of the world while also suggesting that PEA significantly minimizes the importance of the emitter solar reflectivity, and that an optimal PEA thickness (*i.e.*, maximizing cooling power) exists for a given sub-ambient temperature. By using PEA for radiative cooling, we enabled higher sub-ambient cooling power and operation at much lower temperatures than with an uninsulated selective emitter, opening up a wide regime of operation that enables access to cooling powers and sub-ambient temperatures that were previously not accessible.

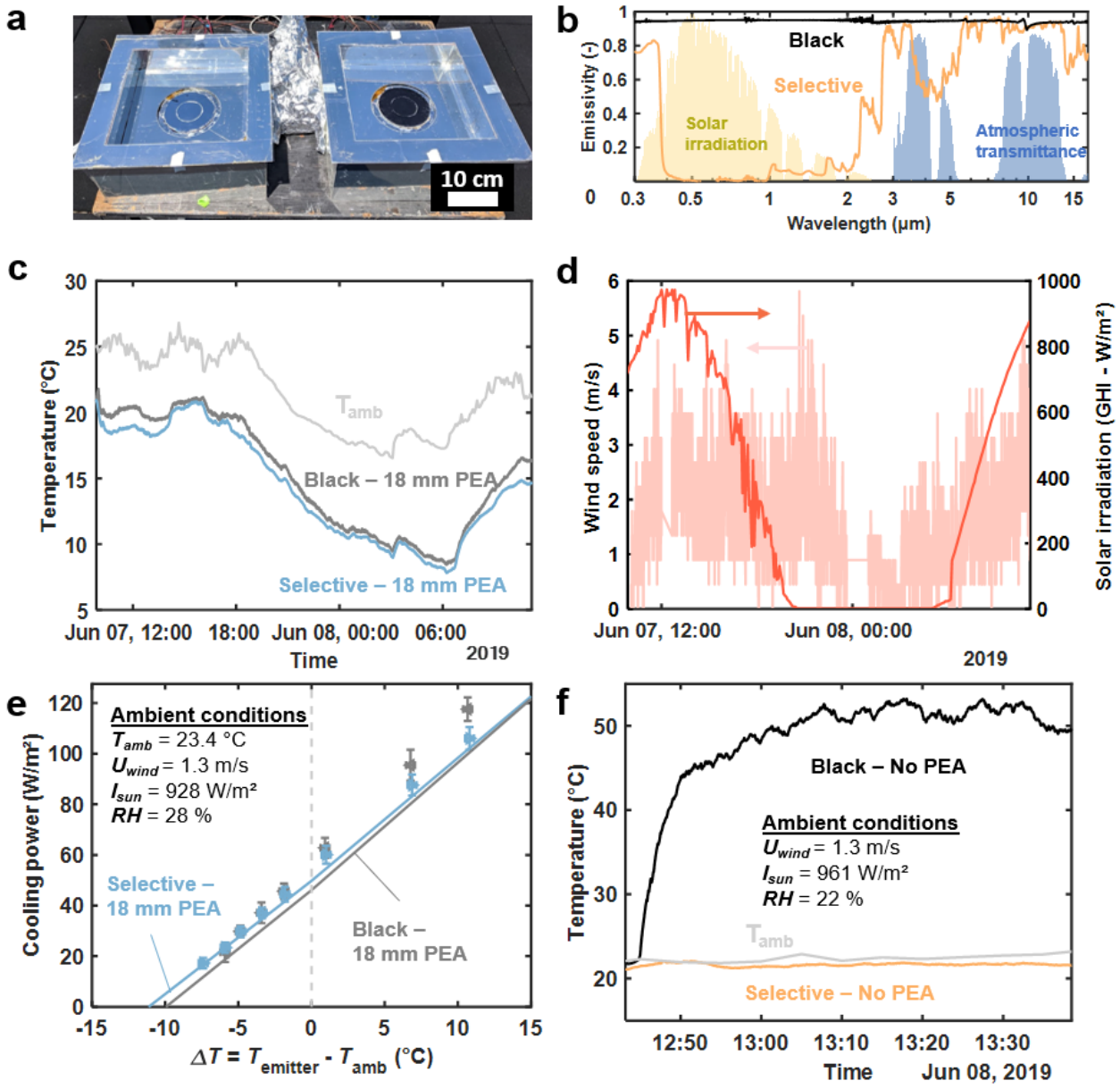

Figure 25 – ***Experimental comparison of selective and black emitters with PEA****. (a) Image of devices (selective emitter – left and black emitter – right) without the PEA. (b) Spectral emissivity of selective and black emitters. (c) Stagnation temperature of the two emitters, both with 18-mm thick PEA over a 24-h period in June in Cambridge, Massachusetts. (d) Wind speed and solar irradiation during the stagnation temperature experiment. (e) Cooling power of the two emitters, both with 18-mm thick PEA as a function of the emitter sub-cooling in Cambridge, Massachusetts. (f) Stagnation temperature of the two emitters with no PEA close to solar noon. The black emitter quickly heated up to over 50 °C after the aerogel was removed at 12:45.*

3.8. SUMMARY

We proposed and experimentally demonstrated the use of optically selective and thermally insulating PEA covers for high-performance subambient radiative cooling. By adding PEA on top of a radiative cooling emitter, we provided a simple approach to reducing parasitic heat gain and solar absorption at the emitter, two limiting factors that have severely hindered the performance of previous experimental demonstrations. Using PEA and a commercially available selective emitter, we experimentally demonstrated a daytime cooling power of 96 W/m² at ambient temperature as well as cooling of up to 13 °C below ambient, surpassing by more than 22% the performance of previous stagnation temperature experiments [55].

In parallel to our experiments, we also investigated the performance of PEA using a theoretical model considering both conductive and radiative heat transfer. The model provided us with insights on the compromise between system performance and PEA thickness which allowed us to determine an optimal PEA thickness for any given system, weather conditions and operating temperature. We have also demonstrated that due to its high solar reflectance, PEA allowed the use of non-selective emitters with no significant degradation in performance, possibly enabling simpler design and lower cost radiative coolers.

We believe our work has proven the potential of PEA and other types of optically selective and thermally insulating covers for subambient radiative cooling. Because the approach is modular and can readily be implemented in existing systems, our work can help improve the performance of existing radiative cooling systems such as radiative cooling water panels for air-conditioning units of buildings [55], [95], sorption-based water harvesting devices [96] as well as passive refrigeration of food produce [94]. Finally, we hope new research opportunities that will further enhance the performance of radiative coolers will stem from this work. Among such opportunities, alternative infrared transparent materials such as BaF_2 and ZnS [47], [93] could be explored to achieve better optical and thermal performance, and further development of the theoretical models to optimize the cover thickness and optical properties for varying weather conditions (*e.g.*, day to day variation over a year) as well as costs (*e.g.*, incremental increase in performance versus incremental cost with thicker PEA) are still required. In the next chapter, we propose adding ZnS inside PEA to increase the optical selectivity of the cover and achieve better daytime cooling performance.

3.9. MODEL ASSUMPTIONS

In developing our radiative transfer and heat transfer models, several assumptions were made. Here, we list some of our assumptions, which help understand the limitations of the model and explain some of the differences between modeling and experimental results.

- The RTE model relies on an estimation of the atmospheric transmittance and irradiance which is calculated using MODTRAN® 6.0 [67] (see Section 2.3.1). When comparing our experimental results to our theoretical model, differences between the real and modeled atmospheric transmittance and irradiance can affect the contribution of radiative cooling in our modeled cooling power as well as the stagnation temperature.
- The RTE model assumes 1D radiative heat transfer and thus that the solar irradiance (experimentally measured as GHI) hits the cooling architecture with a zenith angle of 0°. The solar zenith angle during our experiments in Chile was around 28° which could affect the path length and thus absorption of solar photons in the PEA during our experiments. Furthermore, this 1D assumption assumes that our PEA sample is infinitely large while the finite diameter of our actual samples might cause 2-D radiative flux near the circumference of the PEA, especially in the cooling power experiment where the side of the cooling stack was not insulated.
- The heat transfer model assumes a no flux condition at the bottom side of the emitter while in reality a small heat flux through the bottom boundary could exist due to non-ideal thermal insulation.
- Our heat transfer model assumes constant ambient conditions (solar GHI, ambient temperature, wind speed and RH) throughout the duration of the cooling power experiment or for the averaging period of the stagnation temperature experiments.
- Our heat transfer model does not account for uncertainties in the input model parameters such as solar GHI, ambient temperature, wind speed, RH, optical properties of PEA and the substrate, sky transmittance, PEA and PAH thermal conductivity, and PEA thickness. Accounting for those would lead to a band instead of a line for the modeling curves.

Chapter 4

4. Improving the Optical Selectivity of Polyethylene Aerogels

4.1. INTRODUCTION

In the previous chapter, we demonstrated how optically selective and thermally insulating (OSTI) covers such as polyethylene aerogel (PEA) could improve the performance of radiative cooling systems by minimizing solar absorption and parasitic heat gain at the emitter. Yet, while the cooling performance was certainly good, it was still far from that of an ideal radiative cooler with no solar absorption or parasitic heat gain. In fact, we showed that even with a 20-mm thick PEA, around 1.1% (11 W/m^2) of the solar irradiance made it to the emitter, which might seem small, but is equivalent to around 10% of the ambient cooling power of the emitter. At the same time, we also saw the compromise of PEA thickness and subambient cooling power in Figure 19, where the thicker PEA helped decrease parasitic heat gain, but also hindered radiative transfer. The development of OSTI covers therefore involves optimization of competing optical – solar transmittance (T_{solar}) and reflectance (ρ_{solar}), IR transmittance (τ_{IR}), and thermal properties – thermal conductivity of the cover material (k_{PEA}). Optically, an ideal cover should have $T_{solar} = 0$ ($\rho_{solar} = 1$) (Figure 26a) to minimize solar absorption at the emitter and within the OSTI cover, and $\tau_{IR} = 1$ to maximize IR rejection from the emitter to outer space. Experimentally achieving such optical selectivity is however challenging and limited by the porous structure and fabrication process such as in the case of PEA. As the thickness (or density) of PEA samples is increased beyond a few millimeters, both the solar and IR transmittance decrease (at different rates as we demonstrated in Figure 9) due to increasing scattering of light by the porous structure in the solar spectrum and non-zero absorption of polyethylene in the IR respectively. PEA samples with relatively low density (~15 kg/m^3) were used in past work to achieve $T_{solar} = 0.06$ ($\rho_{solar} = 0.92$) and $\tau_{IR} = 0.80$ at a thickness of 6 mm [70]. Significantly better optical properties – approaching that of an ideal cover – are likely possible and could yield significant gains in cooling performance while lowering cost by reducing the required OSTI cover thickness and allowing the use of low-cost non-selective scalable emitters.

Past work have investigated varying the scattering size and geometry [44]–[46], [97], [98], adding organic/inorganic micro/nano inclusions [93], [99], [100] or using hierarchically microstructures [34], [45] to improve the optical selectivity of porous polymeric materials. However, these approaches have not been demonstrated experimentally for OSTI covers.

In this work, we propose using IR transparent and solar scattering ZnS nanoparticles to enhance the optical selectivity of PEA covers for daytime radiative cooling (Figure 26c). Our work builds on past works [93], [101]–[105] that have demonstrated or proposed the use of BaF_2, ZnS, ZnO, ZnSe and TiO_2 nanoparticles to decrease solar transmittance (while maintaining high IR transmittance) of clear polyethylene films or porous polyethylene. We chose semiconducting ZnS (bandgap = 3.54 eV) due to its relatively high real refractive index [106] in the solar spectrum ($n = 2.29$ at 1 μm) and low imaginary refractive index at IR wavelengths ($k = 6\times10^{-6}$ at 10 μm), making it an ideal candidate for a solar scattering and IR transparent material (see Figure 27a). We first theoretically investigate the effect of ZnS concentration and particle size on the optical properties of PEA + ZnS covers by using the radiative transfer equation (RTE) and Mie theory. We then compare and show good agreement between our model and experimentally measured optical properties of PEA + ZnS samples at different ZnS volume fractions using commercially available ZnS nanoparticles (SACHTOLITH HD-S). Next, we investigate the influence of ZnS on the cooling performance of radiative coolers under direct sunlight – demonstrating up to 58 W/m² higher cooling power with a ZnS pigmented PEA cover combined with a blackbody emitter compared to an unpigmented PEA cover. Finally, we analyze the effect of ZnS spatial distribution within the OSTI cover – indicating that a higher ZnS concentration near the ambient air interface can result in higher cooling power while using less ZnS.

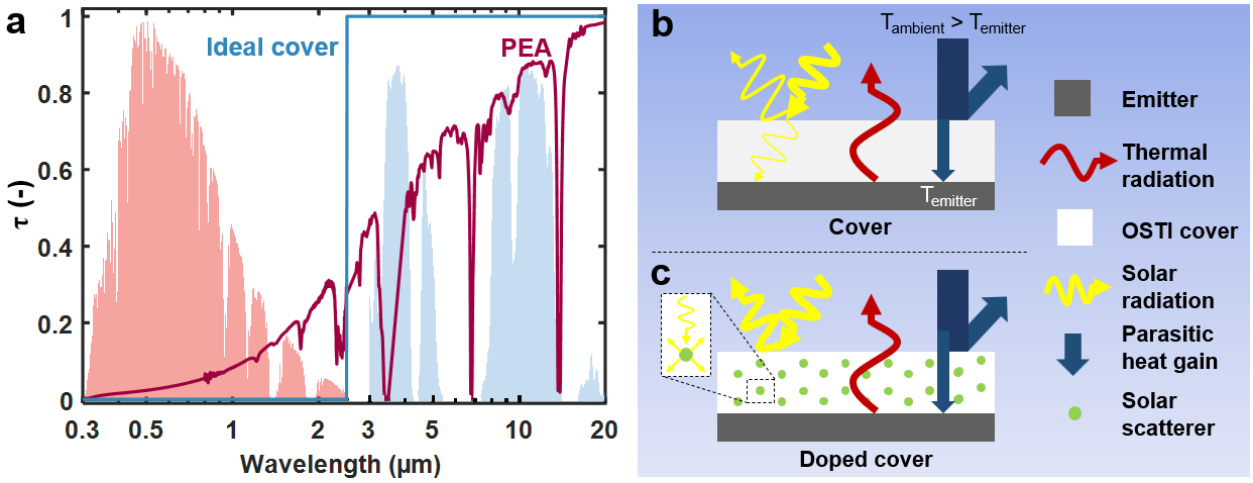

*Figure 26 – **Improving the optical selectivity of OSTI covers**. (a) Comparing the transmittance of an ideal (Ideal cover) and recently demonstrated 5-mm thick polyethylene aerogel (PEA) cover*[70]*. For reference, the solar spectrum (shaded red area) and the U.S. Standard 1976* [67] *atmospheric transmittance (shaded light blue area) are also shown for reference. (b) Optically selective and thermally insulating (OSTI) covers enable subambient radiative cooling of the emitter by minimizing parasitic solar absorption and heat gain from the ambient air. (c) Solar scattering dopants in OSTI covers enable significant increase in solar reflectivity resulting in improved cooling performance.*

4.2. MODELING OPTICAL PROPERTIES OF ZNS DOPED OSTI COVER

Our modeling approach first uses the radiative transfer equation (RTE) (Eq. (7)) to solve for the spectral transmittance and reflectance of the OSTI covers based on the material's optical properties. Radiative transport is then coupled with heat conduction within the cover using the heat equation to estimate the cooling power of an emitter shielded with an OSTI cover. As this modeling framework is similar to the one presented in Section 3.3, we will only highlight the main differences here.

Solving the RTE requires knowledge of the optical properties (ω, β and p) of all components of the medium (PEA and ZnS). By assuming independent scattering from the ZnS nanoparticles and PEA, we may sum up the contributions of both constituents to evaluate the medium's total optical properties [89]. Similar to previous work [68], [70], and based on the Henyey-Greenstein [66] approximation (which uses a single asymmetry factor g to represent the angular dependent scattering phase function p), we evaluated the PEA's ω, β and p using experimental measurements of hemispherical transmittance and reflectance, and direct transmittance of an unpigmented PEA sample. To evaluate the ZnS nanoparticle optical properties (ω, β and p), we used the Mie theory [89], [107] assuming independent scattering by spherical particles of known size, refractive index and volume fraction. We assume that the ZnS nanoparticles have a uniform size distribution, are located on the surface of the polyethylene backbone (*i.e.*, they are not embedded inside the polyethylene lamellae) such that they are surrounded by air only and that scattering of light by individual ZnS nanoparticles is not affected by the polyethylene backbone as well as by other surrounding ZnS nanoparticles. Since we have assumed independent scattering, we can then estimate the total optical properties of the OSTI cover by adding [89] the individual contributions of the PEA and ZnS nanoparticles:

$$\sigma_{sca,\lambda} = C_{sca,\lambda,PEA}N_{t,PEA} + C_{sca,\lambda,ZnS}N_{t,ZnS}, \tag{22}$$

$$\sigma_{abs,\lambda} = C_{abs,\lambda,PEA}N_{t,PEA} + C_{abs,\lambda,ZnS}N_{t,ZnS}, \tag{23}$$

$$\beta_{\lambda} = \sigma_{sca,\lambda} + \sigma_{abs,\lambda}, \tag{24}$$

$$g_{\lambda} = \frac{g_{\lambda,PEA}C_{sca,\lambda,PEA}N_{t,PEA} + g_{\lambda,ZnS}C_{sca,\lambda,ZnS}N_{t,ZnS}}{\sigma_{sca,\lambda}}, \tag{25}$$

where $\sigma_{\mathrm{sca},\lambda}$ and $\sigma_{\mathrm{abs},\lambda}$ are the spectral scattering and absorption coefficients (m^{-1}), $C_{\mathrm{sca},\lambda}$ and $C_{\mathrm{abs},\lambda}$ are the spectral scattering and absorption cross-sections (m^2), $N_{t,ZnS}$ is the number of particles per unit volume

(m^{-3}) and g is the asymmetry factor of the Henyey-Greenstein phase function approximation [66]. For reference, we show in Figure 27b the spectral absorption and scattering cross-sections of ZnS particles at different diameters, where we observe that larger ZnS particles scatter, as expected, more at longer wavelengths. Aside from the different optical properties, we solve for the RTE and the heat equation in a similar way as previous chapters.

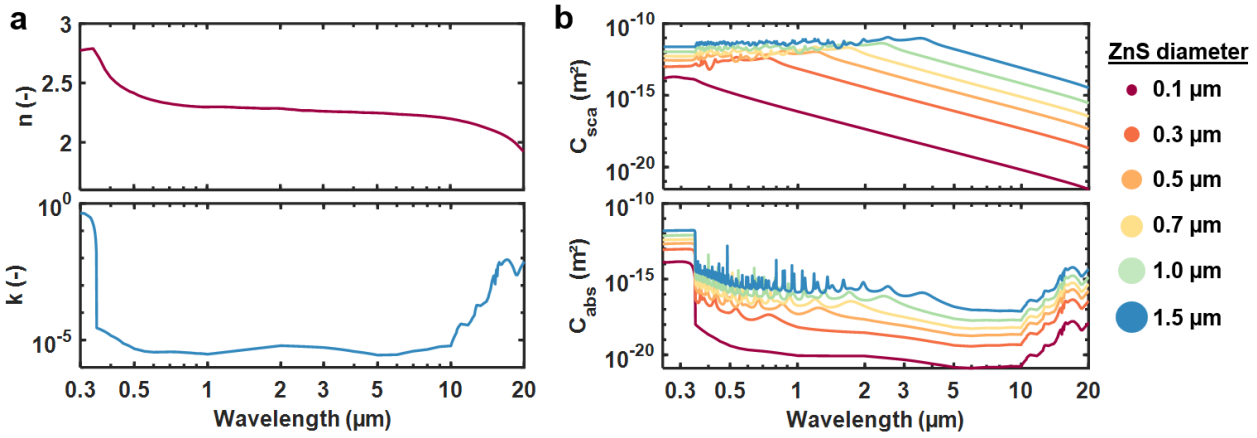

*Figure 27 – **ZnS optical properties**. (a) Real (top) and imaginary (bottom) part of the refractive index of ZnS* [106]. *(b) Scattering (C_{sca}; top) and absorption (C_{abs}; bottom) cross section of ZnS particles of different diameters.*

4.3. IMPROVING THE OPTICAL SELECTIVITY OF PEA COVERS USING ZNS

Figure 28a shows the theoretical hemispherical transmittance (τ, top) and reflectance (ρ, bottom) of 5-mm thick PEA with ZnS nanoparticles as well as the normalized solar spectrum (red area) and sky transmittance (blue area). Results are shown for PEA pigmented with different ZnS diameters (0.1 to 1.5 μm) at a fixed ZnS volume fraction ($f_v = 0.007$), along with an unpigmented PEA sample (black dashed line in Figure 28a). Larger ZnS particles increase scattering at longer wavelengths, resulting in lower transmittance and higher reflectance across all wavelengths considered. We note that at the chosen ZnS volume fraction, solar transmittance is mostly suppressed for particle diameters ≥0.3 μm, while IR (8-13 μm) transmittance remains relatively constant for particle diameters ≤1 μm, suggesting an ideal particle diameter within that range to maximize optical selectivity of the cover. Figure 28b shows the weighted solar (τ_{solar}, top) and IR (τ_{IR}, bottom) transmittance for the different ZnS particle diameters as a function of ZnS volume fraction. We observe that for particle diameters ≥ 0.3 μm, even relatively low ZnS volume fractions ($f_v < 0.01$) can significantly reduce τ_{solar} from 0.07 to less than 0.01. On the other hand, very little change in IR transmittance τ_{IR} ($\tau_{IR} > 0.80$) is observed as we increase ZnS volume fraction, except for larger ZnS particles (≥ 1 μm) which tend to scatter more in that spectral range.

Overall, the theoretical results show that improved optical selectivity can be achieved by pigmenting existing PEA covers with appropriate ZnS concentration and particle diameter.

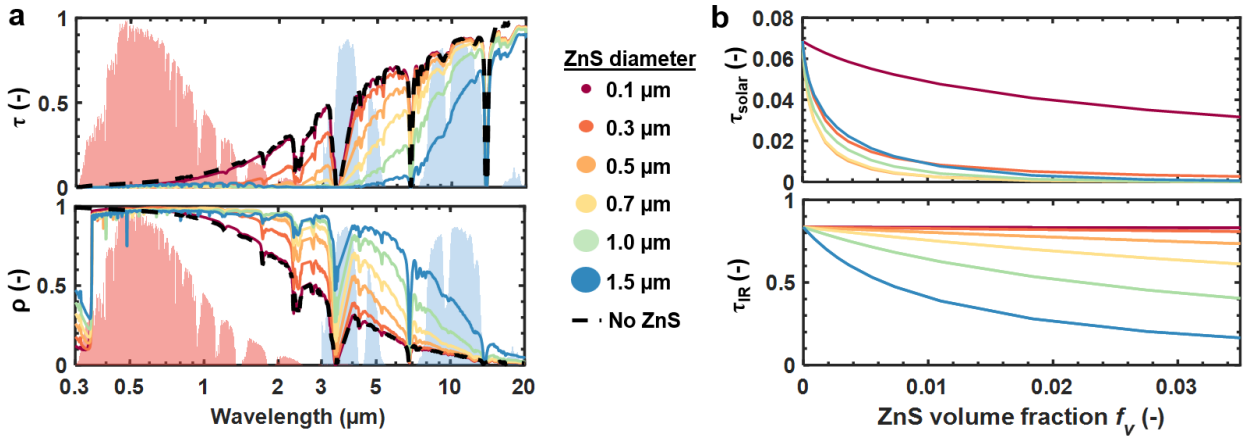

*Figure 28 – **Modeled optical properties of ZnS pigmented PEA**. (a) Modeled hemispherical transmittance (τ; top) and reflectance (ρ; bottom) of PEA pigmented with ZnS particles of different diameters. All curves assume a sample thickness of 5 mm and a ZnS volume fraction $f_v = 0.007$. (b) Modeled solar- (τ_{solar}; top) and infrared- (τ_{IR}; bottom) weighted transmittance of the ZnS doped PEA as a function of ZnS volume fraction and particle diameter.*

To experimentally demonstrate the improved optical selectivity, we fabricated 2-mm thick PEA samples (PEA-only density of 15 kg/m³) pigmented with various volume fractions ($f_v = 0$ to 0.044) of commercially available ZnS powder (SACHTOLITH HD-S; > 97% pure ZnS with particle diameter around 0.3 μm). We fabricated the samples using the same thermally induced phase separation fabrication process presented in Section 2.1. Different ZnS volume fractions in the PEA were achieved by mixing ZnS nanoparticles with polyethylene powder prior to sample preparation. We measured the samples' optical properties (hemispherical transmittance and reflectance) using an ultraviolet–visible–near-infrared spectrophotometer (Cary 4000, Agilent) and Fourier Transform Infrared spectrometer (Nicolet 6700, Thermo Scientific), each equipped with an integrating sphere. Results plotted in Figure 29a show similar trends to theoretical results – improved optical selectivity with large reduction in τ_{solar} achieved via addition of ZnS nanoparticles to PEA for a range of volume fractions. Additional absorption peaks between 8-9.5 μm, and stronger scattering in the IR are however observed in our experimental spectra compared to the theoretical spectra for pure ZnS (Figure 28a). We believe that the presence of contaminants [108] such as $BaSO_4$ (<3 wt. %) or ZnO (0.2 wt. %) within the commercial ZnS powder can incur additional absorption within the material. In fact, $BaSO_4$ has a strong absorption peak [37], [109] between 8-10 μm, which matches well with the additional absorption peak observed experimentally within that same spectral range. Furthermore, we note stronger scattering at IR wavelengths, suggesting possible agglomeration of ZnS particles in the fabricated samples. To further investigate these possible sources of discrepancy, we measured the optical properties of the SACHTOLITH HD-S ZnS powder

(Figure 30) and imaged the agglomeration of ZnS nanoparticles at different ZnS volume fractions (Figure 31) using a scanning helium ion microscope (Orion NanoFab, Zeiss). Our results confirm the presence of additional absorption in the 8-10 µm range as well as significant agglomeration of ZnS nanoparticles into agglomerates of sizes ranging from ~1 µm to several micrometers, with larger agglomerates observed at higher ZnS volume fractions.

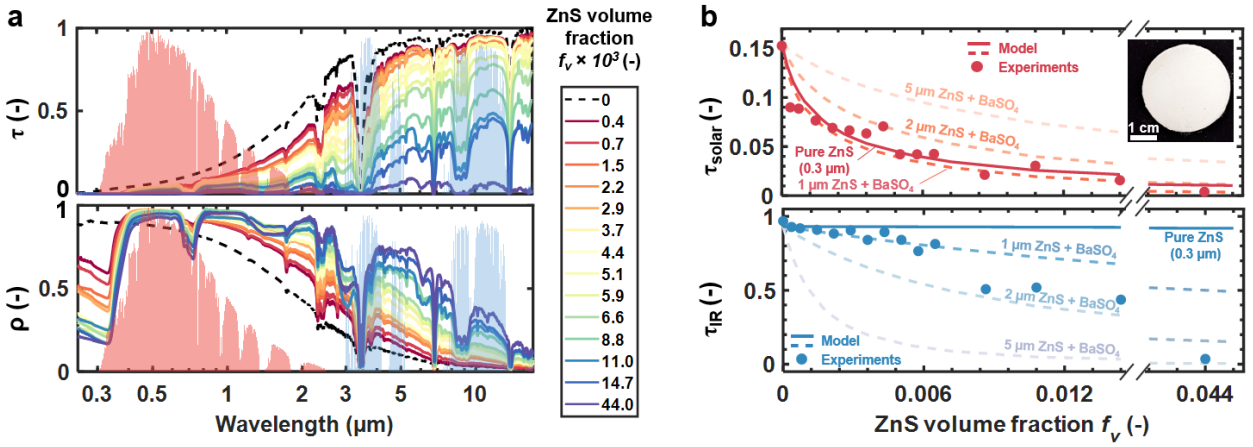

*Figure 29 – **Experimental optical properties of ZnS pigmented PEA**. (a) Experimental hemispherical transmittance (τ) and reflectance (ρ) of a 2-mm thick PEA doped with ZnS particles at different volume fractions. The PEA-only density was measured to be 15 kg/m³. (b) Experimental solar- (τ_{solar}; top) and infrared- (τ_{IR}; bottom) weighted transmittance and reflectance. Modeling results are represented by a solid line for the pure ZnS powder and by dashed lines for the SACHTOLITH HD-S ZnS powder to account for $BaSO_4$ content and ZnS agglomeration observed experimentally.*

The solar (τ_{solar}) and IR (τ_{IR}) weighted transmittance are also plotted in Figure 29b along with our theoretical model. Again, we observe that even a low ZnS volume fraction ($f_v \approx 0.006$) can drastically decrease τ_{solar} from 0.15 to less than 0.05, while only reducing τ_{IR} by ~0.1 for the 2-mm thick samples. Due to the differences between the pure ZnS considered in our earlier model and the commercially available ZnS powder used in our experiments, two sets of theoretical curves (solid line: pure ZnS and dashed lines: ZnS + $BaSO_4$) accounting for the optical properties and agglomeration of each powders are plotted in Figure 29b. The optical properties of both the pure ZnS and the SACHTOLITH HD-S used in Figure 29b were modeled using Mie theory with the latter accounting for both $BaSO_4$ and the effective ZnS agglomerates diameter. The three dashed lines represent our theoretical prediction using the SACHTOLITH HD-S with agglomerate diameters of 1 µm, 2 µm and 5 µm. In general, good agreement is observed between the experimental and theoretical transmittance, while some discrepancies, especially at larger ZnS concentrations, are observed for the IR transmittance compared to the pure ZnS. A comparison of experiments with our modeling of the commercially available ZnS powder, accounting for the presence of IR absorbing $BaSO_4$ and agglomeration of ZnS nanoparticles at larger volume fractions further supports our theory explaining the discrepancies. Overall, our theoretical and experimental results

show that the optical selectivity of PEA covers can be improved by adding small quantities of commercially available ZnS powder, and that even greater optical selectivity could be achieved by using 100% pure ZnS powder, paving the way for better sub-ambient radiative cooling under direct sunlight.

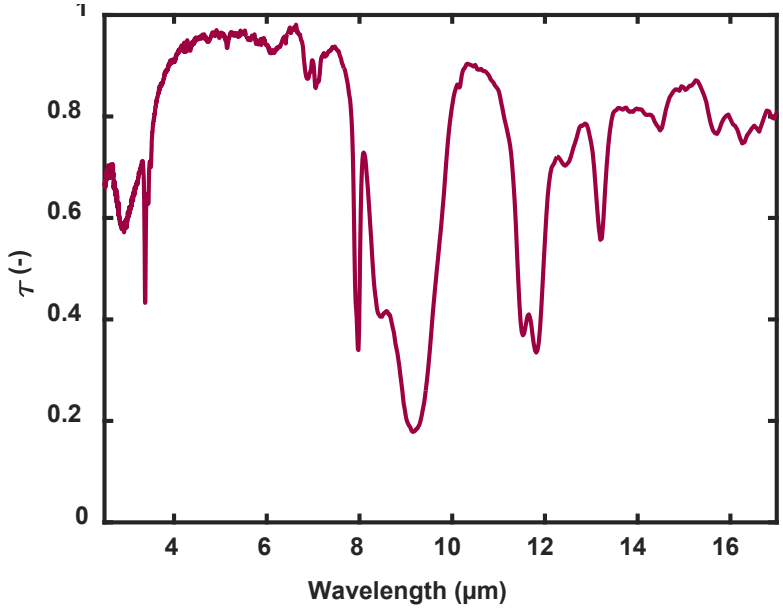

Figure 30 – ***SACHTOLITH HD-S ZnS infrared transmittance****. Infrared transmittance of a ~10-μm thick SACHTOLITH HD-S ZnS powder film. The powder was coated on top of a ZnSe window by evaporating an ethanol/ZnS mixture. The spectrum was corrected using the measured transmittance of an uncoated ZnSe window which was used as the reference. A strong absorption peak is observed between 8-10 μm, similar to our experimental results with ZnS pigmented PEA in Figure 29a. We note that this absorption peak was not found in our modeling of pure ZnS powder. We attribute this absorption peak to the presence of* $BaSO_4$ *in the SACHTOLITH HD-S powder, in accordance with the absorption spectrum of* $BaSO_4$ [37], [109].

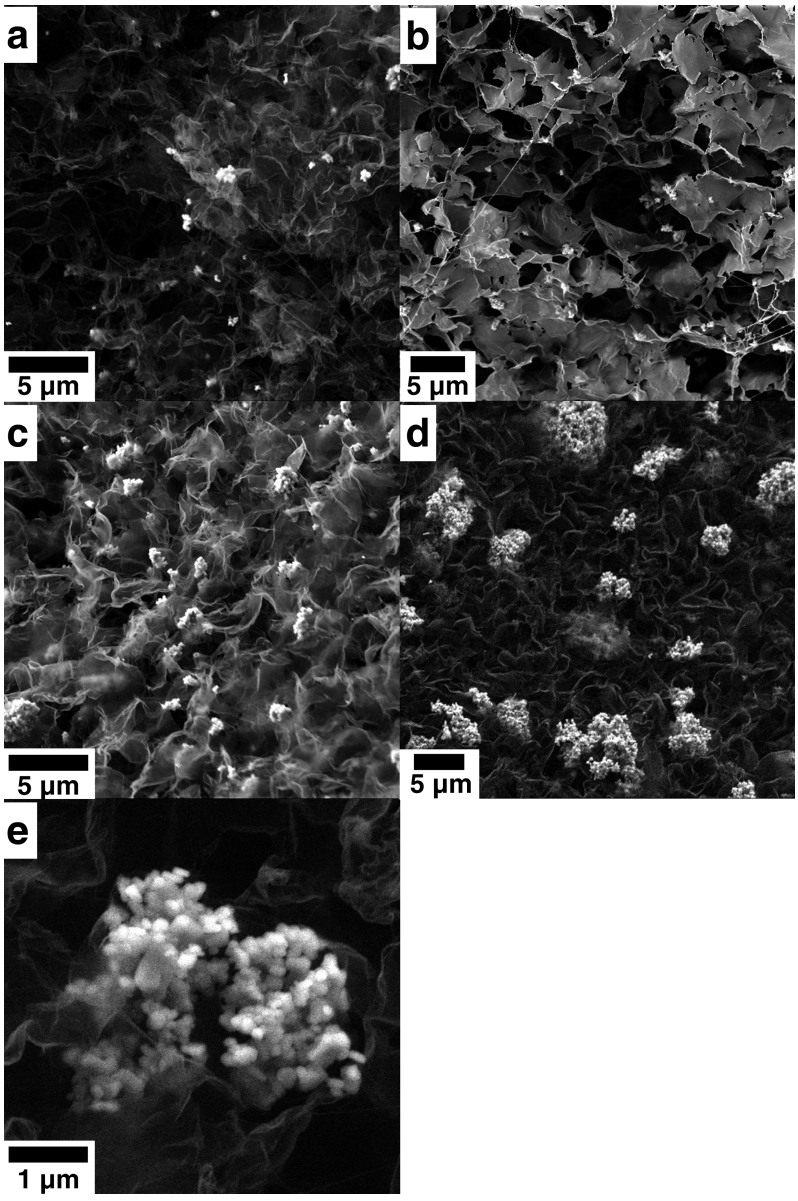

*Figure 31 – **ZnS particles agglomeration**. Agglomeration of ZnS particles in ZnS pigmented PEA observed under a helium-ion beam microscopy. ZnS agglomeration in ZnS volume fraction a) $f_v = 0.0022$; b) $f_v = 0.0079$; c) $f_v = 0.0157$; d) $f_v = 0.0315$. Close up view on an ZnS agglomerate in sample with $f_v = 0.0315$. Image credits: Geoffrey Vaartstra, Massachusetts Institute of Technology.*

4.4. IMPROVED COOLING PERFORMANCE USING PEA + ZNS COVERS

We have demonstrated that the optical selectivity of PEA covers could be improved by adding solar scattering and IR transparent ZnS nanoparticles. Next, we show how these covers can improve the subambient cooling power of radiative coolers.

Figure 32a shows the cooling power of a blackbody emitter ($T_{emitter} - T_{ambient}$ = -5 K) under direct sunlight (Q_{sun} = 1000 W/m²) and the *U.S. Standard 1976* sky shielded by a 5-mm thick PEA + ZnS cover. Similar to Figure 28, various ZnS particle diameters (d_{ZnS} = 0.1-1.5 μm) and volume fractions are considered. As illustrated in Figure 32a, no cooling (P_{cool} = -29.5 W/m²) is achieved with a conventional PEA cover (f_v = 0; *No ZnS* dashed line) due to significant solar absorption at the emitter. Increasing ZnS volume fraction reduces solar absorption at the emitter, resulting in higher cooling power until a reduction in IR transmittance causes it to plateau and then decrease. The influence of ZnS particle size again shows that an optimum particle size around 0.3-0.7 μm (depending on f_v) maximizes cooling power. A maximum cooling power of P_{cool} = 24.3 W/m² (d_{ZnS} = 0.5 μm; f_v = 0.015) is achieved within the range of parameters considered, representing a 53.8 W/m² increase in cooling power over the pure PEA cover case and demonstrating the potential of the approach to increase the cooling performance of daytime radiative coolers. A similar analysis is also performed for similar conditions but with an ideal selective emitter having an emissivity of ε = 1 between 8-13 μm and a reflectivity ρ = 1 at all other wavelengths. In this case, the cooling performance is not affected by solar absorption at the emitter because of its intrinsic ideal optical selectivity. Thus, the addition of ZnS to the cover will only reduce the cooling power due to reduced IR transmittance and additional solar absorption within the cover by the ZnS nanoparticles which in turn increases its temperature and parasitic heat gain. These results indicate that the improved optical selectivity of the cover is, as expected, more important for non-selective emitters. However, the ability to achieve similar cooling power with a blackbody emitter and an ideal selective emitter when combined with a PEA + ZnS cover suggests that the optical properties of the emitter in the solar spectrum are no longer the dominant parameter determining the cooling performance of the radiative cooler. As such, the optimized OSTI cover could be applied to any IR emissive surface to provide subambient cooling irrespective of its optical properties in the solar spectrum, which could be attractive as a retrofit solution or could help reduce the emitter complexity and cost. Finally, the increased optical selectivity of the cover can help decrease the required thickness to achieve net cooling, which could reduce the cover's cost.

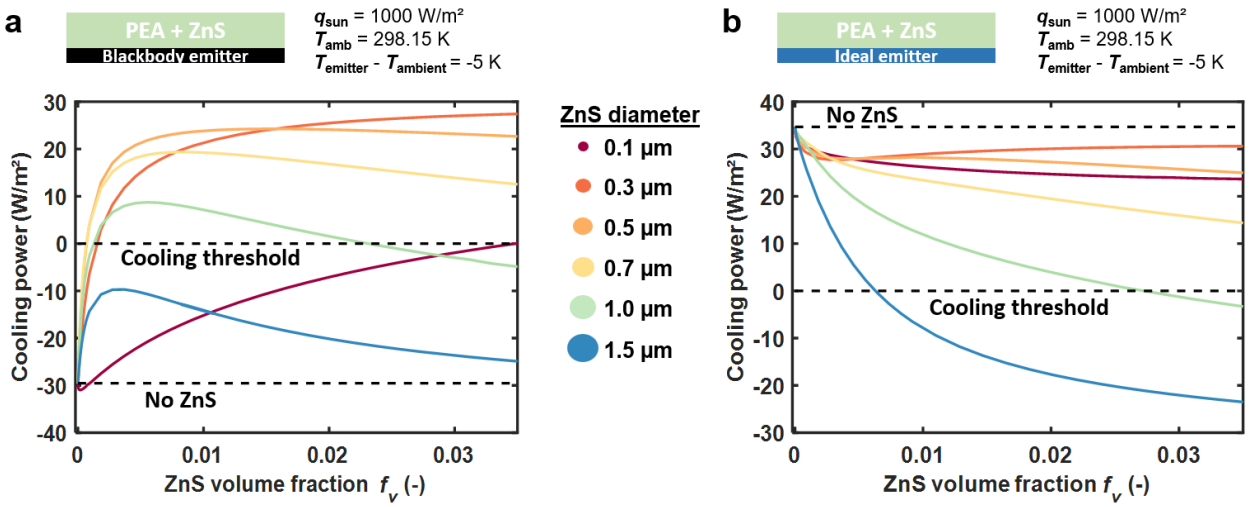

Figure 32 – ***Cooling performance using ZnS pigmented PEA covers****. Cooling power as a function of ZnS volume fraction (f_v) and particle diameter (d_{ZnS}) of (a) a blackbody emitter and (b) an ideal selective emitter (emissivity $\varepsilon = 1$ between 8-13 µm and reflectivity $\rho = 1$ at all other wavelengths) – both with 5-mm thick covers. An incident solar irradiance of 1000 W/m² normal to the emitter and an emitter temperature 5 K below the ambient ($T_{ambient}$ = 298.15 K) are assumed.*

4.5. OPTIMIZING ZNS DISTRIBUTION WITHIN PEA

We have until now assumed a uniform ZnS distribution within PEA for simplicity of modeling and fabrication. Further analysis of modeling results however suggests that the addition of ZnS within PEA raises the cover's internal temperature due to an increased parasitic solar absorption by the ZnS nanoparticles. This increased cover temperature in turn increases the parasitic heat conduction to the colder emitter through the cover which decreases cooling power, as was shown in Figure 32b. Ideally, we would like to suppress all parasitic solar absorption by the cover or spatially confine it as far as possible from the emitter (*i.e.*, closer to the ambient air) to minimize this parasitic conductive heat gain. We thus evaluate the impact of non-uniform ZnS distributions within the cover to see if it can enable higher cooling power for a subambient emitter.

Figure 33a depicts six different ZnS distribution profiles: *No ZnS*, *Constant*, *Linear +*, *Linear -*, *Top only*, *Emitter only*. The ZnS distribution profiles assume 50 evenly distributed 100-µm thick layers, a ZnS particle diameter of 0.5 µm and a fixed ZnS volume fraction (f_{ZnS} = 0.015) – corresponding to the volume fraction at maximum cooling power at the chosen particle diameter (see Figure 32a). Under similar conditions to those in Figure 32a, the daytime emitter cooling power is calculated for the different ZnS distribution profiles. The resulting temperature profiles and cooling powers are shown in Figure 33[b-c] respectively. We observe that all ZnS distributions increase the cover temperature as well as the temperature gradient near the emitter (see inset in Figure 33b) compared to the *No ZnS* case. While the

Bottom only distribution achieves the lowest temperature rise at the air-cover interface, it has the highest emitter-side temperature gradient (*i.e.*, larger conductive heat gain at the emitter) of all ZnS distribution profiles. On the other hand, lower temperature gradients near the emitter (*i.e.*, smaller conductive heat gains at the emitter) are achieved by covers with ZnS concentrated farther away from the emitter, such as the *Top only* cover. The effect of ZnS distribution within the OSTI cover is further illustrated in Figure 33c where the cooling power of each cover is compared. While all ZnS covers greatly surpass the *No ZnS* cover in terms of cooling power, differences are observed amongst the different ZnS distribution profiles. As suggested by the temperature profile in Figure 33b, covers localizing ZnS farther away from the emitter achieve higher cooling power, with the *Top only* case providing the highest cooling power (24.9 W/m² at ΔT = -5 K), representing a 0.6 W/m² (2.5%) improvement over the *Constant* profile case (24.3 W/m² at ΔT = -5 K). Although the improvement in cooling power over the *Constant* profile is rather small, the results however show that the *Bottom only* distribution should be avoided owing to its much lower cooling power (12.1 W/m² at ΔT = -5 K). Practically, we also realize that the *Linear* + and *Linear* – covers would be more difficult to fabricate as opposed to the other ZnS profiles. For example, in the case of the *Top only* cover, two covers could be installed on top of one another, one with ZnS and the other with no ZnS, to mimic a continuous cover with a step change in ZnS concentration. As such, we focus on the *Top only* ZnS distribution in Figure 33d to show that the volume fraction of ZnS (averaged over the whole cover thickness) can also be reduced using a non-constant ZnS distribution profile. The results show that the *Top only* profile can reduce ZnS volume fraction by 59% over the *Constant* profile at equal cooling power or can provide the best performance (25.3 W/m² vs 24.3 W/m² for the *Constant* profile) even at 30% lower ZnS volume fraction. Overall, our results indicate that while ZnS pigmentation of PEA can improve the subambient cooling performance, ZnS pigmentation at the top of the cover, close to the cover/ambient air interface, can provide the best performance while also minimizing the total amount of ZnS.

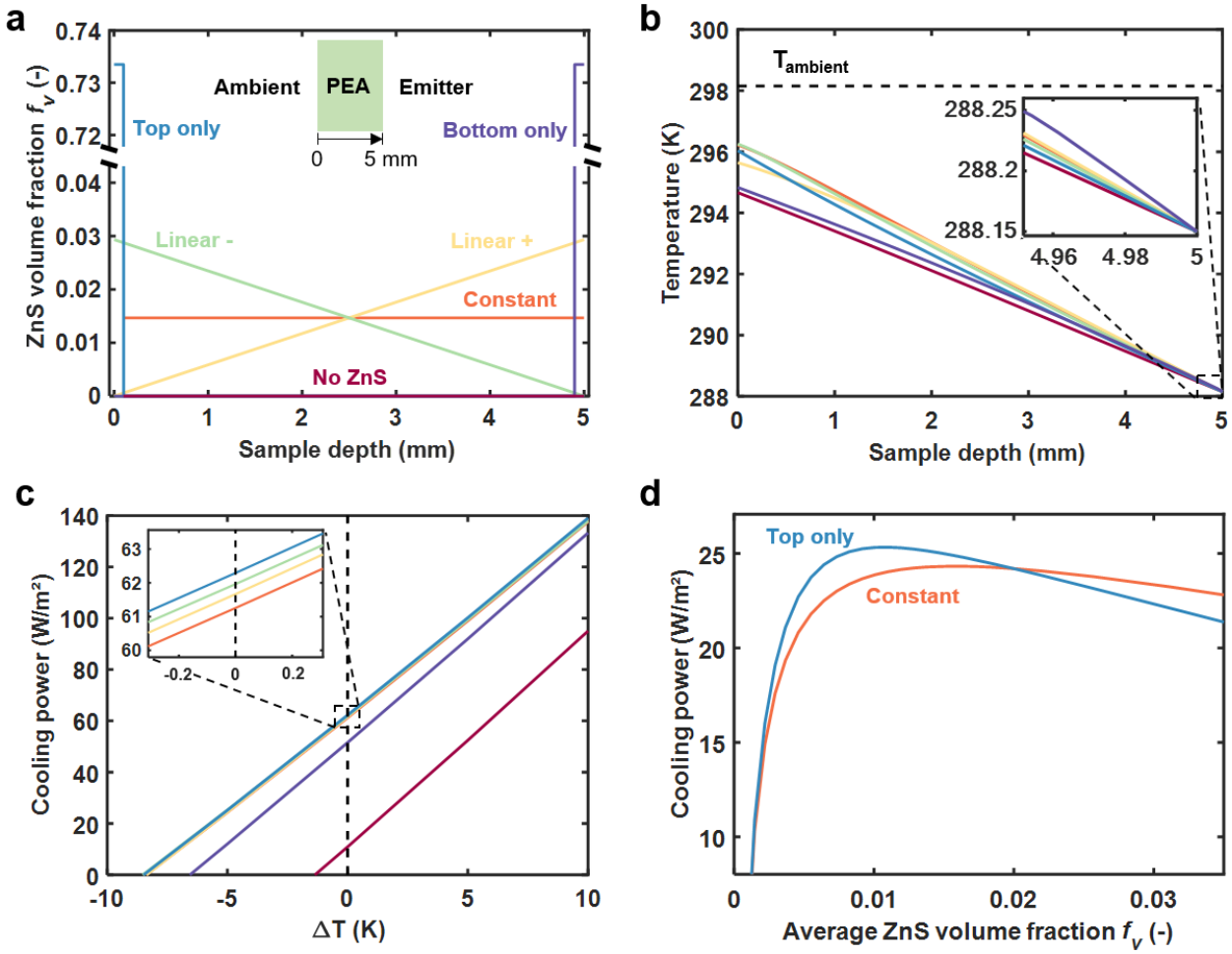

*Figure 33 – **ZnS distribution profile optimization**. (a) ZnS distribution profiles within PEA. (b) Temperature distribution within the cover for different ZnS distributions with the air side represented by sample depth = 0 mm and the emitter-side by sample depth = 5 mm. (c) Cooling power of a blackbody emitter + 5 mm thick PEA having different distributions of ZnS within it as a function of $\Delta T = T_{emitter} - T_{ambient}$. (d) Cooling power of the Top only and Constant ZnS distribution profiles as a function of average ZnS volume fraction. The Top only profile enables the highest cooling power at ΔT = -5 K, achieving 25.3 W/m² of cooling as opposed to 24.3 W/m² with Constant ZnS profile, while also using 30% less ZnS.*

4.6. INFLUENCE OF ZNS VOLUME FRACTION ON COVER THERMAL CONDUCTIVITY

As we increase the volume fraction of ZnS, it is reasonable to expect an increase in the thermal conductivity of the PEA + ZnS cover due to the high thermal conductivity of ZnS (k_{ZnS} = 27 W/mK [110]). To evaluate this hypothesis, we fabricated 10-cm diameter PEA samples with various ZnS volume fractions and measured their thermal conductivity in vacuum and in ambient pressure N_2 using our guarded-hot-plate thermal conductivity setup. The results are presented in Figure 34 and are compared to simple thermal models assuming a ZnS thermal conductivity of 27 W/mK and a PEA solid backbone

thermal conductivity of 0.0025 W/mK as measured in vacuum. The solid, gaseous, and radiative components of thermal conductivity were decomposed using modeling similar to Section 2.4.3.4 to decouple the impact of conduction through the ZnS from the added radiative resistance brought by the ZnS. We note that the uncertainty in the measurements only account for instrumental error of the thermal conductivity measurement and does not capture the modeling error on the radiative component of thermal conductivity.

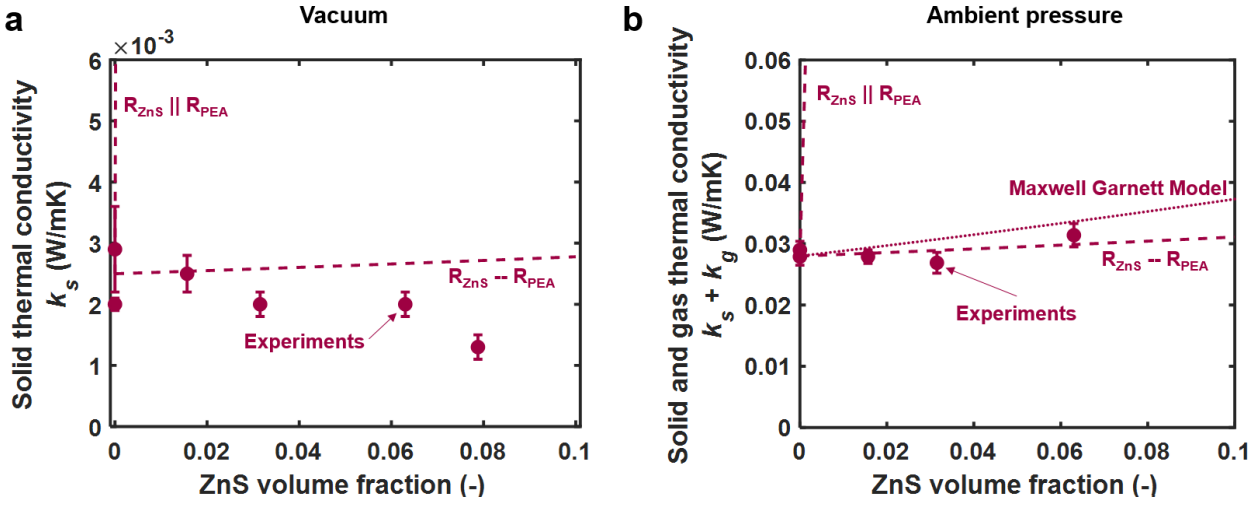

*Figure 34 – **Influence of ZnS volume fraction on PEA thermal conductivity**. (a) Influence of ZnS on the solid (and gaseous) component of thermal conductivity as measured (a) in vacuum and (b) in N_2 at ambient pressure.*

We first explain the impact of ZnS volume fraction on the cover's thermal conductivity by calculating upper and lower bounds. The lower bound or series model assumes that the ZnS nanoparticles are in series with the PEA, while the upper bound or rule of mixture model assumes that the ZnS conducts heat in parallel with the PEA. We observe that in the lower bound case (R_{ZnS} -- R_{PEA}), the ZnS contribution to thermal conductivity is negligible within the volume fraction range considered while for the upper bound case (R_{ZnS} || R_{PEA}), the thermal conductivity quickly increases above 0.005 W/mK at $f_v > 0$. In reality, we should however expect an effective thermal conductivity closer to the lower bound due to the random dispersion of the filler inside the matrix, as well as an additional interfacial thermal resistance between ZnS nanoparticles and the PEA matrix. In fact, spherical particles will not form a continuous network (necessary condition for upper bound estimate) below the percolation volume fraction threshold (f_v = 0.2895 [111]), and will be randomly dispersed, which is what was observed in our work (Figure 31) due to the low ZnS volume fraction (f_v = 0 to 0.044). Furthermore, we should also expect an interfacial thermal resistance between ZnS nanoparticles and the polyethylene backbone due to phonon scattering and imperfect physical contact, an additional resistance not captured in the simple upper and lower bound

models [112], [113]. Together, these factors have been used in prior work to explain why experimental thermal conductivity of composite materials are often orders of magnitude smaller than predicted by the rule of mixture upper bound estimate [113], and can also be used in this work to explain the little difference in the cover thermal conductivity with increasing ZnS volume fraction.

Given the low volume fraction of ZnS in our work, we may also consider another simple model, developed by James Clerk Maxwell [114] as an analogy to electrical conductivity of a material filled with suspended spheres. In our case, the suspended spheres refer to the ZnS nanoparticles while the material refers to the PEA (solid and gaseous components of thermal conductivity only). This model typically holds for low volume fraction (<0.25) with widely separated spheres, making it a good approximation for our medium. We observe that this model predicts a slightly higher thermal conductivity than the lower bound model, but still suggests a very small increase (<10%) in the ZnS volume fraction range studied in previous sections.

Overall, we conclude that ZnS has a negligible influence on thermal conductivity in the range of volume fractions considered, which we explain by the low volume fraction of ZnS, the random dispersion of the nanoparticles within the PEA and the interfacial thermal resistance between the ZnS nanoparticles and the polyethylene and gas.

4.7. SUMMARY

We proposed to improve the optical selectivity of existing PEA OSTI covers by adding solar scattering and infrared transparent ZnS nanoparticles. Using Mie theory to predict the optical properties of ZnS nanoparticles and solving the RTE, we theoretically demonstrated that ZnS addition in PEA could reduce the cover's solar transmittance to well below 0.01 while maintaining high IR transmittance (>0.8). This increased optical selectivity was further demonstrated experimentally using PEA samples pigmented with commercially available ZnS nanoparticles (SACHTOLITH HD-S). We then showed that this increased optical selectivity did not induce an increase in the cover thermal conductivity and that it could drastically improve the subambient cooling performance of radiative coolers, achieving 24.3 W/m² cooling with a blackbody emitter at 5 K below the ambient temperature or more than 53.8 W/m² higher than an unpigmented PEA cover. Furthermore, the added optical selectivity of the cover can reduce the required OSTI cover thickness to achieve subambient cooling using non-selective surfaces. Finally, we demonstrated that using non-uniform ZnS distributions within the PEA cover could reduce the total mass of ZnS required by over 30% while still yielding superior cooling. Overall, our results show the promise of improving the subambient cooling performance of radiative coolers by making it independent from the emitter solar optical properties. We believe this work could improve the performance of existing radiative

coolers and enable new applications such as passive cooling of buildings and passive refrigeration of food produce.

In the next chapter, we investigate an alternative approach to improving the cooling performance of passive coolers, combining our PEA with an evaporating water layer to provide additional cooling power.

Chapter 5

5. Hybrid Cooling Architecture for Simultaneous Evaporative and Radiative Cooling

5.1. INTRODUCTION

The cooling power one can extract from a pure radiative cooler is rather small – around 120 W/m² at ambient temperature. For passive cooling of buildings or of food produce, it implies that a large surface area exposed to the sky is needed to achieve the necessary cooling or that the emitting surface should be at a higher temperature. As a result, existing systems using radiative cooling to improve the efficiency of air conditioners [115] typically rely on the emitting surface to operate above the ambient temperature to meet the air conditioner load. On the other hand, evaporative cooling can provide much higher cooling power per unit area due to the large enthalpy of vaporization of water but suffers from high water consumption and is typically not optimized to minimize solar absorption.

Combining evaporative cooling with radiative cooling could potentially bring major benefits [116], [117]. However, the net cooling power which can be extracted from such a passive cooling architecture has not been experimentally or theoretically characterized, which is critical to evaluate its potential building and food storage applications. In this chapter, we present a unique hybrid evaporative-radiative cooling architecture and then theoretically and experimentally characterize its cooling performance in Cambridge, MA, US (elevation ≈ 22 m). With existing scalable materials, we reached 9.3 °C below the ambient under direct sunlight (solar radiation Q_{sun} = 836 W/m^2) and net ambient cooling power of 143 W/m^2 at RH = 44.0% around solar noon (Q_{sun} = 772 W/m^2) as well as 202 W/m^2 at RH = 70.2% during the nighttime. Finally, we compare the passive cooling performance of our hybrid architecture with that of radiative coolers in all 16 climates regions of the United States, showing large benefits in cooling power.

5.2. HYBRID COOLING ARCHITECTURE

Our hybrid cooling structure consists of a solar reflector, a water-rich and IR-emitting evaporative layer, and a vapor-permeable, IR-transparent, and solar-reflecting insulation layer (Figure 35). The solar reflector minimizes solar absorption by the structure while the water-rich layer achieves passive cooling by both IR emission and evaporation of water. The vapor permeable insulation on top of the water-rich layer can provide additional solar reflectance to minimize parasitic solar heat gain, while also minimizing

parasitic heat gain for the ambient air when operating below the ambient temperature. To simplify notation, we will from now on refer to the cooling designs with and without the top insulation layer as *Hybrid 1* and *Hybrid 0* respectively.

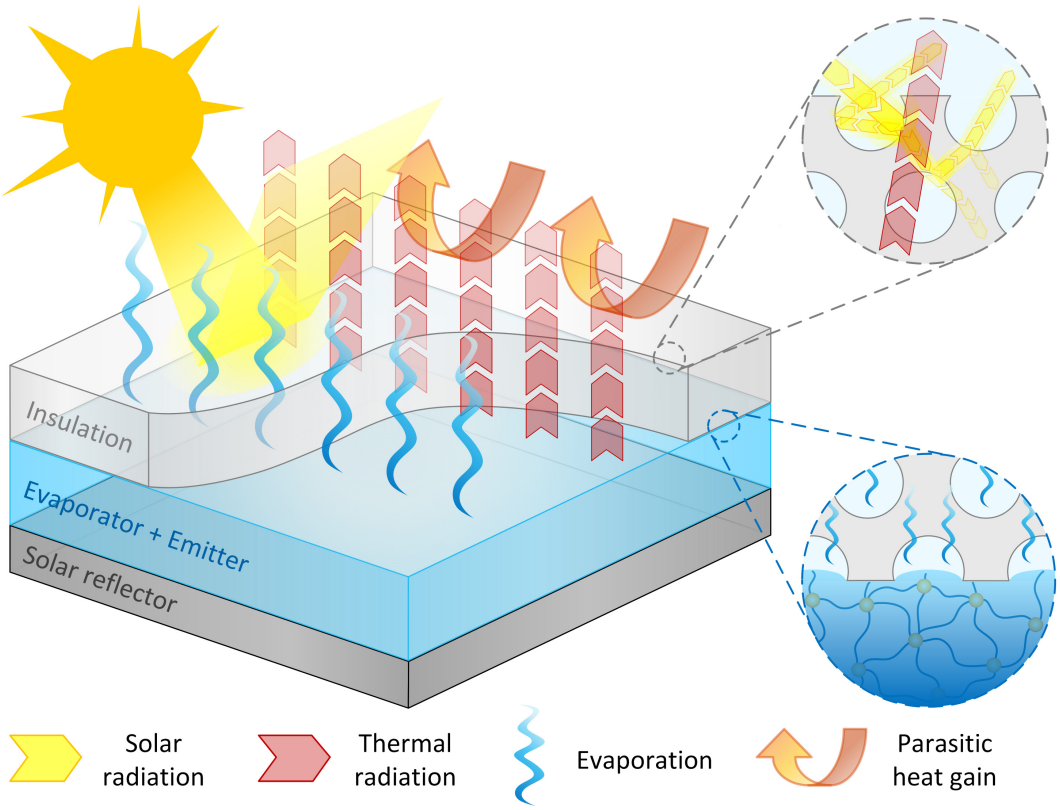

*Figure 35 – **A hybrid evaporative-radiative cooling architecture.** (a) Cooling structure consisting of a solar reflector, a water-rich and IR-emitting evaporative layer, and a vapor-permeable, IR-transparent, and solar-reflecting insulation layer. Figure credit: Lenan Zhang, Massachusetts Institute of Technology.*

5.3. MODELING COOLING PERFORMANCE

We model the cooling performance of our hybrid cooling design using a 1D steady state combined heat and mass transfer energy balance to account for solar/thermal radiation, heat conduction, water vapor diffusion as well as heat and water vapor convection. We define our control volume as the evaporation and insulation layers, of which the bottom boundary is defined by the substrate underneath and the top boundary is defined by the ambient air, the atmosphere and the solar input. Our model solves for the energy balance of the system given by

$$\frac{d}{dx}\left(q_{evap} + q_{rad} + q_{cond}\right) = 0, \tag{26}$$

where x is the distance from the top surface of the insulation layer, $q_{evap,}$ q_{rad}, and q_{cond} are the energy flux associated with evaporation, radiation, and conduction, respectively, and the energy flowing from the ambient to the substrate takes the positive sign.

Similar to previous modeling work for radiative cooling with a PEA cover, we solve for Eq. (26) by first discretizing the control volume into L layers and then taking a linear temperature profile $T(x)$ within the system as an initial guess based on the boundary conditions. We then use the temperature profile within each layer to calculate the divergence of $q_{evap,}$ q_{rad}, and q_{cond} at the interfaces of each of the L layers, and iteratively update $T(x)$ using a nonlinear solver in MATLAB until we satisfy the heat equation. Details of the evaporative, radiative, and conductive energy fluxes are given below. Because of the similarity in the modeling framework, modeling assumptions presented in Section 3.9 also apply here.

5.3.1. Evaporative Energy Flux

The evaporative energy flux q_{evap} is driven by the vapor density difference between ρ_0 at the evaporation/insulation interface and ρ_{amb} in the ambient air. Here, ρ_0 corresponds to the saturation vapor density at the evaporation/insulation interface temperature T_0 and ρ_{amb} is characterized by the ambient temperature T_{amb} and RH. The evaporative flow needs to overcome two transport resistances: the first being the mass diffusion resistance in the insulation layer governed by Fick's law and the second being the mass convection resistance at the air/insulation layer interface. Accounting for both resistances, we obtain the evaporative flux j_{evap}:

$$j_{\mathrm{evap}} = -\frac{\rho_0 - \rho_{\mathrm{amb}}}{\frac{L_{\mathrm{ins}}}{D_{\mathrm{ins}}} + 1/h_{\mathrm{m}}}, \tag{27}$$

where L_{ins} is the insulation thickness, D_{ins} is the diffusion coefficient of water vapor in the insulation layer, h_m is the mass transfer coefficient at the air/insulation layer interface. For PEA, D_{ins} was experimentally determined equal to D_{PEA} = 1.8e-5 m/s² as per the wet cup method following ASTM E96 [92]. A negative sign for j_{evap} implies that the net evaporative flow is from the evaporation/insulation interface to the ambient air. The evaporative energy flux can then be calculated from the evaporative flux:

$$q_{\mathrm{evap}} = j_{\mathrm{evap}} h_{\mathrm{fg}}, \tag{28}$$

where h_{fg} is the enthalpy of vaporization of water at temperature T_0. In our multilayer model, we assume that the evaporative energy flux is constant across the whole insulation layer and that within the insulation, there is no temperature dependent effect, condensation, or re-evaporation.

5.3.2. Radiative Heat Flux

The radiative heat flux q_{rad} is governed by the emission, absorption and scattering that originate from the atmosphere, the insulation layer, the water-rich layer, and the substrate underneath. We solved for q_{rad} at each layer of the same control volume using the radiative transfer equation (RTE).

The optical properties (scattering albedo ω, extinction coefficient β and scattering phase function p) of the water-rich (polyacrylamide hydrogel, introduced in the next section) and the insulation layer (PEA) were estimated from experimental measurements of hemispherical transmittance and reflectance, and direct transmittance. In the current model, the spatial variation of optical properties with changing medium is also accounted for, such that the optical depth $\tau_\lambda = \int_0^x \beta_\lambda ds$, the scattering albedo ω_λ, the scattering phase function p_λ and the spectral blackbody intensity B_λ are all functions of the spatial coordinate x.

The boundary condition at $x = 0$ (air/insulation layer interface) was set by the downward irradiance from the atmosphere modeled in MODTRAN® 6.0 [67] (see Section 2.3.1 on atmospheric modeling) using time and geographical specific weather conditions:

$$I_\lambda(0, -\mu) = I_{\infty,\lambda}(-\mu), \tag{29}$$

where $I_{\infty,\lambda}$ is the spectral diffuse radiance at the top of the medium (*i.e.*, the atmospheric radiance). At the bottom side of the water-rich layer, we assumed reflection and emission from the reflector/emitter at temperature T_{sub}.

$$I_\lambda\left(\tau_{\lambda,\mathrm{tot}}, \mu\right) = \epsilon_\lambda B_\lambda(T_{\mathrm{sub}}) + 2\int_0^1 d\mu'\, \mu'(1-\epsilon_\lambda) I_\lambda\left(\tau_{\lambda,\mathrm{tot}}, -\mu\right) + \frac{F_\lambda^S}{\pi} e^{-\tau_{\lambda,\mathrm{tot}}}(1-\epsilon_\lambda), \tag{30}$$

where ϵ_λ is the emitter spectral emissivity and $\tau_{\lambda,tot}$ is the optical depth at the bottom of the water-rich layer. We note that the IR emission from the water-rich layer is captured as volumetric emission by the RTE and therefore does not appear in the boundary conditions. Because water is strongly absorbing in the IR, we can also expect that the IR properties of the substrate will not be important.

The total radiative heat flux is then calculated by adding the total diffuse and direct fluxes of radiation:

$$q_{\mathrm{rad}}(x) = -\left[2\pi \int_0^\infty \int_1^{-1} I_\lambda(\tau_\lambda(x), \mu)\mu d\mu d\lambda + \int_0^\infty F_\lambda^S e^{-\tau\lambda} d\lambda\right], \tag{31}$$

where the negative sign implies that the net radiation energy flow goes out of the control volume towards the ambient.

5.3.3. Conductive Heat Flux

The conductive heat flux q_{cond} is driven by the local temperature gradient and thermal conductivity in the system and is evaluated at each interface of the L layers of our medium. We solve for q_{cond} using Fourier's law:

$$q_{\text{cond}} = -k\nabla T, \tag{32}$$

where the thermal conductivity k is equal to $k_{\text{h}} = 0.6$ W/mK for PAH and $k_{\text{PEA}} = 0.028$ W/mK for PEA. We note that k_{PEA} refers only to the solid and gas components of thermal conductivity as the radiative component is captured by our radiative model. As part of our boundary conditions, we set a fixed emitter temperature T_{sub} at the bottom of the water-rich layer. At the air/insulation layer interface, we assume thermal convection with the ambient air with a heat transfer coefficient h_{conv}. When modeling our experimental systems, we estimated h_{conv} based on the wind speed in our experiments using the empirical relation $h_{\text{conv}} = 5.7 + 3.8V$ as proposed by Ezekwe [94].

5.3.4. Cooling Power and Stagnation Temperature

Once we find the temperature profile $T(x)$ within our system that satisfies Eq. (26) , we can calculate the evaporative, radiative, and conductive energy flux at any location x such as $x = 0$ to evaluate the total cooling power:

$$q_{\text{cool}} = -\big(q_{\text{evap}}(x=0) + q_{\text{rad}}(x=0) + q_{\text{cond}}(x=0)\big). \tag{33}$$

By changing the substrate temperature (one of the boundary conditions), we can evaluate the cooling power as a function of the temperature difference between the substrate and the ambient. From there, we may evaluate the stagnation temperature difference ΔT defined as $T_{\text{sub}} - T_{\text{amb}}$ when $q_{\text{cool}} = 0$ W/m² and the net ambient cooling power q_0 defined as q_{cool} at $T_{\text{sub}} = T_{\text{amb}}$.

In Figure 36, we use our model to plot $-\Delta T$ and q_0 as a function of the insulation thickness for pure radiative cooling (orange solid line) and hybrid cooling (blue solid line). More specifically, both cooling structures use the same 3M ESR selective emitter and PEA as in Chapter 4, while the hybrid design also uses a 1-mm thick water film as the evaporator. As reference ambient conditions, we used $T_{\text{amb}} = 30$ °C, RH = 50%, $Q_{\text{sun}} = 1000$ W/m^2, a heat transfer coefficient to the ambient air $h_{\text{conv}} = 10$ W/m^{2}K, and the U.S. Standard 1976 atmosphere. First, we observe that the hybrid design exhibits both colder stagnation temperature (Figure 36a) and higher cooling power (Figure 36b) than pure radiative cooling for all insulation thickness considered, demonstrating the potential of the hybrid cooling architecture to provide

better passive cooling under these weather conditions. More significantly, we also show that both systems can reach a temperature below the wet bulb temperature, a limiting temperature for traditional evaporative-only cooling systems. In Figure 36c, we also consider the water mass flux leaving the system $\dot{m}''$ for the two cooling methods. While pure radiative cooling achieves $\dot{m}'' = 0$, the hybrid cooling without insulation (*Hybrid 0*) consumes a large amount of water (blue point at $t_{PEA} = 0$ mm; up to 540 g/m²h of water), corresponding to around 0.54 mm of water per hour for a stagnant water layer. Nevertheless, adding insulation on top of the water-rich layer (*Hybrid 1*) can significantly decrease $\dot{m}''$ for hybrid cooling. By minimizing solar absorption and resisting parasitic heat gain (which becomes even more useful for materials with non-ideal optical properties and for operation at subambient temperature operation [11], [118]), the insulation layer can help decrease water consumption by ~90% at a cover thickness 17 mm. At the same time, the insulation layer also reduces water evaporation by adding a resistance to vapor diffusion, which comes at the expense of a lower total cooling power (76% lower cooling power at a cover thickness of 17 mm). Overall, we therefore observe that the increased water savings are attained by a decrease in the cooling power. Depending on the cooling performance required (high cooling power vs low stagnation temperature) and on the water consumption requirements (low vs high water consumption), the insulation layer can thus be tuned to achieve the desired performance.

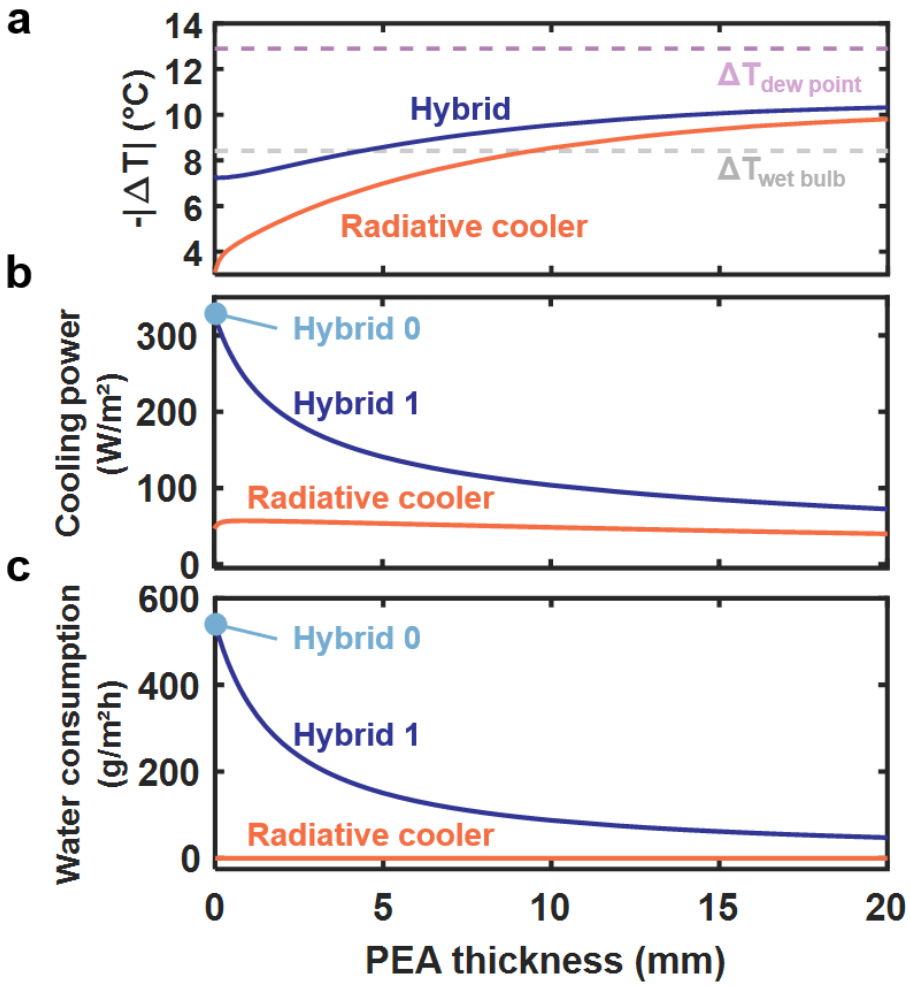

Figure 36 – ***Cooling performance of the hybrid evaporative-radiative architecture.*** *Model of (a) stagnation temperature, (b) cooling power and (c) evaporation mass flux at the ambient temperature for radiative cooling and hybrid cooling with varying insulation thickness. A 3M Enhanced Specular Reflector (ESR) selective emitter, a 1-mm thick water layer and PEA were used. We used T_{amb} = 30 °C, RH = 46%, Q_{sun} = 1000 W/m^2, h_{conv} = 10 W/m^{2}K and the U.S. Standard 1976 atmosphere as the ambient condition. Hybrid cooling at zero insulation thickness is denoted as Hybrid 0 (light blue point).*

5.4. EXPERIMENTAL DEMONSTRATION

5.4.1. Proof-of-Concept Hybrid Architecture

Experimentally, we realized the hybrid cooling concept with existing scalable materials: a 3M Enhanced Specular Reflector (ESR) film, a polyacrylamide hydrogel (PAH), and a polyethylene aerogel (PEA), used as the three layers in Figure 35, from bottom to top respectively. The images of PAH and PEA are shown in Figure 37: PAH is transparent in the visible spectrum and opaque in the IR while the opposite holds for PEA, making them ideal materials for our hybrid cooling concept.

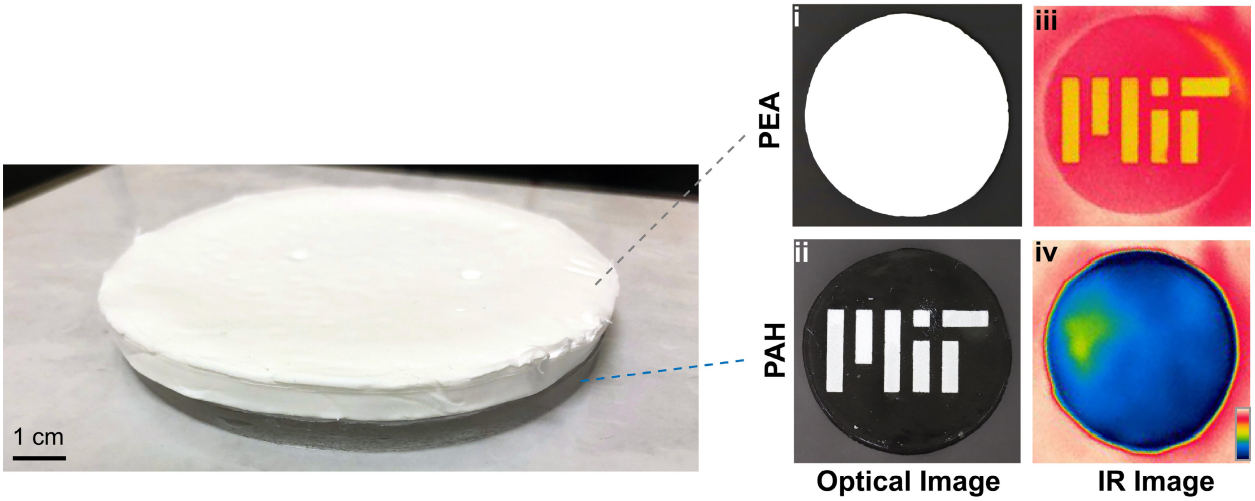

*Figure 37 – **Experimental hybrid cooling architecture**. (a) Optical and IR images of polyacrylamide hydrogel (PAH) and polyethylene aerogel (PEA). The height of the MIT logo is 40 mm. Figure credit: Zhengmao Lu, Massachusetts Institute of Technology.*

Detailed optical properties of PAH can be found in Figure 38 where we observe high transmittance and low absorption in the solar spectrum (α_{solar} = 0.15) , with very high emission in the infrared ($\varepsilon_{8\text{-}13\ \mu m}$ = 0.98) for a 7-mm thick PAH sample. To fabricate the PAH samples, we mixed 4.3 g acrylamide (A8887, Sigma Aldrich) and 20 mL deionized (DI) water to form the monomer solution for PAH synthesis. 320 µL 0.4 wt.% solution of N,N'-Methylenebisacrylamide (146072, Sigma Aldrich) in DI water was used as the crosslinker. 320 µL 5 wt.% solution of ammonium persulfate (A3678, Sigma Aldrich) was used as the reaction initiator. 40 µL N,N,N′,N′-Tetramethylethylenediamine (T9281, Sigma Aldrich) was used as the reaction accelerator. We added the crosslinker solution, the initiator solution, and the accelerator solution to the monomer solution and quickly put the mixture into a mold. We placed the mold in an UV oven (Spectrolinker™ UV Crosslinker, Spectronics) for an hour to obtain PAH which was then put into excess DI water to reach the fully hydrated state. The PAH fabrication was done by Zhengmao Lu.

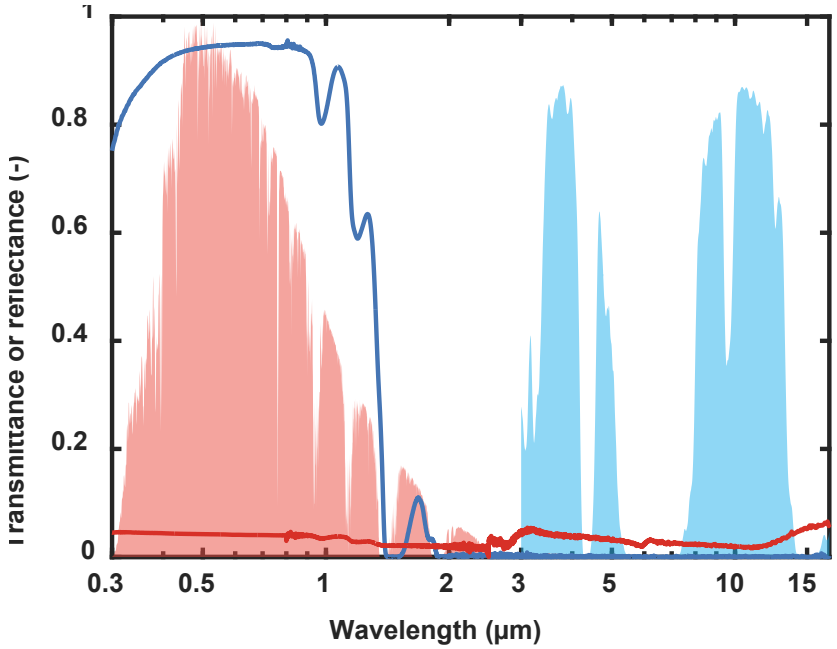

*Figure 38 – **PAH optical properties.** Hemispherical spectral transmittance (red line) and reflectance (purple line) of a 7 mm thick PAH sample. For reference, the normalized solar irradiance spectrum (red area) and the atmospheric transmittance (blue area) are also plotted.*

5.4.2. Stagnation Temperature Test

For our experimental demonstration of the hybrid cooling concept, we first focus on the stagnation temperature test for the two cases of hybrid cooling with and without insulation (*Hybrid 1* and *Hybrid 0*), where significant temperature drop is demonstrated under direct sunlight. In Figure 39, two identical experimental setups were placed next to each other on the roof of a building in Cambridge, Massachusetts, USA: one contained a 3M ESR film, a PAH layer, and a PEA layer (Hybrid 1) while the other had a 3M ESR film and a PAH layer without the PEA insulation (Hybrid 0). The diameter of the samples is 10 cm. To simulate 1-D heat and mass transfer in our experiments, the samples were insulated using a 5 cm thick vacuum insulation panel (VIP) (THRESHOLD, Thermal Vision) with 2.88 mW/m-K thermal conductivity on the bottom as well as a 10-mm thick aerogel insulation blanket (08-052gel, HiwowSport) with 12-18 mW/m-K thermal conductivity surrounding the perimeter. The aerogel blanket was covered by an aluminum sheet to reduce solar heating of the setup. Between the PAH and the vacuum insulation is a 3M ESR reflective film which serves as a reflector. A T-type thermocouple was embedded between the VIP and the reflector to measure the temperature with a data acquisition card (NI-9212, National Instruments) and a mass balance was used to record the mass change. The weather conditions including the ambient temperature, dew point, solar radiation, and wind speed were recorded by a weather station (HOBO U30 Station).

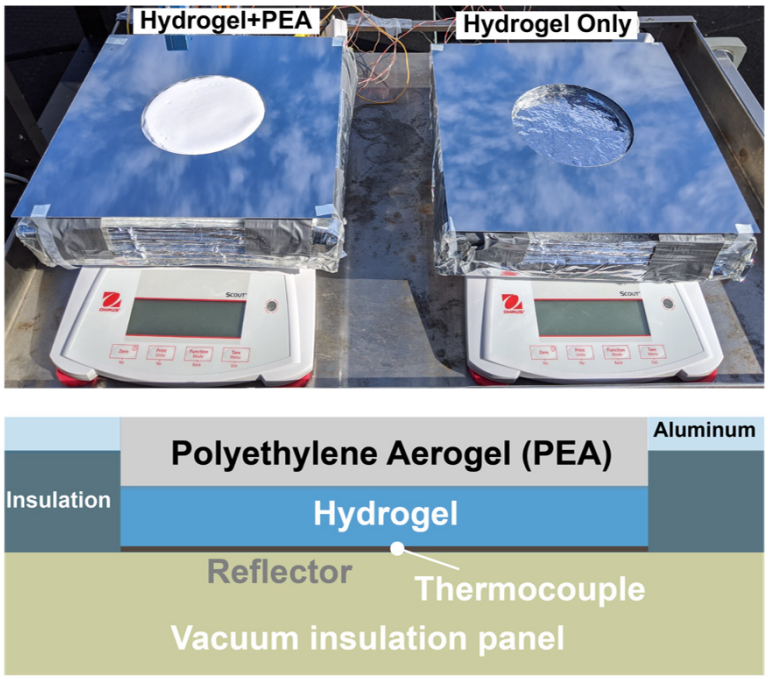

*Figure 39 – **Stagnation temperature setup**. Image (top) and schematic (bottom) of experimental setup: two identical setups were placed next to each other, where left one contains a 3M ESR film, a PAH layer, and a PEA layer (Hybrid 1) and the right one also has the ESR and PAH layers but without the PEA layer (Hybrid 0). The diameter of the samples is 10 cm. Experiments were performed on the roof of an MIT building (Cambridge, MA, USA). Photo credit: Arny Leroy, Massachusetts Institute of Technology. Figure credit: Zhengmao Lu, Massachusetts Institute of Technology.*

We report the temperature of the *Hybrid 0* sample (light blue solid line) and the Hybrid 1 sample (dark blue solid line), as well as the ambient (black solid line), the dew point (light pink solid line) and the wet bulb temperature (light gray solid line) recorded between 10:00 and 22:00 on August 26, 2020 (Figure 40a). The other weather conditions including the solar radiation and the wind speed during this period can are also shown in Figure 40c. The thickness of the PAH and PEA layers are summarized in Table 3.

Table 5 – PAH and PEA thickness for the stagnation temperature tests in Figure 40.

	Thickness (mm)	
System	**PAH**	**PEA**
Hybrid 1: ESR+PAH+PEA	7.4	7.6
Hybrid 0: ESR+PAH	7.1	-

Leveraging simultaneous net radiation and vapor outflow, we achieved temperatures significantly below the ambient for both samples and even below the wet bulb temperature. In the daytime, the temperature of the *Hybrid 1* sample was 2-3 °C lower than the *Hybrid 0* sample as the PAH still absorbs a non-negligible amount of solar energy without protection from the solar-reflecting PEA layer. At night when $Q_{sun} = 0$, this temperature difference becomes minimal. We also plot the evaporated water mass as a function of

time for the two samples (Figure 40b). Adding the PEA caused evaporation of the Hybrid 1 sample to be significantly slower, which is typically associated with higher sample temperatures [11]. However, since PEA resists parasitic and solar heating, the *Hybrid 1* sample reached lower stagnation temperatures even with much less water consumption. With the *Hybrid 1* sample, we demonstrated a stagnation temperature drop of 9.3 °C for T_{amb} = 22.2 °C and RH = 39.5% under solar radiation Q_{sun} = 836 W/m². Overall, the stagnation temperature measured demonstrated the ability of the hybrid concept to achieve all-day subambient temperatures while also showing the benefits of the insulation cover to reduce water consumption.

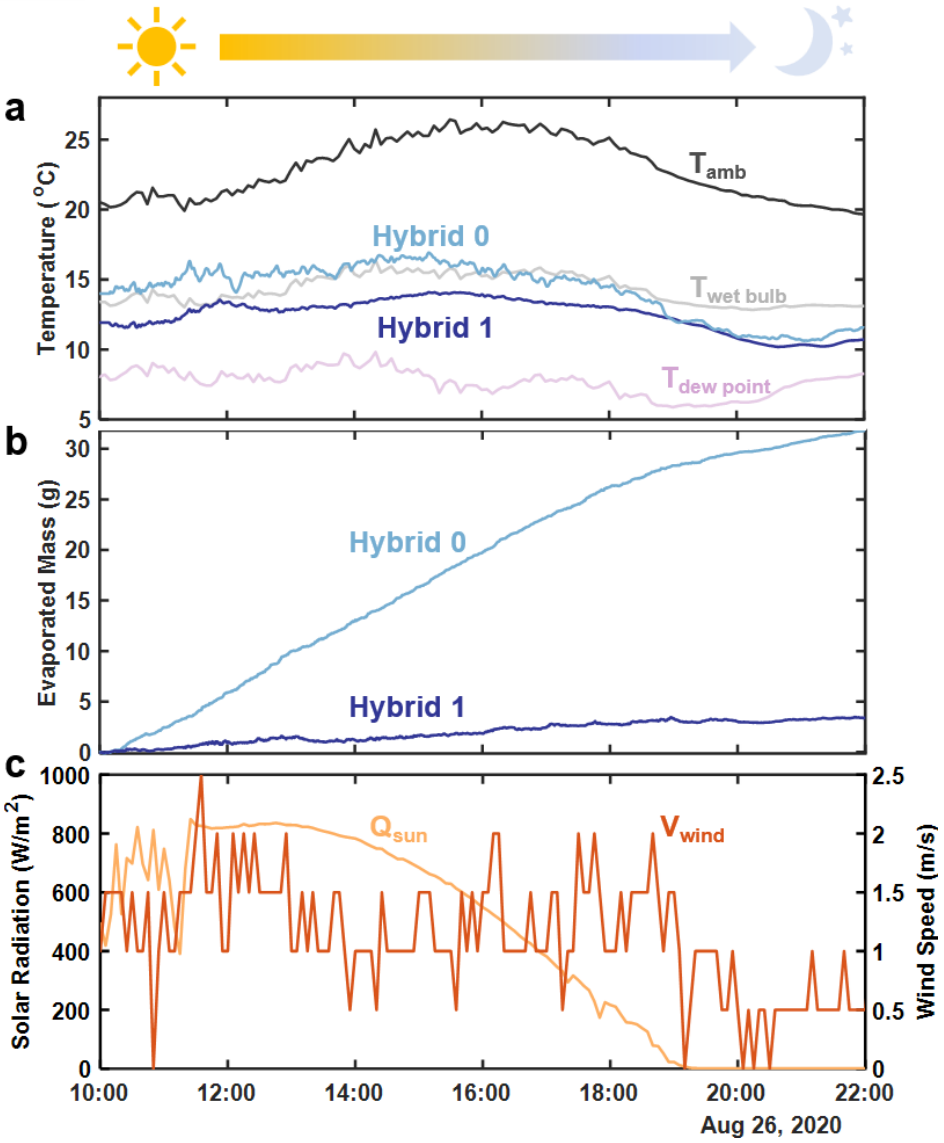

*Figure 40 – **Stagnation temperature experimental results**. (a) Stagnation temperature profile and (b) evaporated water mass for the Hybrid 0 sample (dark blue line) and the Hybrid 1 sample (light blue line) recorded between 10:00 and 22:00 on August 26, 2020. The ambient dry bulb temperature (dark gray), the wet bulb temperature (light gray) and the dew point (light pink) are also shown in (a). (c) The solar irradiance and wind speed during the experiment.*

To compare the experimental results with model predictions, we averaged the data for both setups during the daytime (11:30-13:00) and the nighttime (20:00-21:00), separately, generating four different cases (Figure 41). Good agreement is shown between the model and experiments for all cases in terms of both -ΔT and $\dot{m}''$. The uncertainty on the substrate temperature and temperature difference between the substrate and ambient was determined from the calibrated thermocouple uncertainty (±0.2 °C), the weather station uncertainty (±0.2 °C), as well as from the standard deviation of their fluctuation during the measuring period. The uncertainty on the water mass loss rate was calculated from the standard deviation of the slope of water mass vs time in our stagnation temperature experiments as well as from the scale uncertainty (± 0.1 g). While the error that results directly from temperature and mass measurement is low, the error bars in Figure 41 are mainly due to the standard deviation of the fluctuation during the averaging period. Error bar on the modeling were not included but would include the uncertainty on the input weather conditions, the layer thicknesses and the optical properties of each layer. We also note that two-dimensional heat and mass transfer near the circumference of the PAH and PEA samples can alter the cooling performance of the devices.

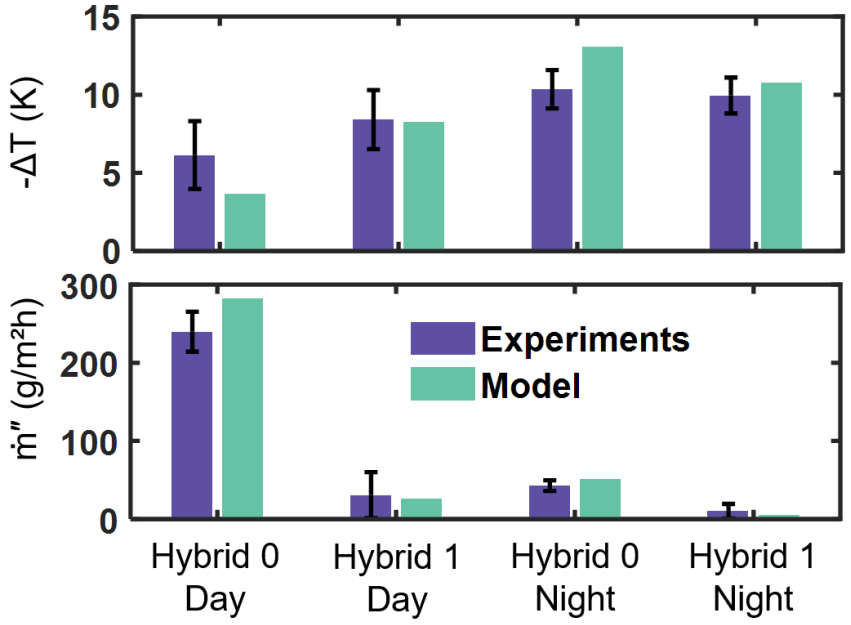

*Figure 41 – **Model comparison**. Comparison of -ΔT (top) and evaporation mass flux $\dot{m}''$ (bottom) for four different cases between experimental (dark green) and modeling (light green) results.*

5.4.3. Cooling Power Test

Next, we show that hybrid cooling enables large subambient cooling power even under unfavorable climate conditions. At a low altitude test location (Cambridge, MA; elevation ≈ 22 m), we characterized the net cooling power of *Hybrid 0*, *Hybrid 1*, and a reference pure radiative cooler (ESR + PEA) while

varying $\delta T = T_{sub} - T_{amb}$ by embedding heaters and temperature controllers underneath the cooling layers. To achieve this experimental demonstration, we used the same experimental setup and methods described earlier in Section 3.5. A schematic and pictures of the outdoor experimental setup with the PAH and PEA are shown in Figure 42. We used similar materials for each cooling design to allow for fair comparison.

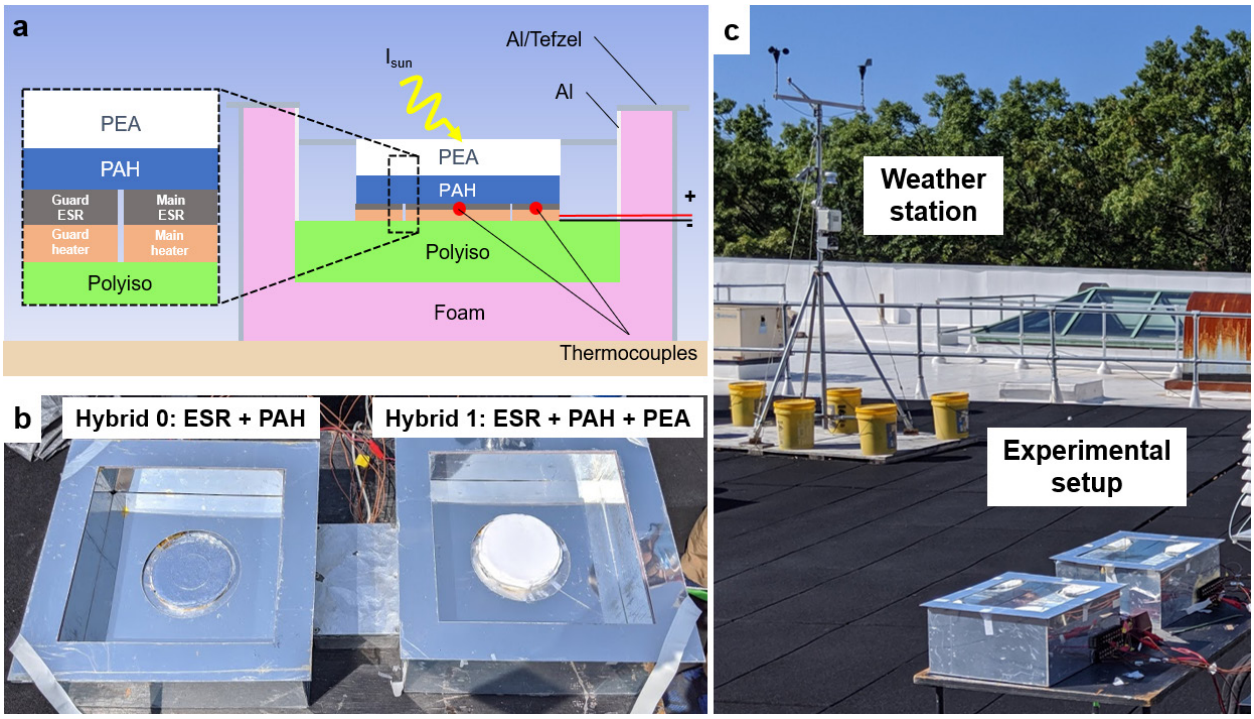

*Figure 42 – **Cooling power experimental setup.** (a) Schematic of experimental setup. A PAH+PEA cooling stack is placed on top of the 3M ESR. The ESR and heater are split into two parts: 1) the main ESR and the main heater which are located in the center of the disc and used for 1D heat transfer temperature and power measurements; 2) the guard ESR and the guard heater which are used to minimize the lateral heat transfer for the main heater and the main emitter. (b) Photo of outdoor experimental setup with two identical setups – the Hybrid 0 sample with ESR + PAH only (left) and the Hybrid 1 sample with the ESR+PAH+PEA (right). The diameter of the samples is 10 mm. (c) Picture of the outdoor experimental setup (cooler power setup) next to the weather station (HOBO U30 Station). The weather station measures temperature, dew point, relative humidity, solar global horizontal irradiance, average wind speed, gust wind speed and wind direction at intervals of 5 min. Photo Credit: Arny Leroy, Massachusetts Institute of Technology.*

The first set of experiments compared the performance of *Hybrid 1* (ESR + PAH + PEA) against pure radiative cooling (ESR + PEA)[118] (Figure 43a-b) while the second set compared *Hybrid 1* (ESR + PAH + PEA) and *Hybrid 0* (ESR + PAH) (Figure 43c-d). Each set of tests contains both a daytime and a nighttime comparison to evaluate the influence of solar absorption on the cooling power. The PAH and PEA thickness used in each experiment are detailed in Table 4 below.

Table 6 – PAH and PEA thicknesses for the cooling power experiments in Figure 43.

	System	Thickness (mm)	
		PAH	PEA
Daytime	ESR+PAH+PEA	5.0	6.0
	ESR+PEA	-	5.4
Nighttime	ESR+PAH+PEA	5.0	6.0
	ESR+PEA	-	5.4
Daytime	ESR+PAH+PEA	5.0	7.5
	ESR+PAH	5.0	-
Nighttime	ESR+PAH+PEA	5.0	7.5
	ESR+PAH	3.0	-

In Figure 43a, we show significantly higher cooling power of *Hybrid 1* (dark blue circles for experimental data and dark blue solid line for model prediction) compared to pure radiative cooling (*ESR + PEA*; orange circles for experimental data and orange solid line for model prediction). Specifically, around $\delta T = 0$ K, we obtained $q_{cool} = 22$ W/m² for pure radiative cooling and $q_{cool} = 86$ W/m^2 for *Hybrid 1* with RH = 50.9%, which represents an almost 300% increase. The *Hybrid 1* device also enables much higher cooling power at subambient temperatures and a lower stagnation temperature. In Figure 43b, the cooling power difference between *Hybrid 1* and pure radiative cooling becomes less at night as evaporation was much slower with the lower T_{amb} and higher RH. In Figure 43c-d, we compare the performance of two hybrid devices to study the influence of PEA insulation on the cooling performance. In Figure 43c around the ambient temperature with RH = 44.0%, *Hybrid 1* reached $q_{cool} = 96$ W/m^2 which is lower than the 143 W/m^2 from the *Hybrid 0* (dark blue circles for experimental data and dark blue solid line for model prediction) device. This is due to the minimal parasitic heat gain when T_{sub} is close to T_{amb}. At night (Figure 43d), the high solar reflectance of PEA also becomes irrelevant, leading to even better relative performance of *Hybrid 0* which reached a cooling power of 202 W/m^2 versus 105 W/m^2 for the *Hybrid 1* device at an RH = 70.2%. On the other hand, Figure 43[c-d] also shows that the low thermal conductivity of PEA can still help the system maintain a higher q_{cool} when T_{sub} is sufficiently below the ambient. As such, we observe a crossover point in the cooler power vs temperature drop curve, which locates the point at which the *Hybrid 1* devices enables higher cooling power than the *Hybrid 0* (or vice versa). Overall, the results show that the hybrid architecture can provide larger cooling power than traditional radiative cooling systems, and that PEA insulation can help achieve higher cooling power at lower temperatures.

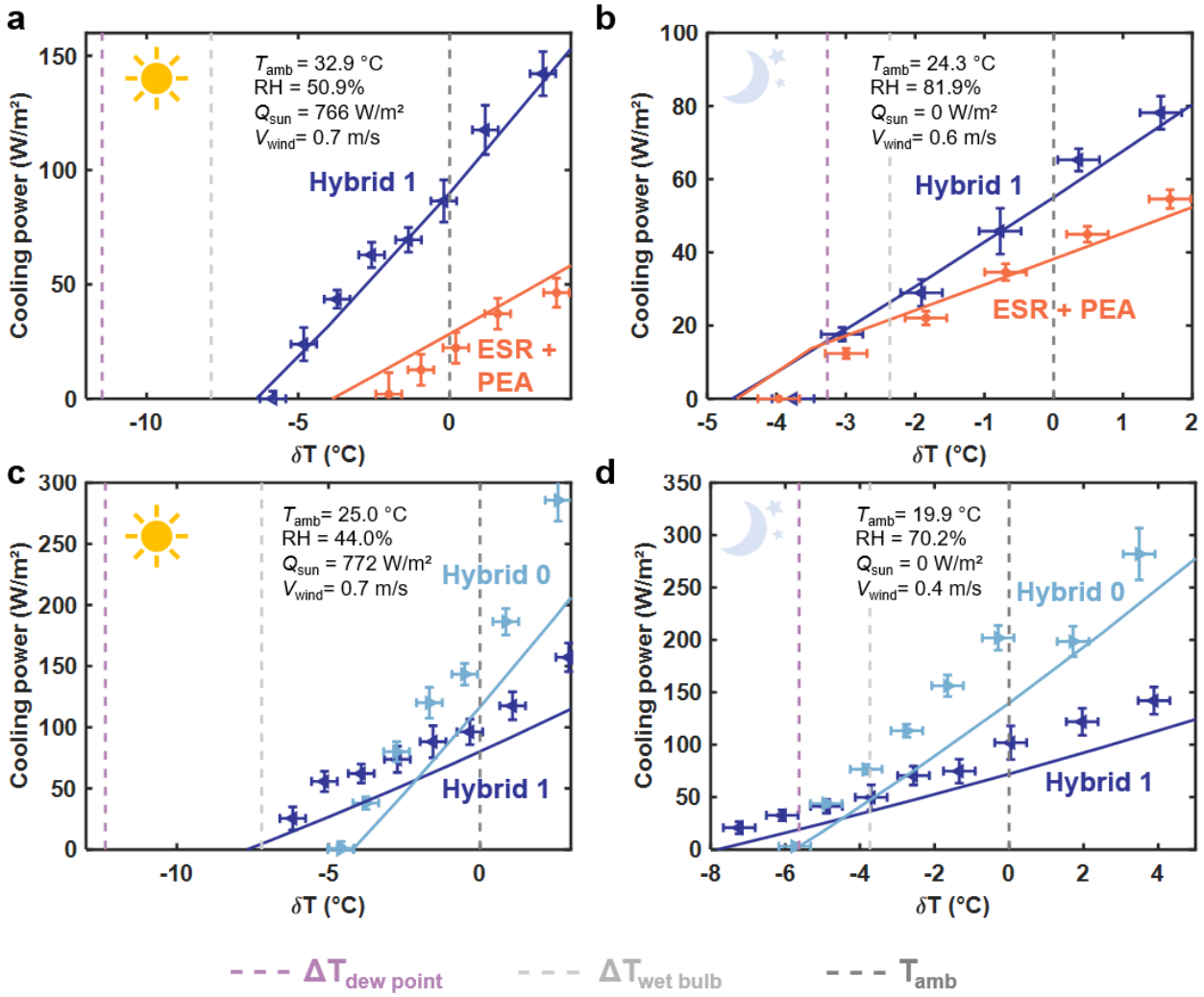

Figure 43 – ***Cooling power test.*** *High cooling powers were demonstrated with our hybrid evaporative-radiative architecture with high RH and at low altitude. We compare model and experiments of cooling power as a function of the temperature difference between the substrate and the ambient ($\delta T = T_{sub} - T_{amb}$) for (a) Hybrid 1 sample (with insulation) vs the pure radiative sample in the daytime and (b) at night and (c) Hybrid 1 sample vs Hybrid 0 sample (without insulation) in the daytime and (d) at night. The weather conditions are also provided for each set of experiments. The PAH and PEA thickness for each experiment and system are given in Table 4.*

We further consider the case where the solar reflectance of the reflector is not high enough to provide passive cooling such that a PEA layer also becomes essential for mitigating solar heating. For example, in Figure 44, we replaced the ESR substrate with a white paint (ColorMaster™ Paint + Primer White) surface with 0.77 solar reflectance (Figure 44a). In Figure 44b, we show that the *Hybrid 1* (white paint + PAH + PEA) design shows consistently better cooling performance for subambient-to-ambient temperatures than the *Hybrid 0* design due to the additional solar reflectance provided by PEA. With the PEA layer, the performance of the hybrid cooling layers is much less sensitive to the optical properties of

the substrate and can thus achieve larger temperature drop. In Figure 43[a-d] and Figure 44b, we again show good agreement between the experimental data and the model prediction.

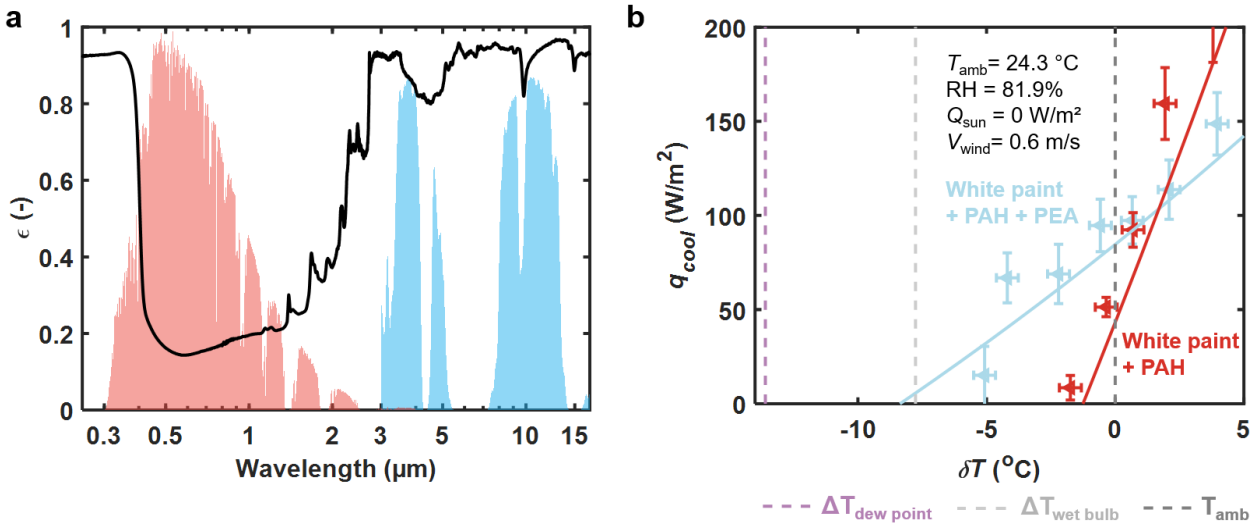

Figure 44 – ***Cooling power test with low performance reflector substrate underneath the cooling stack.*** *(a) Spectral emittance of a low performance white paint (ColorMaster™ Paint + Primer White) coated substrate (black line) along with the normalized solar irradiance spectrum (red area) and the atmospheric transmittance (blue area). While the white paint emitter shows a high IR emittance of 0.93, its solar reflectance of 0.77 is too low to allow any daytime subambient radiative cooling when placed under direct sunlight by itself. (b) Comparison between the modeled and experimental cooling power as a function of the temperature difference between the substrate and the ambient ($\delta T = T_{sub} - T_{amb}$) for a White Paint + PAH + PEA vs a White Paint + PAH sample in the daytime. The PEA sample was 7.6 mm thick while the PAH layers were 6 mm thick. The test was performed around solar noon in Cambridge, MA on August 26, 2020.*

5.5. PREDICTING COOLING PERFORMANCE ACROSS THE UNITED STATES

Using our experimentally validated model, we can further evaluate the cooling performance of the hybrid cooling architecture across the United States to guide future passive cooling systems design. To do so, we consider a list of cities that represents all 16 different climate zones in the US (see Table 5). In each city, we evaluate the stagnation temperature ΔT, the ambient cooling power q_0 and the water consumption $\dot{m}''$ of the *Hybrid 0* cooler (ESR + PAH), the *Hybrid 1* cooler (ESR + PAH + PEA), the reference radiative cooler (ESR + PEA), and an ideal radiative cooler. For the stagnation temperature, the ideal radiative cooler consists in an ideal selective emitter (perfect reflectivity except in the 8-13 μm range where it has an emissivity of 1) covered with a 5-mm thick PEA to minimize parasitic heat gain. For the ambient cooling power, the ideal radiative cooler is chosen as an ideal stepwise emitter (perfect reflectivity below 2.5 μm and an emissivity of 1 above 2.5 μm) with no PEA to maximize heat rejection. The local weather data at noon on August 1 was used in our model and was obtained from the *Typical Meteorological Year 3* (TMY3) hourly weather data, which represent the typical weather conditions derived from

measurements between 1991 and 2005 [119]. A summary of the weather conditions is presented in Figure 45. Finally, we assume 1-mm thick PAH, 5-mm thick PEA for the hybrid coolers and the non-ideal radiative cooler.

Table 7 – Building America (BA) and International Energy Conservation (IECC) climate zones for a list of US cities.

City	BA Climate Zone	IECC Climate Zone
Miami	Hot-Humid	1A
Houston	Hot-Humid	2A
Phoenix	Hot-Dry	2B
Atlanta	Mixed-Humid	3A
Las Vegas	Hot-Dry	3B
Los Angeles	Hot-Dry	3B-Coast
San Francisco	Marine	3C
Baltimore	Mixed-Humid	4A
Albuquerque	Mixed-Dry	4B
Seattle	Marine	4C
Chicago	Cold	5A
Boulder	Cold	5B
Minneapolis	Cold	6A
Helena	Cold	6B
Duluth	Very Cold	7A
Fairbanks	Subarctic	8

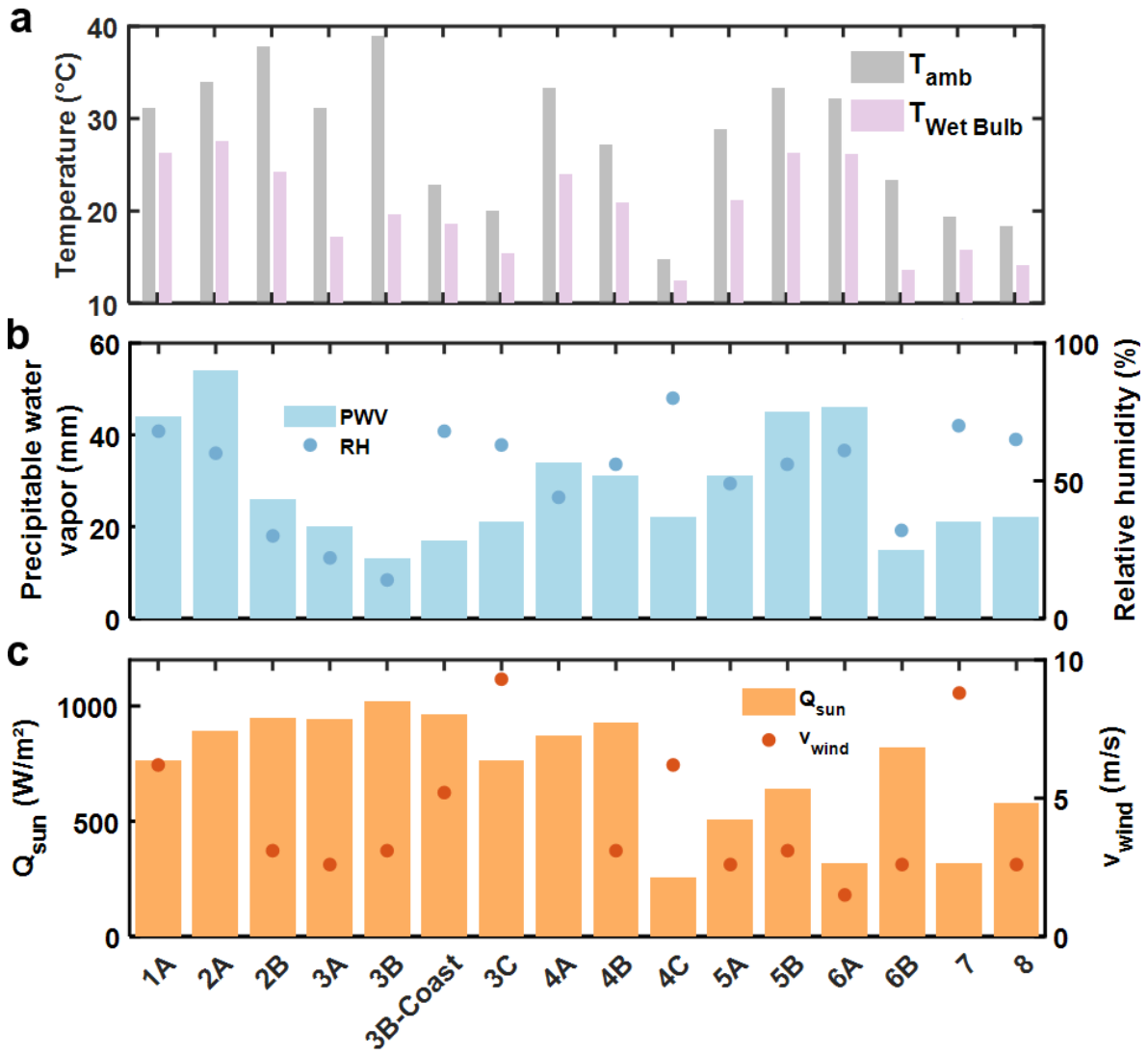

*Figure 45 – **TMY3 weather conditions**. (a) Ambient dry bulb and wet bulb temperatures, (b) precipitable water vapor and relative humidity, and (c) solar irradiance and wind speed in all 16 climates zones at noon on August 1, as given by the TMY3 weather conditions.*

A comparison of the cooling performance of each system is depicted in Figure 46. Starting with the stagnation temperature (Figure 46a), we observe that the *Hybrid 0* (light blue bars) and the *Hybrid 1* (dark blue bars) exhibit the largest temperature drop in hot and dry climates such as 2B, 3A and 3B, often reaching a lower temperature than the wet bulb temperature. In colder climate conditions such as 3B-Coast, 3C, 4C, 6B, 7 and 8, we however observe that the *Ideal radiative cooler* (yellow bars) can provide lower stagnation temperature than the hybrid devices, demonstrating the importance of weather conditions on the efficacy of the evaporative cooling. Yet, when compared to a more realistic *Radiative cooler* (orange bars), the hybrid devices achieve in general, equal, or colder stagnation temperatures. In terms of cooling power (Figure 46b), the *Hybrid 0* exhibits by far the highest cooling power while also consuming the largest amount of water in all cases (Figure 46c). *Hybrid 1* significantly cuts the water

usage while still offering cooling powers higher than even the *Ideal radiative cooler* for almost all climate zones, again highlighting the compromise between water consumption and cooling performance. The radiative-only cooling devices have no water consumption, which represents an advantage for these systems over the hybrid designs. Overall, we have demonstrated that the hybrid cooling architecture could provide colder stagnation temperature and higher cooling power than the pure radiative systems. We however saw that the benefits in cooling performance were more important in hot and dry climates, and that better performance was possible with an ideal radiative cooler in colder climates.

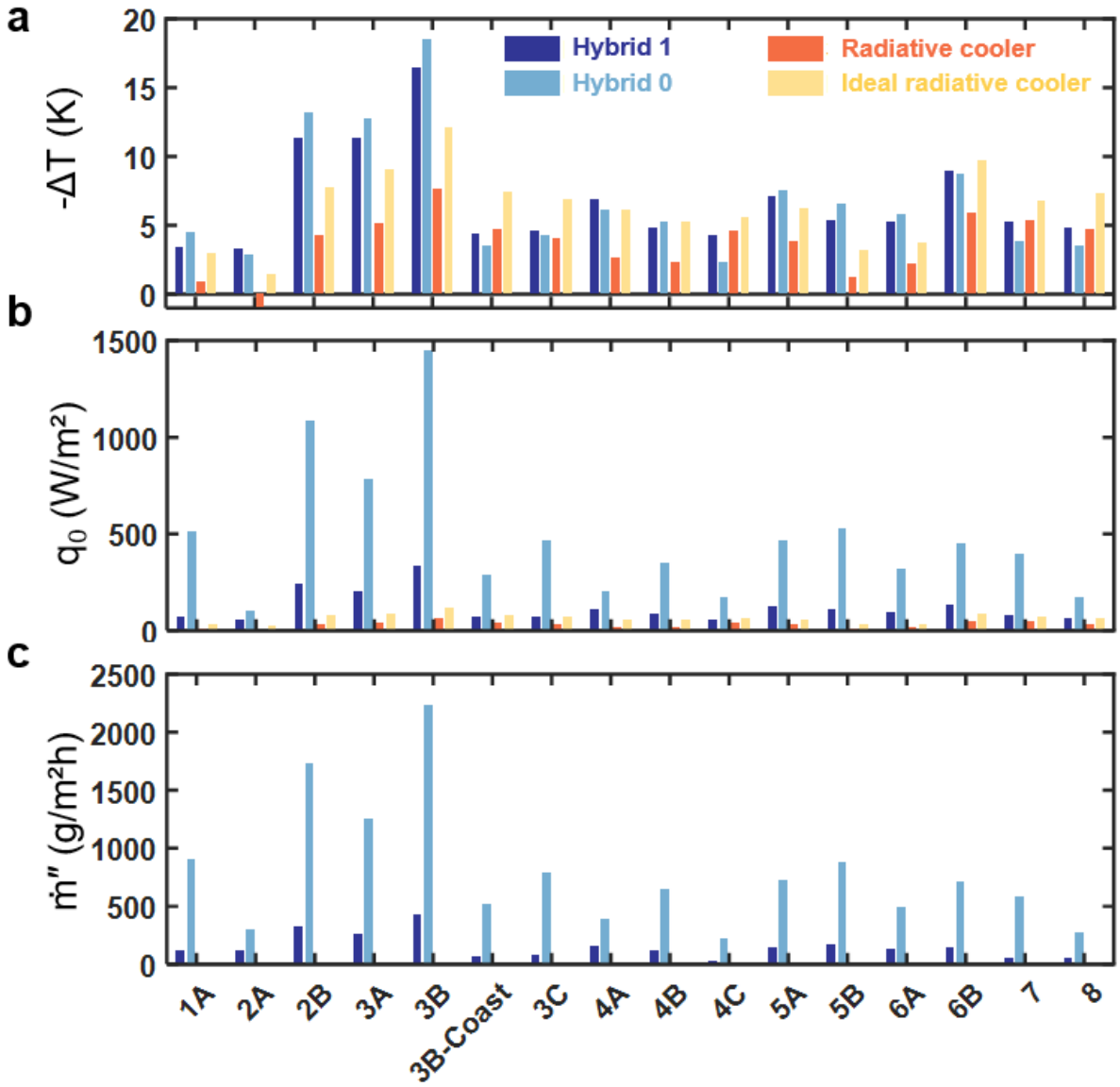

Figure 46 – ***Cooling performance in different cities/climate zones.*** *(a) Stagnation temperature, (b) ambient cooling power, and (c) water consumption at different locations calculated for the Hybrid 1 cooler (dark blue bar), and the Hybrid 0 cooler (light blue bar), and the reference pure radiative cooler (orange bar), as well as an ideal broad-band radiative cooler* [120] *(yellow bar) based on the typical weather data TMY3 at noon on August 1.*

5.6. SUMMARY

In this chapter, we proposed to address the low cooling performance of standalone radiative and evaporative coolers by combining the two approaches in a single hybrid architecture. With the help of modeling, we first showed the potential of this hybrid architecture using existing materials and standard weather conditions. Motivated by these results, we then fabricated the hybrid cooling stack using a 3M ESR reflector, a water-rich and IR emitting polyacrylamide hydrogel layer and a PEA insulation layer and tested the hybrid structures in outdoor experiments in Cambridge, MA. We demonstrated significantly higher cooling power compared to previous radiative cooling works even under much less favorable ambient conditions, while also achieving significant subambient cooling. Unlike previous evaporative coolers which are often heated to above-ambient temperatures by the sun, our hybrid coolers were also able to reach significant subambient temperatures under direct sunlight. Finally, we compared the performance of the hybrid cooling architecture to that of ideal and existing radiative cooler in all 16 climates zones in the United States on a typical summer day. Our results again showed the superior cooling performance of the hybrid cooling structure, but also found that ideal radiative coolers could achieve lower stagnation temperatures in colder climate. The results also highlighted the compromise between the two hybrid cooling approaches, *Hybrid 1* and *Hybrid 0*, where the PEA insulation thickness can be used to decrease water consumption but at the cost of lower cooling power. The high cooling performance of the hybrid structures, combined with low water consumption, could have important implications in building energy savings and food produce storage. In the next chapter, we will propose and evaluate the potential of integrating hybrid cooling with passive food coolers and with air-conditioning and refrigeration systems in buildings across the United States.

Chapter 6

6. Applications for Passive Evaporative and Radiative Cooling

6.1. INTRODUCTION

In the previous chapter, we proposed a new passive hybrid cooling architecture that could achieve higher cooling power and lower stagnation temperatures in hot and dry climates compared to existing standalone radiative or evaporative cooling systems. The results were promising, especially compared to existing radiative cooling systems, but the real-life impact of the improved cooling was not clear.

In this chapter, we study the potential impact of our passive hybrid cooling structure on the storage of food produce, and on the air-conditioning and refrigeration energy use in buildings across the United States. For the storage of food produce, we propose a passive cold storage unit for post-harvest food produce that incorporates our hybrid cooling structure and then briefly evaluate to potential increase in the green life of bananas. For building air-conditioning and refrigeration, we propose a passive cooling panel that can be installed on the rooftop of buildings that can help reduce the vapor-compression cycle condenser-side temperature. Using building level simulations to simulate the cooling demand and using hourly weather data, we then predict the potential energy savings enabled by our passive hybrid cooling panels. Overall, we show that our hybrid cooling architecture can help prolong the lifetime of bananas by over 50% in most cities across the United States and provide cooling energy savings on par with existing evaporative condensers but with significantly less water consumption.

6.2. STORAGE OF FOOD PRODUCE

Around one third of the food produced on earth is being wasted [5]. In developing countries, over 15% of post-harvest food is being lost because of inadequate handling and storage, accentuating food insecurity, reducing farmer's income and depleting natural resources while causing unnecessary greenhouse gases emissions. With earth's increasing population and related consumption, demand on agriculture, energy and natural resources is hitting record highs and must urgently be addressed. Solving this complex problem will require many different types of solutions, ranging from improved food production, environmental performance and resilience, to better data and decision support tools that guide management decisions, to simple solutions improving the food supply chains and customer behavior [4].

One approach to improving the food chain is to improve the cold chain starting right at the post-harvest. Several works in the literature propose ideal storage temperatures and humidity conditions for various food produce as well as their temperature dependent lifetime [6]–[9]. In fact, the storage temperature for sensitive products such as perishable foods can have a drastic effect on produce lifetime. Labuza and Breene [8] summarized the effect of temperature on the shelf life of many vegetables and fruits, where they noted that the rate of quality decay can increase by 2-3× for every 10 °C in temperature increase. Their results suggest that even a small decrease in average or maximum temperature can have significant effects on post-harvest losses. With that in mind, the MIT D-Lab has recently been exploring the use of clay pot passive evaporative coolers to reduce post-harvest food waste in sub-Saharan Africa [15], [121]. By storing post-harvest fruit and vegetables inside clay pots coolers, the authors have demonstrated a decrease in the average daily temperature by 1-3 °C, with a 7-15 °C lower peak daily temperature and a reduction in temperature fluctuations by 10-20 °C. As a result, the controlled environment enabled shelf-life improvements of specific vegetables ranging from 2-4× compared to other vegetables stored at ambient temperature. While the evaporative cooler provides significant benefits to the users, the system still suffers from critical challenges. First, the evaporative cooler suffers from environmental heat gain as its temperature drop below the ambient dry bulb temperature. Second, the evaporative cooler requires frequent watering due to the large evaporation rate of water. Last, the evaporative coolers have poor solar reflectivity, leading to undesired solar heating or requiring the construction of a large shade cover [21]. To tackle these limitations, we propose to use our hybrid cooling architecture to provide passive cooling of food produce at low subambient temperatures, with lower water consumption and without shade cover.

A very simple concept of a hybrid passive cooler for food produce is presented in Figure 47a. A clay container is used to store fruit and vegetables. A lid made of a solar reflector, a water layer and a polyethylene cover provide both radiative and evaporative cooling. The water also wicks into the clay container to evaporate on the side walls. This concept is very similar to evaporative coolers presented in past work [15], [121]. Using our model of the hybrid cooling structure and the same set of materials used in Chapter 5, we estimate the green life (GL) of bananas following Jedermann et al. [9] based on the stagnation temperature that can be achieved by each passive cooling technology. The green life of bananas is compared in Figure 47b for the different cooling devices under the same weather conditions as presented in Figure 45. On average the hybrid cooling devices can extend the green life of bananas by around 50% and even more than 100% in a few cities such as Chicago, Boulder and Phoenix. While the results are only presented for bananas, other perishable produces typical exhibit a similar behavior, experiencing a 2-3× decrease in lifetime for every 10 °C increase in temperature [8]. The fabrication and implementation of a hybrid cooler for food produce could have a significant impact in developing

countries which currently lack proper refrigerated storage facilities. We hope that future work will further investigate this promising avenue, use cheap and locally available materials as well as innovate the design to maximize food storage time.

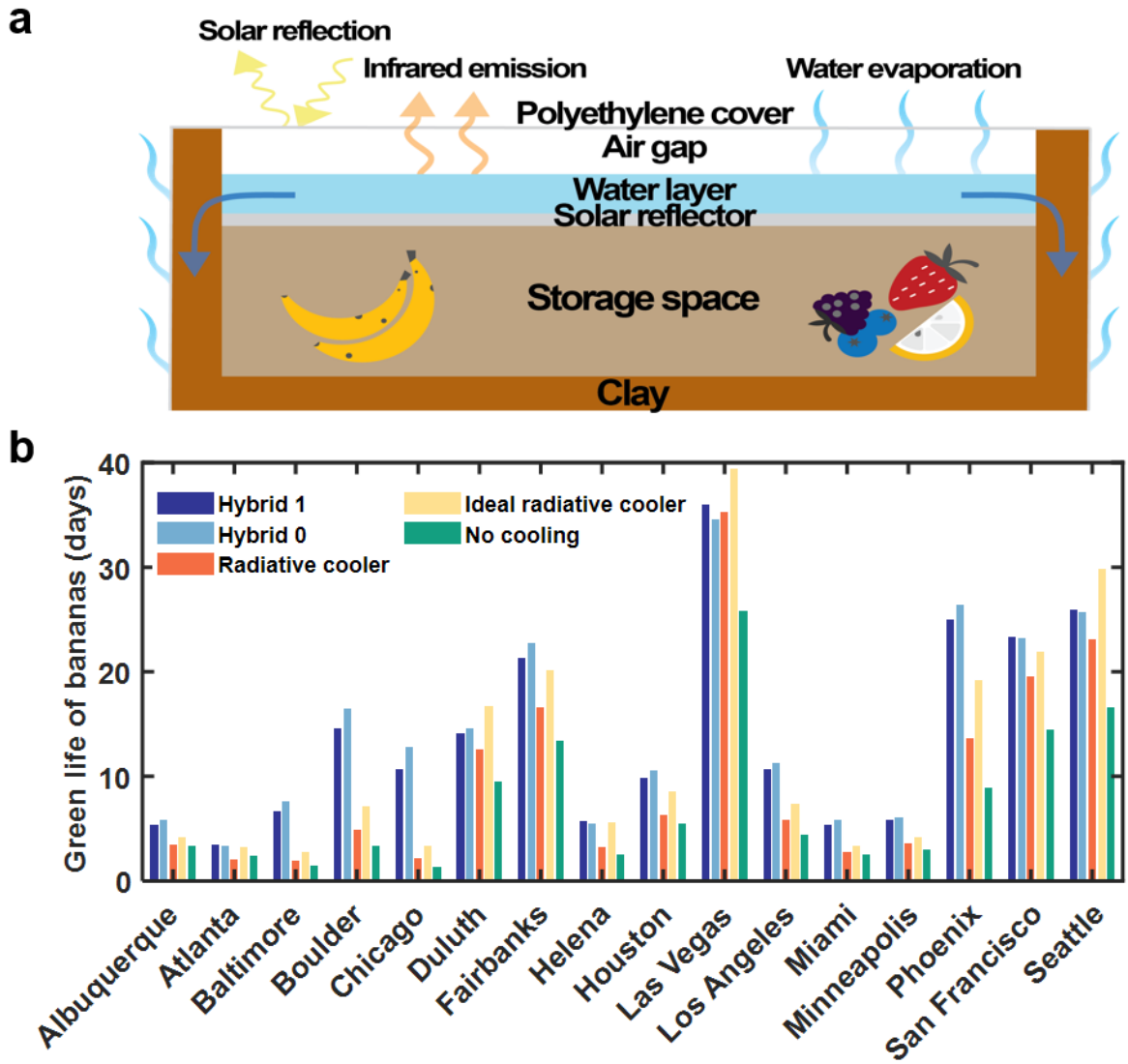

*Figure 47 – **Improving food storage**. (a) Concept of a hybrid evaporative-radiative cooler for storage of food produce. (b) Impact of cooling on the green life of bananas under the weather conditions summarized in Figure 45.*

6.3. REDUCING AIR CONDITIONING AND REFRIGERATION ENERGY IN BUILDINGS

Space cooling was responsible for over 1 Gt CO_2 emissions and 8.5% of the world's electricity consumption in 2019 and represents the fastest-growing end-use of energy in the building sector. Cooling efficiency improvement is urgently needed to reduce this growing electricity demand and the peak load on power supply systems.

Recently, research groups [24], [95] have proposed to use rooftop radiative cooling panels at the condenser side of vapor-compression air conditioning and refrigeration systems to improve the energy efficiency of such systems. Following their initial publications, SkyCool Systems [115] and Radi-Cool [122] have emerged to explore commercialization of radiative cooling panels in commercial buildings. Their initial building level demonstration in grocery stores have led to annual energy savings up to 15% [123]. Yet, because of the relatively low cooling power of radiative cooling, the panels must be operated above the ambient temperature to maximize the total cooling power and the energy savings per cooling panel area, which limits the potential energy savings of the system.

In this section, we propose to use rooftop hybrid cooling panels to improve the energy efficiency of vapor-compression air conditioners and refrigerators. By combining evaporative and radiative cooling, the hybrid cooling panels have the potential to provide higher energy savings with a lower footprint than existing pure radiative cooling panels, while also consuming less water than existing evaporative condensers. A concept of the rooftop hybrid cooling panels is presented in Figure 48. In Figure 48a, we show details of the hybrid cooling structure (from top to bottom: an insulation layer, a water-rich layer, a solar reflector, and a heat transfer fluid), as well as a sketch of a cooling panel and the integration of an array of cooling panels on the rooftop of a commercial building. In Figure 48b, we also depict how the hybrid cooling panel would be connected to existing air-cooled condensers – a heat transfer fluid flows at the backside of the hybrid cooling panels to then enter a heat exchanger where it serves as a cold heat sink to the refrigerant exiting the existing air-cooled condenser.

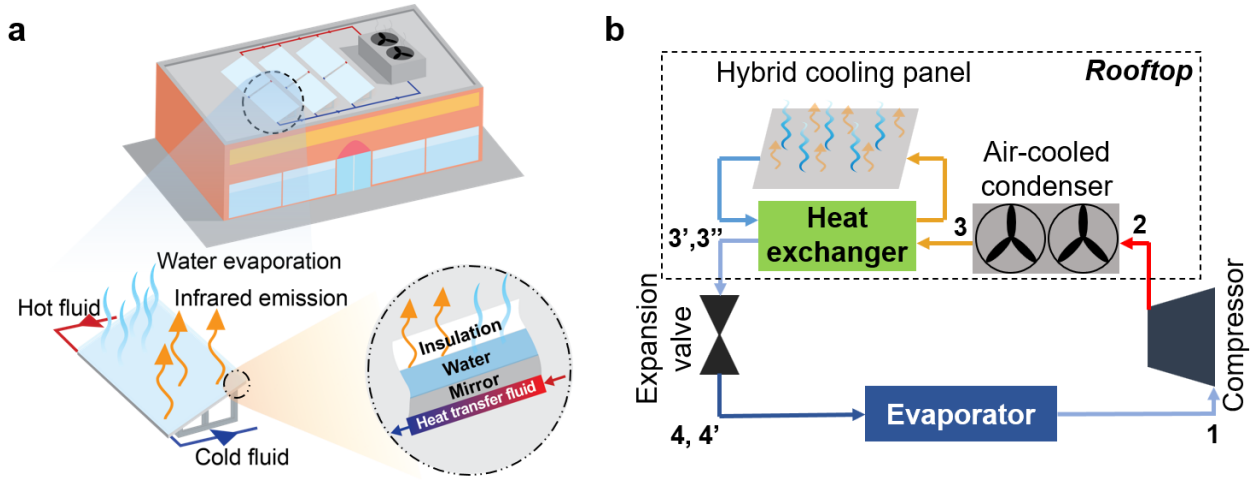

*Figure 48 – **Hybrid cooling panels for air conditioners**. (a) Hybrid evaporative-radiative cooling panels are located on the rooftop of buildings and connected in series with existing air-cooled condensers. A heat transfer fluid flows at the back of the panel, cooling down as it rejects its heat to the panel.*

The advantage of using the hybrid cooling panels at the condenser side can be better understood by looking at the pressure-enthalpy diagram of a refrigeration cycle (Figure 49). In one case, the hybrid cooling panels can lower the condensation temperature of the refrigerant (from 2-3 to 2'-3'), thus reducing the maximum refrigerant pressure and the compressor work. In another case, the hybrid cooling panels can provide refrigerant subcooling (3' to 3''), delivering additional cooling (4'-4) at the evaporator side for a constant compressor work. In the first approach, the air-cooled condenser is only used to provide desuperheating of the refrigerant, while in the second approach the air-cooled condenser is used for the whole condensation heat rejection. Depending on the heat rejection capacity of the panels at a given temperature relative to the ambient, one approach will provide higher energy savings than an another. More specifically, refrigerant subcooling will be more appropriate for lower cooling panel heat rejection capacity while the reduced condensation temperature will provide higher energy savings for higher cooling panel heat rejection capacity.

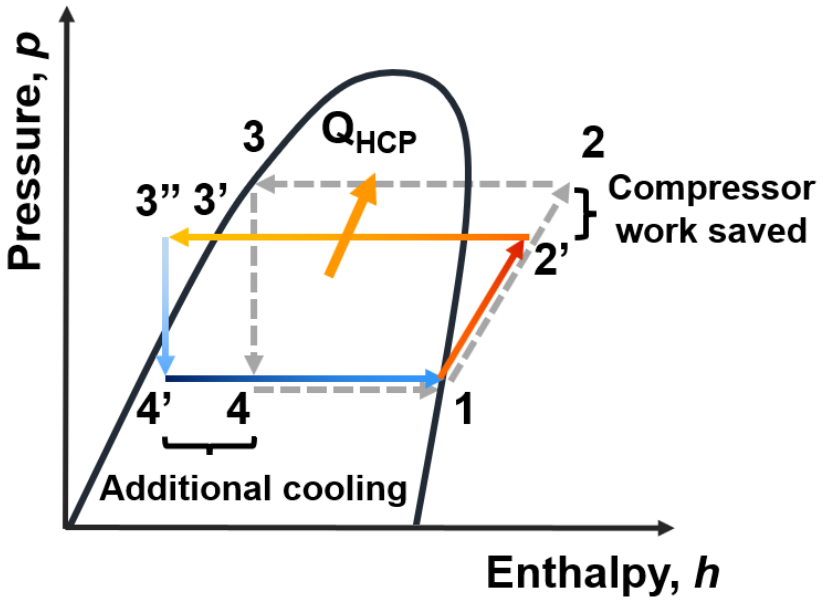

*Figure 49 – **Refrigeration cycle**. Pressure-enthalpy diagram of a refrigeration cycle, characterized by the compression (1-2), the heat rejection to the ambient or condensation (2-3), the expansion (3-4) and the cooling or evaporation (4-1) of a refrigerant.*

Next, we study the potential energy savings in supermarket refrigeration systems using hybrid evaporative-evaporative cooling panels. Supermarkets have a very stable and high refrigeration load (and energy bill) throughout the year, which makes them ideal buildings to improve refrigeration efficiency. In fact, refrigeration energy costs in supermarkets across the United States account for ~$7.7 billion/year, which is just slightly below their total margins of $10.5 billion/year [124]. Even small savings in refrigeration energy use could significantly help increase supermarkets margins and competitiveness.

6.3.1. Modeling Building Cooling Energy Savings

To estimate the potential energy savings of the passive hybrid evaporative-radiative cooling approach proposed here, we start by modeling the hourly cooling load of a typical new supermarket building using *EnergyPlus* (version 9.4). Reference buildings such as the modeled supermarket are provided by the Department of Energy Commercial Reference Buildings [125]. The hourly cooling loads were calculated for 16 representative climates cities (Miami, Florida; Houston, Texas; Phoenix, Arizona; Atlanta, Georgia; Los Angeles, California; Las Vegas, Nevada; San Francisco, California; Baltimore, Maryland; Albuquerque, New Mexico; Seattle, Washington; Chicago, Illinois; Boulder, Colorado; Minneapolis, Minnesota; Helena, Montana; Duluth, Minnesota; Fairbanks, Alaska) representing the 16 climate zones (1, 2A, 2B, 3A, 3B-Coast, 3B, 3C, 4A, 4B, 5A, 5B, 6A, 6B, 7, and 8 respectively) in the United States as defined by the Department of Energy Building America Program [126].

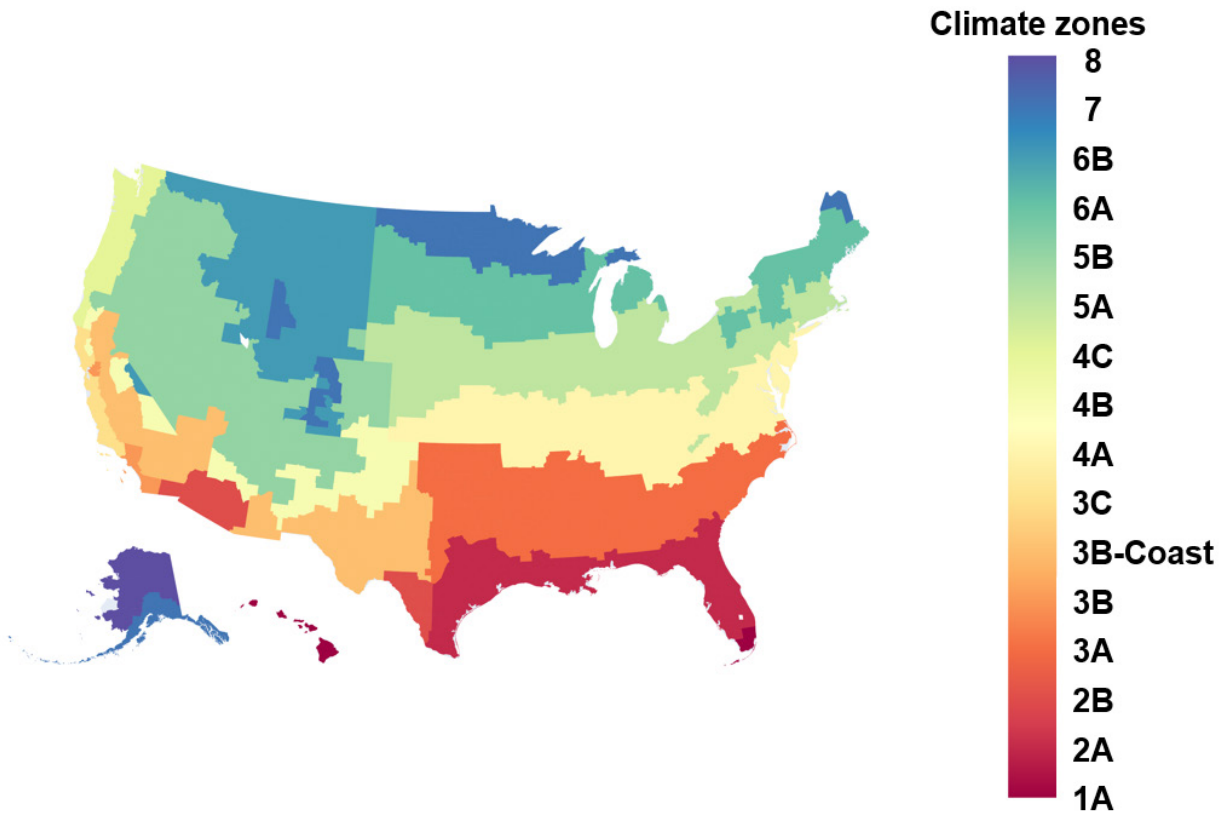

*Figure 50 – **U.S. climate zones**. The geographical location of the 16 U.S. climate zones based on the Department of Energy Building America Program* [126].

The *Typical Meteorological Year 3* (TMY3) hourly weather data, which represents the typical weather conditions derived from measurements between 1991 and 2005, were used for each city [119]. The calculated hourly building cooling loads were then exported to MATLAB to estimate the potential energy

savings of the hybrid cooling architecture. An example of a supermarket hourly refrigeration cooling load calculated in *EnergyPlus* is presented in Figure 51.

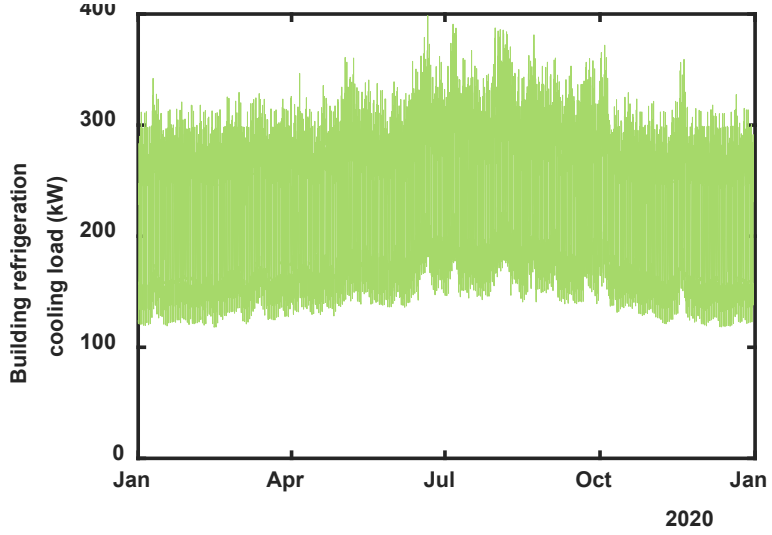

Figure 51 – ***Hourly supermarket refrigeration cooling load****. Hourly supermarket refrigeration cooling load as modeled in EnergyPlus for a 4181 m² supermarket in Las Vegas.*

In MATLAB, we first calculate the baseline system (no evaporative-radiative cooling) hourly electricity consumption. We assume that the refrigeration cycle uses R-407A refrigerant [127] with a fixed evaporator temperature of -2 °C, a compressor isentropic efficiency of 70%, a pressure drop of 1% across the condenser and evaporator, and an air-cooled condenser operating at a temperature of 10 K above the ambient temperature [128] with a power consumption of 20 $W_{electric}$ per 1000 $W_{thermal}$ rejected to the ambient [129], [130]. The thermodynamic properties of the refrigerant are obtained from *CoolProp* [131]. The total energy consumption for the baseline system, calculated on an hourly basis, accounts for the compressor work and the air-cooled condenser fan power. For our hybrid evaporative-radiative cooling approach, we use the same solar reflector, hydrogel, and PEA as in Figure 46 and varied the proportion of the rooftop area covered by our panels depending on the simulation. We also assume that a 15% ethylene glycol-water solution flows at the backside of the cooling panels in a parallel flow configuration. The hybrid cooling panels' fluid loop is also connected to a heat exchanger with the R-407A refrigerant in series (after) with the air-cooled condenser. Depending on the operating mode, the air-cooled condenser either desuperheats (fully or partly down to a temperature of 10 K above the ambient) the refrigerant after compression (while the hybrid cooling panels perform the rest of the refrigerant cooling) or cool the refrigerant down to a saturated liquid state (before subcooling the refrigerant with the hybrid cooling panel). For simplicity, it is assumed that the heat exchanger between the cooling panel heat transfer fluid and the refrigerant operates in a counterflow configuration with an effectiveness of unity.

Using the hybrid cooling panels minimizes the air-cooled condenser fan power while enabling lower condenser temperatures than the baseline system and thus lower compressor work. These energy savings are however counterbalanced by the pumping energy required to flow the ethylene glycol-water fluid at the backside of the hybrid cooling panels such that an optimal mass flow rate must be solved for at each hour. More specifically, a higher fluid mass flow rate will maximize the average temperature of the hybrid cooling panels and thus their total heat rejection rate but will also require a higher pumping power, and vice versa. In our model, we therefore optimize the total energy consumption (sum of compressor work, air-cooled condenser fan work and fluid loop pumping work) by varying the condenser temperature and the fluid loop mass flow rate at each hour. The average hourly cooling power of the hybrid cooling panels is calculated from the hourly TMY3 weather data (ambient temperature, solar irradiance, relative humidity, precipitable water vapor, polyethylene aerogel insulation thickness, wind speed and cloud coverage) and using the average ethylene glycol-water fluid temperature. The yearly energy consumption is summed from the hourly results and energy savings are derived using the baseline system as the reference.

We also use this modeling framework to evaluate the yearly energy and water consumption of traditional evaporative condensers. More specifically, we assume that the evaporative condensers can provide a condensation temperature between 5 °F - 15 °F [132], [133] above the wet-bulb temperature and that they operate with a bleed rate of one-quarter the evaporation rate [128] (we assume an equivalent bleed rate for our hybrid cooling panels).

6.3.2. Results

In Figure 52, we compare the yearly energy savings enabled by the hybrid cooling panels (*Hybrid 0* and *Hybrid 1*) over traditional air-cooled condensers for a standard 4181 m² supermarket across all 16 climates zones in the United States. In Figure 52a, we find that yearly electricity savings of up to 155-160 MWh/building or 27-33% are possible with the *Hybrid 0* system in hot and dry regions such as Phoenix (2B) and Las Vegas (3B) respectively. In Las Vegas, the hybrid cooling panels help increase the COP = 4.2 of the reference system using air-cooled condensers to a COP = 6.3. When we compare the yearly electricity savings enabled by the hybrid cooling panels in these regions to the electricity that photovoltaic panels could generate over the same surface area, we find that the former are 10-14% higher. In other climate zones, this trend however reverses (30-62% lower energy savings vs photovoltaics depending on the region) and make hybrid cooling less competitive on an energy standpoint.

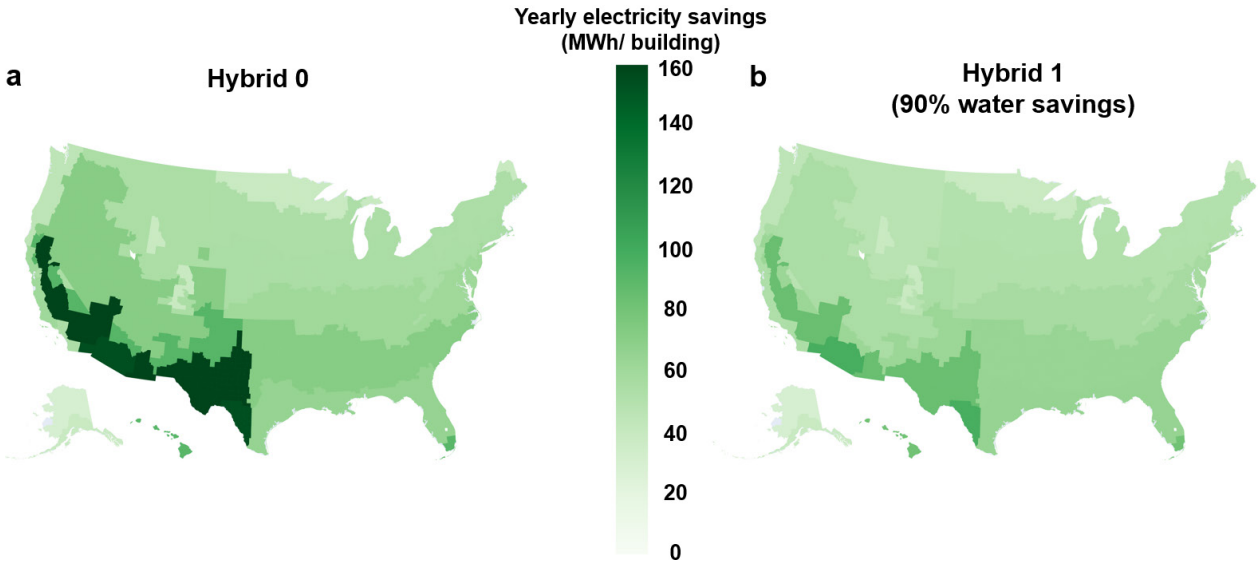

*Figure 52 – **Building-level energy savings.** Yearly refrigeration electricity savings for a standard 4181 m² supermarket by applying the hybrid cooling architecture across the United States calculated based on local climate zones. A 10% rooftop coverage is assumed for the hybrid cooling panels. Traditional air-cooled condensers are taken as a reference.*

In Figure 53, we compare the yearly water consumption of the hybrid panels to that of evaporative condensers. A 76% to 95% reduction in water consumption is observed across the different climate zones for the hybrid cooling panels, a promising number for reducing space cooling related water usage, especially in water-scarce regions. We attribute this reduction in water consumption to a few factors. First, the hybrid nature of the cooling architecture means that a large portion of the cooling is done by radiative cooling, which does not consume water. Second, the cooling panels are in series with an air-cooled condenser which contributes to a portion of the heat rejection. Last, the hybrid cooling panels sometimes operate above the ambient temperature (although at a lower temperature than the air-cooled condenser) and can thus benefit from natural or forced convective cooling. In Figure 52b, we optimized the polyethylene aerogel insulation thickness to reduce water consumption by >90% over traditional evaporative condensers and evaluated the yearly electricity savings at these conditions. This constraint on water consumption lowers the total electricity savings, yet still provides a maximum of 97-84 MWh/building or 17-17.4% in Phoenix (2B) and Las Vegas (3B) respectively and highlights the compromise between water consumption and energy savings. Overall, we have shown that important refrigeration-related electricity savings are possible in supermarkets across the United States using rooftop hybrid cooling panels, while also using much less water than evaporative condensers.

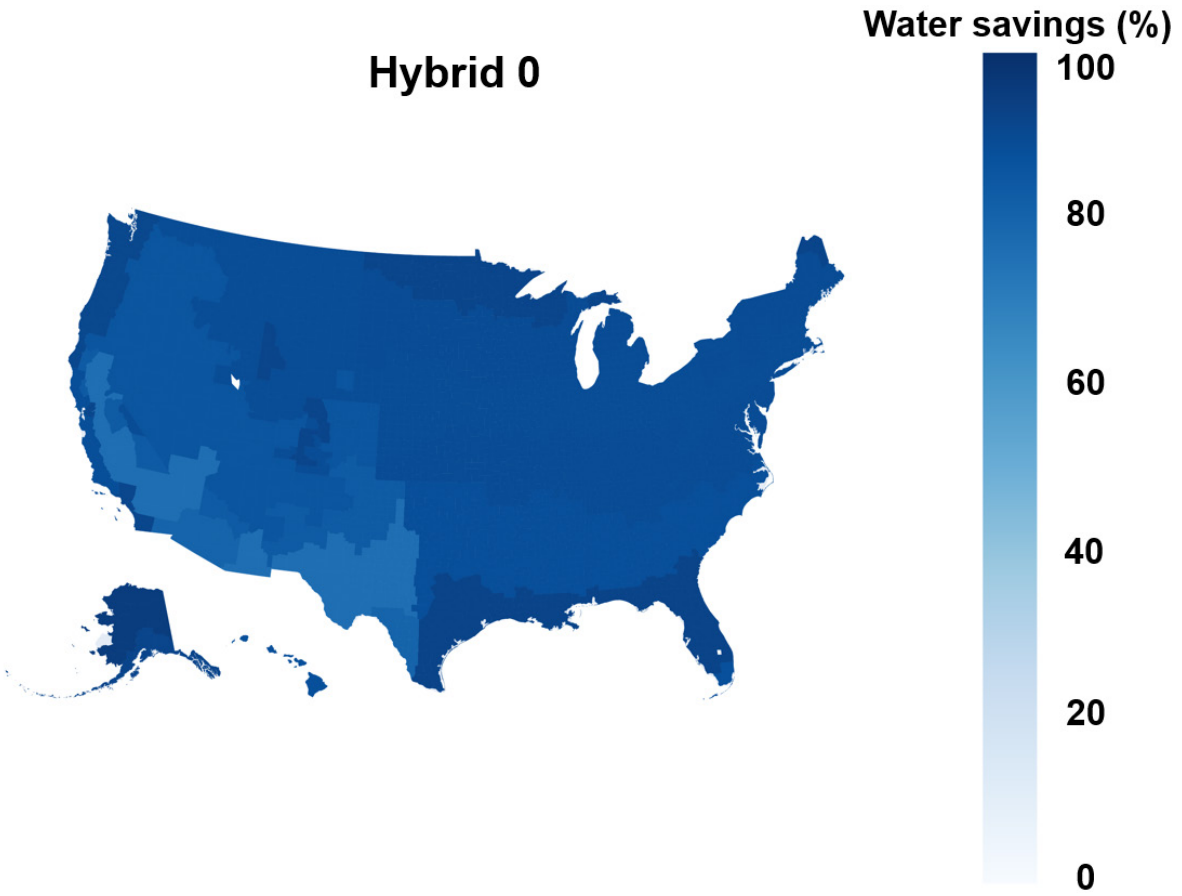

*Figure 53 – **Water savings potential of hybrid cooling panels**. Relative water savings hybrid cooling panels (Hybrid 0: solar reflector + hydrogel) versus evaporative condensers for a standard 4181 m² supermarket across the United States based on local climates zones in. A 10% rooftop coverage is assumed for the hybrid cooling panels.*

In Figure 52 and Figure 53, we fixed the hybrid cooling panels coverage to 10% of the total rooftop surface area (418 m²) for the sake of simplicity. Changing the rooftop panel coverage can however help optimize energy savings, water consumption and the payback period (see Figure 54).

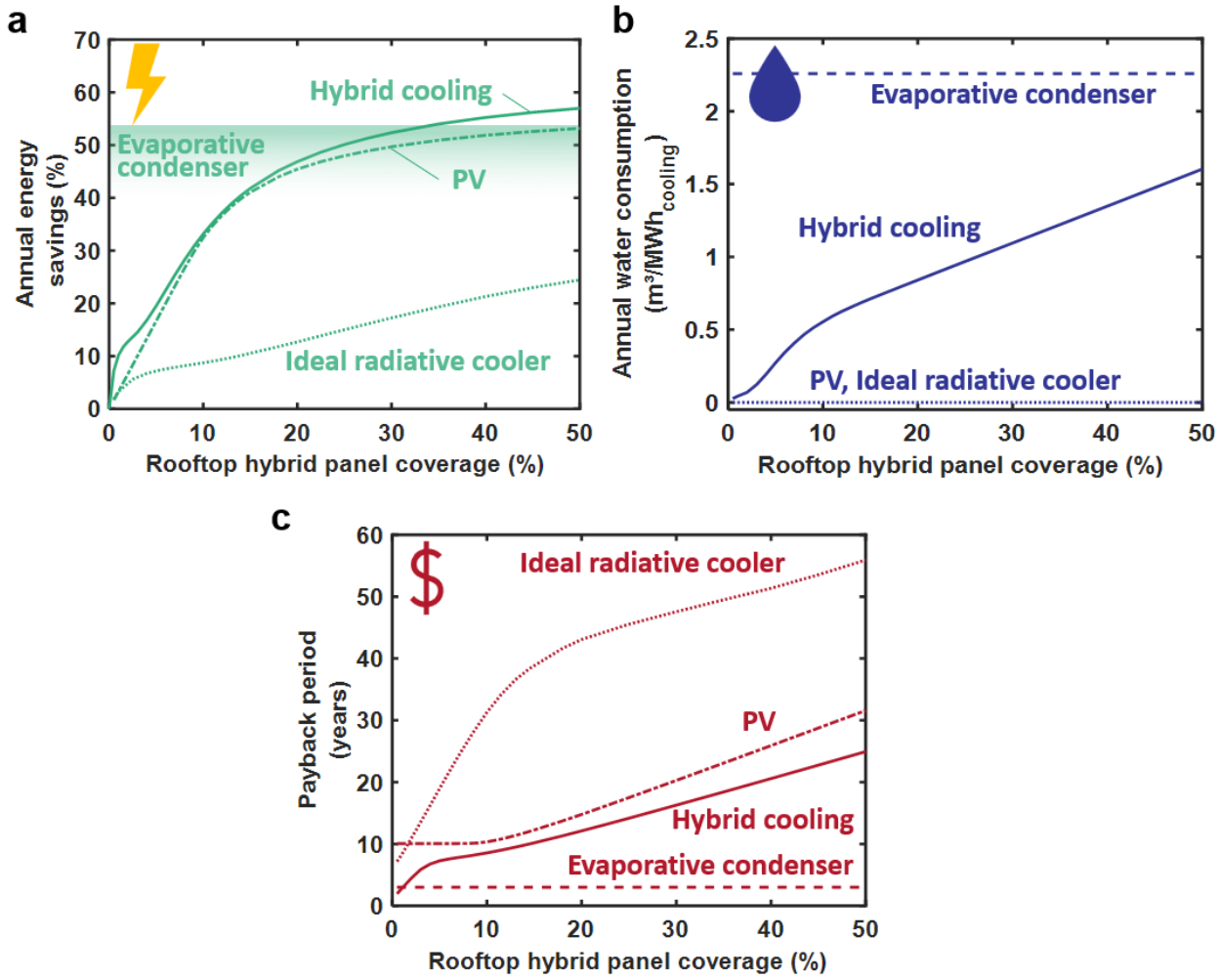

*Figure 54 – **Optimizing rooftop coverage.** (a) Annual energy savings, (b) water consumption per cooling load, and (c) estimated payback period for different condenser technologies and photovoltaics (PV) as a function of rooftop coverage. A standard supermarket in Las Vegas (3B) was used for modeling. Evaporative condensers do not occupy a significant portion of the rooftop, but are shown as a line here for the sake of comparison.*

In Figure 54a, we report total annual energy savings as a function of the rooftop coverage. We compare the hybrid cooling to an evaporative condenser, an ideal radiative cooler and PV. The evaporative condenser area represents the performance of evaporative condensers with an approach temperature of 5 °F - 15 °F [132], [133] to the wet-bulb temperature. For the ideal radiative cooler, we assume an ideal step emitter with no polyethylene aerogel insulation. For PV, we assume that there is no electricity storage, and that the electricity is only used to meet the cooling energy demand. Because of the large mismatch between the building cooling load and the PV power generation (see Figure 55), PV cannot provide 100% energy savings under these assumptions. We note that addition of electricity storage could help achieve that but would increase costs. The results show that at high rooftop coverage, hybrid cooling can be competitive with evaporative condensers and PV, while significantly beating the ideal radiative

cooler due to the larger cooling power of the hybrid structure. In Figure 54a, we compare the water consumption of the different approaches, assuming a bleed rate of 30% of the total evaporation for the hybrid cooling and evaporative condenser. At a rooftop coverage of 20%, the hybrid cooling panels can provide similar energy savings as evaporative condensers yet reduce water consumption by 62%. At lower rooftop coverage, water consumption drops even further.

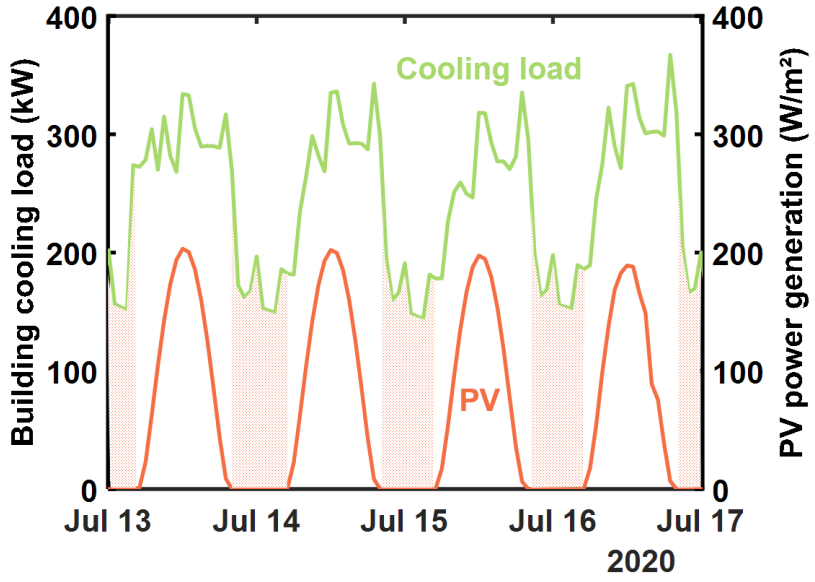

*Figure 55 – **Intermittency of photovoltaic power generation**. Photovoltaics (PV) modules can only generate electricity when the sun is shining. This creates a mismatch between the building cooling load and the PV power generation. To alleviate this problem, PV power generation must be matched with electricity storage or other sources of power generation (e.g., hydro, wind, gas or nuclear).*

Finally, in Figure 54c we estimate the payback period of the different technologies as a function of rooftop coverage. We assume a total PV cost of $344/m² based on publicly available cost data for commercial PV installations [134] and a sunlight-to-electricity conversion efficiency of 20%. The electricity rate was taken as constant and equal to $0.084/kWh [135]. Because of the similarity (structural components, installations, permits, etc.) between rooftop PV modules and hybrid and radiative cooling panels, we used the cost breakdown presented in ref. [134] to estimate the cost of our hybrid ($291/m²) and radiative cooling panels ($280/m²). For evaporative condensers, we assumed a fixed payback period of three years. The results show that the hybrid cooling panel can beat PV and an ideal radiative cooler in terms of payback period (8.5 years or less below 10% rooftop coverage) yet fall short to evaporative condensers. We note that the effects of PV power generation and building cooling load mismatch are not important below 10% rooftop coverage, which explains the constant payback period. Overall, the results presented here show that hybrid cooling panels can provide high energy savings with relatively low water consumption compared to evaporative condensers in hot and dry climates such as in Las Vegas. Finally, we note that different buildings with different cooling load profiles, baseline cooling system efficiency, or

climate regions will have different results and conclusions. An example of the influence of the baseline refrigeration system efficiency on the hybrid panel energy savings is presented in Figure 56. Results show that hybrid cooling panels achieve higher annual energy savings per panel area for lower efficiency cooling systems ($COP_{baseline}$ = 2.0) than for higher efficiency cooling systems ($COP_{baseline}$ = 3.8). These results reflect the way the hybrid cooling panels are integrated into the cooling cycle (see Figure 49) – the panels provide refrigerant subcooling which provides additional cooling at the evaporator for a constant compressor work. As such, the larger the compressor work for a same baseline cooling capacity at the evaporator (lower $COP_{baseline}$), the larger the total energy savings brought by the hybrid cooling panel refrigerant subcooling.

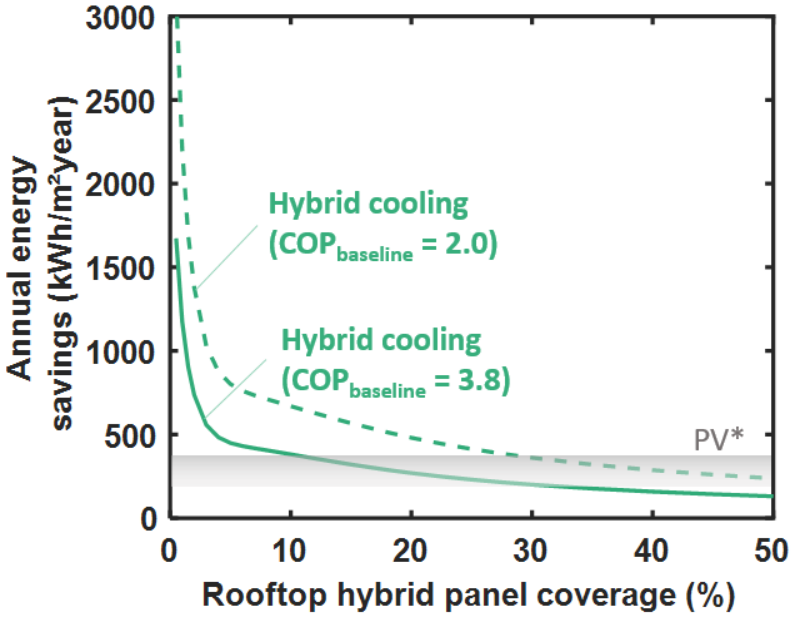

*Figure 56 – **Influence of baseline COP on energy savings.** Comparison of the hybrid cooling panels annual energy savings per panel area as a function of rooftop coverage for a low performance ($COP_{baseline}$ = 2.0) and high performance ($COP_{baseline}$ = 3.8) refrigeration system. Here, PV annual energy savings are represented by a rooftop-coverage-independent band to account for the efficiency of different types of PV (thin film, standard PV, and premium PV as per the NREL PVWatts calculator) with electrical storage.*

6.4. SUMMARY

In summary, we have studied the potential impact of our passive hybrid cooling structure on the storage of food produce and on the refrigeration energy use in supermarkets across the United States. For the storage of food produce, we proposed a simple passive hybrid evaporative-radiative cooler for post-harvest food storage. With the help of modeling, we showed that the hybrid cooler could extend the green life of bananas by 50% on average across the United States. For building cooling, we proposed a passive cooling panel that can be installed on the rooftop of buildings and that can help reduce the vapor-

compression cycle condenser-side temperature or provide refrigerant subcooling. Using a comprehensive model accounting for refrigeration cooling load in different climates across the United States, we predicted the potential energy and water savings from the hybrid cooling panels over traditional air-cooled condensers in supermarkets. Our results show promising energy and water savings over existing technologies and short payback period in hot and dry regions.

Chapter 7

7. Summary, Future Work and Perspective

7.1. SUMMARY

Subambient cooling is vital in our everyday life. Yet existing technologies consume too much energy, are responsible for significant CO_2 emissions or are not adequate for developing regions with lower income and a lack of reliable electricity. Subambient passive cooling technologies have the potential to address these problems while minimizing food shortages, promoting human well-being, and driving sustainable economic growth around the world. In this work, we have developed a porous, vapor permeable, optically selective, and thermally insulating polyethylene aerogel (PEA) that helps passive radiative and evaporative coolers achieve colder subambient temperatures and higher cooling powers throughout the day compared to previous demonstrations. By combining our passive cooling technology with buildings or passive refrigeration units, we have demonstrated a possible path to reducing space cooling energy use in buildings and increasing the lifetime of food produce in remote locations, which are promising steps towards addressing the looming cold crunch.

In Chapter 1, we covered the current challenges in space cooling and food produce storage around the world. We also provided a technical background on passive evaporative and radiative cooling as well as a review of previous literature work in these areas.

In Chapter 2, we introduced PEA as a potential thermal insulation material candidate for passive cooling applications. We described the fabrication process, characterized its optical, thermal and water vapor transport properties, its contact angle with water, and then presented a model capturing radiative transfer inside the material.

In Chapters 3-4, we theoretically and experimentally explored the benefits of combining PEA with existing radiative cooling emitters. We demonstrated that PEA can help a radiative cooling emitter achieve colder stagnation temperatures during the day and night compared to an uncovered emitter due to its thermally and optically insulating effect. We also showed that PEA pigmented with ZnS could achieve even better solar reflectance and optically selectivity than unpigmented covers, decoupling solar absorption at the emitter from its optical properties in the solar spectrum.

In Chapters 5-6, we proposed to combine both evaporative and radiative cooling into a single cooling architecture and demonstrated both experimentally and theoretically the ability of this structure to achieve

colder temperatures, higher cooling powers and lower water consumption than the individual cooling methods. We finally showed how this cooling architecture could be used in buildings to reduce space cooling energy consumption and in passive refrigeration systems in remote locations to improve the lifetime of food produce.

7.2. FUTURE WORK

We have demonstrated the cooling performance and the potential benefits of pure radiative or hybrid evaporative and radiative cooling architectures. Yet, our experimental demonstrations remained at the lab-scale and did not study long term performance. At the same time, we only just started exploring how to integrate cooling panels with HVAC systems, and what type of buildings, HVAC systems and regions would benefit the most from this technology. Finally, future innovations at the material, panel and system level could provide additional energy or water savings in a broader set of climates and buildings.

7.2.1. Scaling Up

Our experiments were limited to lab-scale 10-cm diameter samples to demonstrate the cooling potential and performance of the proposed passive radiative and hybrid cooling approaches with PEA. For at-scale deployment of cooling panels for space cooling in commercial and residential buildings or of passive refrigeration units, more work will be needed to scale up our current experimental design to larger cooling structures.

Scaling up our lab-scale design to large-scale cooling areas will require cheap materials for the selective emitter (or solar reflector), the evaporating (for hybrid systems) and the insulation layers that can easily be manufactured at scale. While selective emitters, solar reflectors and hydrogels are already being manufactured at scale and can be relatively low cost, aerogels manufacturing is still costly due to the critical point drying (or freeze-drying step) which requires significant capital investment. In this thesis, we used PEAs to demonstrate the potential of optically selective, vapor-permeable, and thermally insulating covers for passive radiative and hybrid evaporative and radiative cooling systems. However, throughout our work, we found that low-density PEAs can be quite soft and prone to damage, and expensive and time-consuming to fabricate due to the solvent exchanges and the critical point drying steps. Future material development, advances in aerogel manufacturing or alternative recipes that can address cost, robustness and scalability will thus have to be found if this type of insulation is to be used at scale in harsh environments over long periods of time. Methods to attach PEA to the emitter and to the frame will also have to be devised. In any case, it will also be interesting to explore other materials. In

fact, I believe one should not be solely focused on PEA, but rather on the motivation behind and the potential of this class of optically selective, vapor-permeable, and thermally insulating materials. Moving forward, I hope that the results obtained in this thesis will encourage not only future development of better performing, cheaper, and more scalable and robust covers, but also open up new applications that can help improve people's live and the environment.

7.2.2. Continuous Long-Term Operation

In our experiments, we did not need to worry about dirt accumulation on the PEA, damage of the materials from the environment (rain, hail, strong winds, etc.), UV degradation of the PEA, hydrogel, or selective emitter, recharging the hydrogel, or scaling, fouling or biological growth in the hydrogel and other surfaces exposed to water due to the short (~day) experiments. Continuous and long-term operation of a cooling structure using PEA, hydrogels and selective emitters will however be crucial for real products.

At the material level, we will need to first characterize over time the behavior of the PEA (or other insulation), hydrogel and selective emitter layers when exposed to these external stresses, and then find solutions to any issues that arise.

To ensure continuous operation, the hydrogel or the water-rich layer will have to be continuously replenished. In Figure 57, we briefly propose two hybrid cooling panels concepts to address water replenishment. For simplicity, the PEA insulation layer is not shown. In Figure 57a, we use a hydrogel layer on top of a solar reflector to wick water from a lower reservoir. In Figure 57b, water flows from the top of the panel to the bottom where water is collected and then recirculated. That water layer can be either plain water or can be a hydrogel with embedded water channels. Recent work [17] has demonstrated internal water channels in polyvinyl alcohol hydrogels for thermal management applications, which could provide an attractive solution here if wicking alone is not enough.

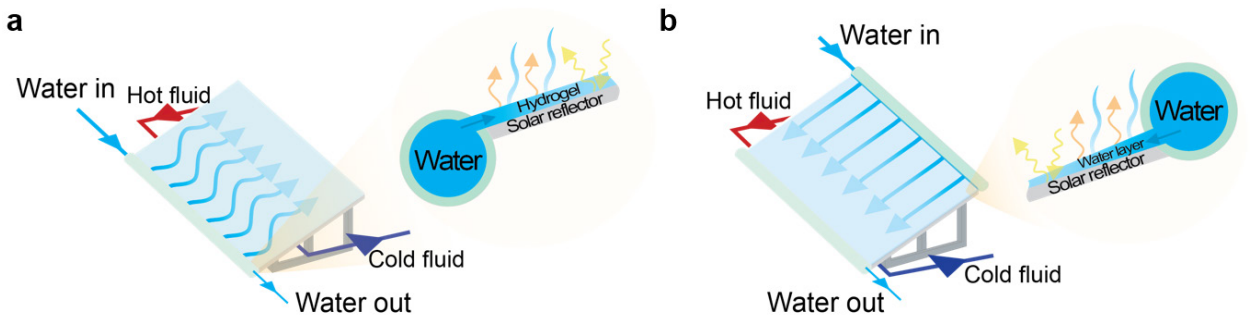

Figure 57 – ***Concepts for hybrid cooling panels****. (a) A hydrogel on top of the solar reflector wicks water from a reservoir at the bottom of the panel. (b) Water flows from top to bottom on top of a solar reflector, or inside a hydrogel layer.*

7.2.3. Addressing Water Treatment and Management in Hybrid Cooling Panels

Proper panel design and water treatment and management will be crucial in preventing deposition, corrosion, and biological growth which all tend to reduce the system's lifetime and performance while increasing costs. Adequate management and prevention of these phenomena have presented major challenges in existing and past cooling towers and boilers and are expected to be even more difficult to tackle with hybrid cooling panels due to the importance of both the optical and thermal properties of the evaporating surface. As such, appropriate water treatment and management strategies will be critical to reduce water-related issues. For reference, a good summary of water treatment practices is presented in the *ASHRAE Handbook on Heating, Ventilating, and Air-Conditioning Applications* [136].

Depending on its source, water can have varying levels of impurities which can affect its propensity to cause deposition, corrosion or favor biological growth. Typical impurities include calcium and magnesium (defined by the water hardness), carbonate, bicarbonate, borate, hydroxide, and phosphate (defined by the water alkalinity), chloride and sulfate salts, iron, silica as well as other organic solids and biological matter. To quantify the amount of each of these impurities, water is typically characterized by its hardness (linked to its potential to form calcium and magnesium scale), alkalinity (capacity of water to neutralize acids or base which leads to calcium/magnesium carbonate scale formation), pH (low pH can lead to corrosion), turbidity (water haziness which can cause plugging, foaming or sedimentation), levels of chlorides (lead to corrosion) and sulfates (contribute to scale), its total dissolved solids (TDS) or conductivity, and its biological matter. All these parameters must typically be tightly controlled within a defined range depending on the materials in the systems all throughout the evaporation process to minimize the effects of deposition, corrosion, and biological growth. On the one side, potable municipal water sources in the United States are typically of higher quality with relatively constant properties which minimizes water treatment requirements. On the other side, alternative sources of water such as the ocean,

rivers, lakes, groundwater, wastewater and reclaim water will however present more variation in their properties with higher TDS and biological activity, posing additional challenges to cooling towers and water treatment systems. Depending on the location, existing water infrastructure, water availability, and the amount of water needed for cooling purposes, evaporative cooling might not be economically viable or may require lower quality water sources.

To mitigate deposition, corrosion, and biological growth in large scale hybrid cooling panels, several strategies that have been used in cooling towers could similarly be used. Firstly, the makeup water can be treated by reverse osmosis, ion exchange or deionization to reduce its content of dissolved solids and limit the concentration of scale-forming dissolved solids. Other treatments such as acid treatments can also help reduce alkalinity to prevent scale formation from carbonates. Additionally, water can be treated with scale inhibitors that extend the time for nucleation of scale deposit or scale conditioners that control the scale crystal structure to decrease its tendency to stick to surfaces. Secondly, the system design (hybrid cooling panel, evaporating layer, piping, and heat exchanger) should be made of non-corroding material such as PVC or polypropylene which have been used extensively in the industry due to their low cost, ease of manufacture and ability to resist corrosion. Thirdly, adequate biological control should be adopted. Wetted surfaces should be shielded from sunlight as much as possible to reduce algae growth. The use of solar reflecting, infrared transparent and vapor permeable covers such as PEA, proper orientation of the hybrid cooling panels towards the north and reducing low flow areas in the water loops should all be explored to minimize algae growth. Biocides such as oxidizing chemical biocides (chlorine, bromine, ozone, hydrogen peroxide), nonoxidizing biocides, biocidal paint, or water exposure to ultraviolet light may also be required to prevent biological growth within the hybrid cooling panels or in the piping. Aside from the undesired growth of biological life, we further note that biofilm growth on top of surfaces can lead to increase corrosion due to low pH conditions within the biofilm and additional scale formation due to trapping of particles within the biofilm. As such, control of biological growth in hybrid cooling panels will be even more important to prevent water-related issues. Lastly, adequate monitoring of cooling water quality and scheduled water blowdown will be crucial. As water evaporates and makeup water is added to the system, the total amount of dissolved solids increases in the water. Over time, the concentration of some dissolved solids will increase beyond their solubility limit, causing precipitation or deposition on surfaces. To avoid this, water is typically periodically discharged from the system to carry out the highly concentrated dissolved minerals along with it. In practice, the frequency at which this blowdown occurs is characterized by the cycles of concentration (typically between 2 to 4) and is defined by the ratio of the makeup water volume to the blowdown water volume. Adequate water blowdown and choice of cycles of concentration will also be primordial in minimizing water consumption and water-related issues in hybrid cooling panels.

Overall, water treatment and management are complex problems that will present significant challenges in the development of large scale, long term, and continuously operating hybrid cooling panels. Nonetheless, we hope future work will be able to leverage past work and existing expertise in this field (*e.g.*, water treatment experts and companies, literature, and HVAC manufacturers) to design hybrid cooling panels and water treatment strategies that can resist deposition, corrosion, and biological growth with minimal environmental and financial costs.

7.2.4. Integration of Cooling Panels with Buildings

In the previous chapter, we proposed to combine the hybrid cooling panel in series with existing vapor compression cooling systems to provide refrigerant subcooling or lower condensation temperatures. Yet, little details were given about how to integrate the hybrid cooling panels (or pure radiative cooling panels) to existing HVAC systems in buildings. Moving forward, questions such as how to connect the cooling panel fluid loop to the HVAC refrigerant loop or condenser, what kind of water treatment is needed, are the panels constrained by buildings codes, are there regulations preventing the use of water evaporation in specific locations, or which buildings would benefit the most from hybrid or pure radiative cooling panels will need to be answered.

Another interesting research opportunity will be to explore how different refrigerants in HVAC systems affect the performance or the optimal configuration of the hybrid cooling panels. For example, some new vapor compression systems are now relying on transcritical CO_2 cycles due to the lower global warming potential of CO_2 compared to other traditional refrigerants. Because transcritical CO_2 cycles do not go through a constant temperature condensation process but rather a high to moderate temperature constant-pressure supercritical gas cooling process, this could affect the operating temperature and performance of the cooling panels. Yet, it is not clear how this would affect the performance and potential water and energy savings of cooling panels compared to HVAC systems using more traditional refrigerants such as was the case in this thesis. More work is thus required in that area and could provide interesting insights and research directions.

Finally, while we have assumed the cooling panels to be connected in series with vapor compression systems, the panels are not limited to this configuration. In some industries like data center cooling, vapor compression systems are not always required and free cooling with the ambient air can often be sufficient to maintain the server at their target operating temperature. But while free cooling can help achieve significant energy savings in data centers compared to vapor-compression-only cooling, free cooling is only possible when the ambient dry-bulb or wet-bulb temperatures are low enough, limiting its use to

only a limited number of hours annually or to colder regions. By using hybrid or pure radiative cooling panels, it would be possible to extend the range of operating ambient temperatures to further extend the operating hours of free cooling, thus cutting down on energy consumption while also enabling free cooling in warmer climates and lower water consumption compared to evaporating coolers [137].

7.2.5. Passive Refrigeration

In Chapter 6, we proposed a passive food produce cooler using a hybrid cooling architecture. Aside from addressing scalability, robustness, durability, and cost issues, a more complete design of a passive food produce cooler using passive cooling will also need to be developed and tested. I believe there are many opportunities to innovate at the design level using fundamental principles of mechanical engineering such as thermodynamics, heat and mass transfer, and fluid dynamics, to deliver a final product that is simple to use and achieves high performance with cheap and locally available materials.

7.2.6. Innovations

Many opportunities for innovation still remain in hybrid evaporative and radiative cooling systems that can help achieve higher energy and water savings.

One particularly interesting research opportunity is to study the use of sorbents inside the evaporating layer to provide water regeneration capabilities and reduce water consumption. Prior work [18], [116] has shown this approach to be promising by replenishing the water-rich evaporating layer at night when the cooling load is low using adsorption from the sorbent material. Yet, existing work remained at the lab-scale and has not demonstrated a thorough understanding of the optimal sorbent material and isotherm in different climates, as well as the influence of the adsorption heat on the efficiency of cooling systems.

Another promising field of research are switchable optical properties [138]. The ability to switch optical properties from a solar reflecting and IR emitting material to a solar absorbing and IR reflecting material could make the panels much more attractive in colder climates where space cooling is only required during the hottest months of the year and space heating is required the rest of the year. A panel with such tunable optical properties could thus provide cold water to the condenser side of vapor compression cooling systems in the summer and hot water to the evaporator side of vapor compression heating systems in the winter. By doing so, we could maximize the utilization factor of the panels, provide shorter payback period through increased annual energy savings, and enable wider adoption of the panels in colder climates and in residential and commercial buildings.

In Chapter 2 of this thesis, we suggested that decreasing the pore size in PEA, reducing the gas pressure, or replacing the gas within PEA with a lower thermal conductivity gas could all help decrease the thermal conductivity of the material. Previous attempts at reducing PEA mean pore size (rapid cooling by doing the thermally induced phase separation in liquid nitrogen, using other solvents with varying viscosities or affinity for polyethylene, and using additive to promote nucleation) have so far failed to provide the necessary change in pore size. Finding a way to create a low-density, porous polyethylene network with a mean pore size below 100 nm could help significantly cut the thermal conductivity of the material which would allow for even lower temperatures and thinner PEA and could even help the material find a use in other applications requiring low thermal conductivity. Similarly, additional work is still needed to make a PEA with lower inner gas pressure or with a different internal gas. Such a PEA cover would need a physical barrier that prevents diffusion of gases across it to maintain the pressure or gas species difference while still being infrared transparent.

Finally, it would also be interesting to explore thermal energy storage combined with our hybrid cooling panels in future work. Thermal energy storage has the potential to leverage colder temperatures and lower cooling demand at night to produce cold water that can then be used at peak load during the day. This could help decrease the hybrid cooling panel surface area or improve the cooling energy savings. Overall, future opportunities are still numerous and exciting.

7.3. PERSPECTIVE

Passive cooling solutions such as radiative and evaporative cooling have the potential to bring the much-needed energy savings in buildings and to broaden access to subambient cooling in developing countries. Motivated with this potential, several startups have already emerged from that field and have been developing and selling radiative cooling panels for commercial buildings. Future developments in this field will no longer focus on optical and thermal properties of the emitting or evaporating materials but will rather focus more on practical challenges such as durability, scalability, reliability, and most importantly, cost. With the field moving forward, the overall performance of passive radiative and evaporative cooling systems will now be compared to that of alternative technologies such as air-cooled and evaporative cooling units and photovoltaics, which are all competing for the same rooftop area on buildings. Aside from space cooling and food produce storage, many other applications such as personal thermal management, urban cooling, power generation and power systems will benefit from advances in the field.

Moving ahead, I think it is also important to consider the limitations of these technologies. It would be optimistic to believe that pure radiative cooling or even hybrid evaporative and radiative cooling could

one day completely replace vapor compression cooling systems in buildings or refrigerators for food or vaccine storage. The inherently low cooling power and dependence on the ambient weather conditions of these technologies mean that they will most likely play a support role in these applications, helping reduce the cooling energy consumption in buildings or provide subambient cooling to food produce. Nevertheless, I believe these passive cooling technologies still have a promising future in which they will help our generation address climate change and the looming cold crunch. I am excited about this future and look forward to seeing all the different and creative implementations of these technologies in our everyday life.

Bibliography

[1] International Energy Agency, “The Future of Cooling: Opportunities for energy- efficient air conditioning,” 2018.

[2] U.S. Energy Information Administration, “Monthly Energy Review - April 2021,” 2021.

[3] *The State of Food Security and Nutrition in the World 2020*. FAO, IFAD, UNICEF, WFP and WHO, 2020.

[4] J. A. Foley *et al.*, “Solutions for a cultivated planet,” *Nature*, vol. 478, no. 7369, pp. 337–342, Oct. 2011.

[5] J. Gustavsson, C. Cederberg, U. Sonesson, and A. Emanuelsson, *The methodology of the FAO study: “Global Food Losses and Food Waste - extent, causes and prevention,”* no. 857. The Swedish Institute for Food and Biotechnology, 2013.

[6] B. M. McGregor, “Tropical Products Transport Handbook,” 1989.

[7] ASHRAE, “Commodity storage requirements,” *ASHRAE Handb. - Refrig.*, pp. 21.1-21.11, 2014.

[8] T. P. Labuza and W. M. Breene, “Applications of ‘Active Packaging’ for Improvement of Shelf-Life and Nutritional Quality of Fresh and Extended Shelf-Life Foods,” *J. Food Process. Preserv.*, vol. 13, no. 1, pp. 1–69, 1989.

[9] R. Jedermann, M. Nicometo, I. Uysal, and W. Lang, “Reducing food losses by intelligent food logistics,” *Philos. Trans. R. Soc. A Math. Phys. Eng. Sci.*, vol. 372, no. 2017, 2014.

[10] P. L. Today, “Alternative refrigeration - Three methods of passive cooling,” 2013. [Online]. Available: www.provident-living-today.com/Alternative-Refrigeration.html. [Accessed: 01-Sep-2019].

[11] Z. Lu, E. Strobach, N. Chen, N. Ferralis, and J. C. Grossman, “Passive Sub-Ambient Cooling from a Transparent Evaporation-Insulation Bilayer,” *Joule*, vol. 4, no. 12, pp. 2693–2701, Dec. 2020.

[12] S. Cui, C. Ahn, M. C. Wingert, D. Leung, S. Cai, and R. Chen, “Bio-inspired effective and regenerable building cooling using tough hydrogels,” *Appl. Energy*, vol. 168, pp. 332–339, 2016.

[13] A. C. C. Rotzetter *et al.*, “Thermoresponsive Polymer Induced Sweating Surfaces as an Efficient Way to Passively Cool Buildings,” *Adv. Mater.*, vol. 24, no. 39, pp. 5352–5356, Oct. 2012.

[14] S. Ferber *et al.*, “Evaporative Cooling Hydrogel Packaging for Storing Biologics Outside of the Cold Chain,” *Adv. Healthc. Mater.*, vol. 7, no. 14, p. 1800220, 2018.

[15] E. Verploegen, R. Ekka, and G. Gill, “Evaporative Cooling for Improved Vegetable and Fruit Storage in Rwanda and Burkina Faso,” 2019.

[16] R. Li, Y. Shi, M. Wu, S. Hong, and P. Wang, “Photovoltaic panel cooling by atmospheric water sorption–evaporation cycle,” *Nat. Sustain.*, vol. 3, no. 8, pp. 636–643, Aug. 2020.

[17] M. Zamengo and J. Morikawa, “Evaluation of cooling ability for a novel heat sink made of polyvinyl alcohol hydrogel,” *Int. J. Heat Mass Transf.*, vol. 143, p. 118523, Nov. 2019.

[18] C. Wang, L. Hua, H. Yan, B. Li, Y. Tu, and R. Wang, “A Thermal Management Strategy for Electronic Devices Based on Moisture Sorption-Desorption Processes,” *Joule*, vol. 4, no. 2, pp. 435–447, 2020.

[19] R. Zhao, S. Zhang, J. Gu, J. Liu, S. Carkner, and E. Lanoue, “An experimental study of lithium ion battery thermal management using flexible hydrogel films,” *J. Power Sources*, vol. 255, pp. 29–36, Jun. 2014.

[20] S. Pu *et al.*, “Promoting Energy Efficiency via a Self-Adaptive Evaporative Cooling Hydrogel,” *Adv. Mater.*, vol. 32, no. 17, p. 1907307, Apr. 2020.

[21] E. Verploegen, P. Rinker, and K. E. Ognakossan, “Evaporative cooling best practices,” 2018.

[22] C. G. Granqvist, A. Hjortsberg, and T. S. Eriksson, “Radiative cooling to low temperatures with selectivity IR-emitting surfaces,” *Thin Solid Films*, vol. 90, no. 2, pp. 187–190, 1982.

[23] F. Trombe, “Perspectives sur l’utilisation des rayonnements solaires et terrestres dans certaines régions du monde,” *Rev. Générale Therm.*, vol. 6, no. 70, pp. 1285–1314, 1967.

[24] D. Zhao *et al.*, “Subambient Cooling of Water: Toward Real-World Applications of Daytime Radiative Cooling,” *Joule*, vol. 3, no. 1, pp. 111–123, Jan. 2019.

[25] A. P. Raman, M. A. Anoma, L. Zhu, E. Rephaeli, and S. Fan, “Passive radiative cooling below ambient air temperature under direct sunlight,” *Nature*, vol. 515, no. 7528, pp. 540–544, 2014.

[26] Z. Chen, L. Zhu, A. Raman, and S. Fan, “Radiative cooling to deep sub-freezing temperatures through a 24-h day–night cycle,” *Nat. Commun.*, vol. 7, no. 1, p. 13729, Dec. 2016.

[27] A. R. Gentle, A. Nuhoglu, M. D. Arnold, and G. B. Smith, “3D printable optical structures for sub-ambient sky cooling,” in *Thermal Radiation Management for Energy Applications*, 2017, no.

September, p. 10.

[28] L. Zhu, A. Raman, K. X. Wang, M. A. Anoma, and S. Fan, “Radiative cooling of solar cells,” *Optica*, vol. 1, no. 1, pp. 32–38, 2014.

[29] L. Zhu, A. P. Raman, and S. Fan, “Radiative cooling of solar absorbers using a visibly transparent photonic crystal thermal blackbody,” *Proc. Natl. Acad. Sci.*, vol. 112, no. 40, pp. 12282–12287, Oct. 2015.

[30] L. Zhu, A. Raman, and S. Fan, “Color-preserving daytime radiative cooling,” *Appl. Phys. Lett.*, vol. 103, no. 22, p. 223902, Nov. 2013.

[31] A. R. Gentle and G. B. Smith, “Radiative Heat Pumping from the Earth Using,” pp. 373–379, 2010.

[32] Y. Zhai *et al.*, “Scalable-manufactured randomized glass-polymer hybrid metamaterial for daytime radiative cooling,” *Science (80-.).*, vol. 355, no. 6329, pp. 1062–1066, Mar. 2017.

[33] P. Yang, C. Chen, and Z. M. Zhang, “A dual-layer structure with record-high solar reflectance for daytime radiative cooling,” *Sol. Energy*, vol. 169, no. April, pp. 316–324, Jul. 2018.

[34] J. Mandal *et al.*, “Hierarchically porous polymer coatings for highly efficient passive daytime radiative cooling,” *Science (80-.).*, vol. 362, no. 6412, pp. 315–319, Oct. 2018.

[35] D. Li *et al.*, “Scalable and hierarchically designed polymer film as a selective thermal emitter for high-performance all-day radiative cooling,” *Nat. Nanotechnol.*, vol. 16, no. 2, pp. 153–158, Feb. 2021.

[36] A. W. Harrison and M. R. Walton, “Radiative cooling of TiO2 white paint,” *Sol. Energy*, vol. 20, no. 2, pp. 185–188, 1978.

[37] X. Li, J. Peoples, P. Yao, and X. Ruan, “ Ultrawhite BaSO 4 Paints and Films for Remarkable Daytime Subambient Radiative Cooling ,” *ACS Appl. Mater. Interfaces*, 2021.

[38] X. Li, J. Peoples, Z. Huang, J. Qiu, and X. Ruan, “SCALABLE METAL-FREE PAINT FOR PASSIVE RADIATIVE COOLING,” in *The Second Pacific Rim Thermal Engineering Conference*, 2019, pp. 3–5.

[39] A. Hjortsberg and C. G. Granqvist, “Radiative cooling with selectively emitting ethylene gas,” *Appl. Phys. Lett.*, vol. 39, no. 6, pp. 507–509, Sep. 1981.

[40] E. M. Lushiku, A. Hjortsberg, and C. G. Granqvist, “Radiative cooling with selectively infrared-

emitting ammonia gas," *J. Appl. Phys.*, vol. 53, no. 8, pp. 5526–5530, 1982.

[41] J. Kou, Z. Jurado, Z. Chen, S. Fan, and A. J. Minnich, "Daytime Radiative Cooling Using Near-Black Infrared Emitters," *ACS Photonics*, vol. 4, no. 3, pp. 626–630, Mar. 2017.

[42] E. M. Lushiku, A. Hjortsberg, and C. G. Granqvist, "Radiative cooling with selectively infrared-emitting ammonia gas," *J. Appl. Phys.*, vol. 53, no. 8, pp. 5526–5530, Aug. 1982.

[43] B. Bhatia *et al.*, "Passive directional sub-ambient daytime radiative cooling," *Nat. Commun.*, vol. 9, no. 1, p. 5001, Dec. 2018.

[44] Y. Peng *et al.*, "Nanoporous polyethylene microfibres for large-scale radiative cooling fabric," *Nat. Sustain.*, vol. 1, no. 2, pp. 105–112, Feb. 2018.

[45] P.-C. Hsu *et al.*, "Radiative human body cooling by nanoporous polyethylene textile," *Science (80-.).*, vol. 353, no. 6303, pp. 1019–1023, Sep. 2016.

[46] M. Yang *et al.*, "Bioinspired 'Skin' with Cooperative Thermo-Optical Effect for Daytime Radiative Cooling," *ACS Appl. Mater. Interfaces*, vol. 12, no. 22, pp. 25286–25293, Jun. 2020.

[47] H. Kim and A. Lenert, "Optical and thermal filtering nanoporous materials for sub-ambient radiative cooling," *J. Opt.*, vol. 20, no. 8, p. 084002, Aug. 2018.

[48] N. A. Nilsson, T. S. Eriksson, and C. G. Granqvist, "Infrared-transparent convection shields for radiative cooling: Initial results on corrugated polyethylene foils," *Sol. Energy Mater.*, vol. 12, no. 5, pp. 327–333, Nov. 1985.

[49] A. R. Gentle, K. L. Dybdal, and G. B. Smith, "Polymeric mesh for durable infra-red transparent convection shields: Applications in cool roofs and sky cooling," *Sol. Energy Mater. Sol. Cells*, vol. 115, pp. 79–85, Aug. 2013.

[50] S. N. Bathgate and S. G. Bosi, "A robust convection cover material for selective radiative cooling applications," *Sol. Energy Mater. Sol. Cells*, vol. 95, no. 10, pp. 2778–2785, 2011.

[51] M. Benlattar, E. M. Oualim, M. Harmouchi, A. Mouhsen, and A. Belafhal, "Radiative properties of cadmium telluride thin film as radiative cooling materials," *Opt. Commun.*, vol. 256, no. 1–3, pp. 10–15, 2005.

[52] Z. Chen, L. Zhu, W. Li, and S. Fan, "Simultaneously and Synergistically Harvest Energy from the Sun and Outer Space," *Joule*, pp. 1–10, Nov. 2018.

[53] J. Zhang *et al.*, "Mechanically Robust and Spectrally Selective Convection Shield for Daytime

Subambient Radiative Cooling," *ACS Appl. Mater. Interfaces*, vol. 13, no. 12, pp. 14132–14140, Mar. 2021.

[54] X. Li *et al.*, "Integration of daytime radiative cooling and solar heating for year-round energy saving in buildings," *Nat. Commun.*, vol. 11, no. 1, pp. 1–9, 2020.

[55] D. Zhao *et al.*, "Subambient Cooling of Water : Toward Real- World Applications of Daytime Radiative Cooling Subambient Cooling of Water : Toward Real-World Applications of Daytime Radiative Cooling," *Joule*, pp. 1–13, 2019.

[56] Y. Zhai *et al.*, "Scalable-manufactured randomized glass-polymer hybrid metamaterial for daytime radiative cooling," vol. 7899, pp. 1–9, 2017.

[57] A. R. Gentle and G. B. Smith, "A Subambient Open Roof Surface under the Mid-Summer Sun," *Adv. Sci.*, vol. 2, no. 9, p. 1500119, Sep. 2015.

[58] Y. A. Attia, "Polyethylene aerogels and method of their production," US 9,034,934 B1, 2015.

[59] C. Daniel, S. Longo, and G. Guerra, "High porosity polyethylene aerogels," *Polyolefins J.*, vol. 2, no. 1, pp. 49–55, 2015.

[60] J. V. Gulmine, P. R. Janissek, H. M. Heise, and L. Akcelrud, "Polyethylene characterization by FTIR," *Polym. Test.*, vol. 21, no. 5, pp. 557–563, Jan. 2002.

[61] G. W. Ball, R. Hurd, and M. G. Walker, "The Thermal Conductivity on Rigid Urethane Foams," *J. Cell. Plast.*, vol. 6, no. 2, pp. 66–75, Mar. 1970.

[62] X. Lu, R. Caps, J. Fricke, C. T. Alviso, and R. W. Pekala, "Correlation between structure and thermal conductivity of organic aerogels," *J. Non. Cryst. Solids*, vol. 188, no. 3, pp. 226–234, Aug. 1995.

[63] L. W. Hrubesh and R. W. Pekala, "Thermal properties of organic and inorganic aerogels," *J. Mater. Res.*, vol. 9, no. 03, pp. 731–738, 1994.

[64] T. Xie and Y. He, "Heat transfer characteristics of silica aerogel composite materials: Structure reconstruction and numerical modeling," *Int. J. Heat Mass Transf.*, vol. 95, pp. 621–635, Apr. 2016.

[65] U. Heinemann, R. Caps, and J. Fricke, "Radiation-conduction interaction : An investigation on silica aerogels," *Int. J. Heat Mass Transf.*, vol. 39, no. 10, pp. 2115–2130, 1996.

[66] K. Stamnes, G. E. Thomas, and J. J. Stamnes, *Radiative Transfer in the Atmosphere and Ocean*.

Cambridge: Cambridge University Press, 2017.

[67] A. Berk, P. Conforti, R. Kennett, T. Perkins, F. Hawes, and J. van den Bosch, “MODTRAN6: a major upgrade of the MODTRAN radiative transfer code,” in *Proceeding of SPIE 9088, Algorithms and Technologies for Multispectral, Hyperspectral, and Ultraspectral Imagery XX*, 2014, p. 90880H.

[68] L. Zhao, S. Yang, B. Bhatia, E. Strobach, and E. N. Wang, “Modeling silica aerogel optical performance by determining its radiative properties,” *AIP Adv.*, vol. 6, no. 2, 2016.

[69] W. L. Smith, “Note on the Relationship Between Total Precipitable Water and Surface Dew Point,” *J. Appl. Meteorol.*, vol. 5, no. 5, pp. 726–727, Oct. 1966.

[70] A. Leroy *et al.*, “High-performance subambient radiative cooling enabled by optically selective and thermally insulating polyethylene aerogel,” *Sci. Adv.*, vol. 5, no. 10, p. eaat9480, Oct. 2019.

[71] W. M. Rohsenow, J. P. Hartnett, and E. N. Ganic, *Handbook of Heat Transfer Fundamentals*, 2nd ed. New York: Mcgraw-Hill, 1985.

[72] M. Alvarez-Lainez, M. A. Rodriguez-Perez, and J. A. De Saja, “Thermal Conductivity of Open-Cell Polyolefin Foams,” *J. Polym. Sci. Part B Polym. Phys.*, vol. 46, no. 2, pp. 212–221, 2008.

[73] G. Wei, Y. Liu, X. Zhang, F. Yu, and X. Du, “Thermal conductivities study on silica aerogel and its composite insulation materials,” *Int. J. Heat Mass Transf.*, vol. 54, no. 11–12, pp. 2355–2366, May 2011.

[74] L. R. Glicksman, “Low density cellular plastics: Physical basis of behavior,” in *Low density cellular plastics: Physical basis of behavior*, First., N. C. Hilyard and A. Cunningham, Eds. Springer Science + Business Media, 1994, pp. 104–152.

[75] S. Q. Zeng, A. Hunt, and R. Greif, “Geometric Structure and Thermal Conductivity of Porous Medium Silica Aerogel,” *J. Heat Transfer*, vol. 117, no. 4, pp. 1055–1058, Nov. 1995.

[76] T. Xie, Y. He, and Z. Hu, “Theoretical study on thermal conductivities of silica aerogel composite insulating material,” *Int. J. Heat Mass Transf.*, vol. 58, no. 1–2, pp. 540–552, 2013.

[77] S. S. Sundarram and W. Li, “On Thermal Conductivity of Micro- and Nanocellular Polymer Foams,” *Polym. Eng. Sci.*, vol. 53, pp. 1901–1909, 2013.

[78] C. Bi and G. H. Tang, “Effective thermal conductivity of the solid backbone of aerogel,” *Int. J. Heat Mass Transf.*, vol. 64, pp. 452–456, Sep. 2013.

[79] Y. L. He and T. Xie, “Advances of thermal conductivity models of nanoscale silica aerogel insulation material,” *Appl. Therm. Eng.*, vol. 81, pp. 28–50, 2015.

[80] M. A. Rodriguez-perez, J. La, and A. De Saja, “Influence of Solid Phase Conductivity and Cellular Structure on the Heat Transfer Mechanisms of Cellular Materials : Diverse Case Studies ** By Eusebio Solo,” no. 10, pp. 818–824, 2009.

[81] B. Notario, J. Pinto, E. Solorzano, J. A. De Saja, and M. Dumon, “Experimental validation of the Knudsen effect in nanocellular polymeric foams,” vol. 56, pp. 57–67, 2015.

[82] P. Gong, P. Buahom, M. Tran, M. Saniei, C. B. Park, and P. Po, “Heat transfer in microcellular polystyrene / multi-walled carbon nanotube nanocomposite foams,” vol. 3, 2015.

[83] D. W. Van Krevelen and K. Te Nijenhuis, “Transport of Thermal Energy,” *Prop. Polym.*, pp. 645–653, 2009.

[84] J. Antonio, R. Ruiz, C. Saiz-arroyo, M. Dumon, M. A. Rodr, and L. Gonzalez, “Production , cellular structure and thermal conductivity of microcellular (methyl methacrylate)–(butyl acrylate)–(methyl methacrylate) triblock copolymers,” no. October 2010, pp. 146–152, 2011.

[85] M. G. Kaganer, *Thermal insulation in cryogenic engineering*, 1st ed. Jerusalem: Israel Program for Scientific Translations, 1969.

[86] K. Swimm, G. Reichenauer, S. Vidi, and H. P. Ebert, “Impact of thermal coupling effects on the effective thermal conductivity of aerogels,” *J. Sol-Gel Sci. Technol.*, vol. 84, no. 3, pp. 466–474, 2017.

[87] K. Swimm, S. Vidi, G. Reichenauer, and H. Ebert, “Coupling of gaseous and solid thermal conduction in porous solids Solid phase Gas phase Solid phase,” *J. Non. Cryst. Solids*, vol. 456, pp. 114–124, 2017.

[88] National Institute of Standards and Technology, “NIST Reference Fluid Thermodynamic and Transport Properties Database (REFPROP).” .

[89] M. F. Modest, *Radiative heat transfer*. Academic press, 2013.

[90] ASTM International, “ASTM C1044-16 Standard Practice for Using a Guarded-Hot-Plate Apparatus or Thin-Heater Apparatus in the Single-Sided Mode,” West Conshohocken, PA, 2016.

[91] O.-J. Lee *et al.*, “Determination of mesopore size of aerogels from thermal conductivity measurements,” *J. Non. Cryst. Solids*, vol. 298, no. 2–3, pp. 287–292, Mar. 2002.

[92] ASTM-E96/E96M, “Standard Test Methods for Water Vapor Transmission of materials, West Conshohocken,” vol. i, p. 14p., 2016.

[93] H. Kim and A. Lenert, “Wavelength Selective Cover for Sub-Ambient Passive Radiative Cooling,” in *International Heat Transfer Conference 16*, 2018, pp. 8415–8422.

[94] C. I. Ezekwe, “Performance of a heat pipe assisted night sky radiative cooler,” *Energy Convers. Manag.*, vol. 30, no. 4, pp. 403–408, 1990.

[95] E. A. Goldstein, A. P. Raman, and S. Fan, “Sub-ambient non-evaporative fluid cooling with the sky,” *Nat. Energy*, vol. 2, no. 9, p. 17143, Sep. 2017.

[96] H. Kim *et al.*, “Adsorption-based atmospheric water harvesting device for arid climates,” *Nat. Commun.*, vol. 9, no. 1, pp. 1–8, 2018.

[97] J. K. Tong, X. Huang, S. V. Boriskina, J. Loomis, Y. Xu, and G. Chen, “Infrared-Transparent Visible-Opaque Fabrics for Wearable Personal Thermal Management,” *ACS Photonics*, vol. 2, no. 6, pp. 769–778, 2015.

[98] T. Gao *et al.*, “Three-Dimensional Printed Thermal Regulation Textiles,” *ACS Nano*, vol. 11, no. 11, pp. 11513–11520, Nov. 2017.

[99] L. Cai *et al.*, “Spectrally Selective Nanocomposite Textile for Outdoor Personal Cooling,” *Adv. Mater.*, vol. 30, no. 35, pp. 1–7, 2018.

[100] L. Cai *et al.*, “Temperature Regulation in Colored Infrared-Transparent Polyethylene Textiles,” *Joule*, vol. 3, no. 6, pp. 1478–1486, 2019.

[101] T. M. J. Nilsson, G. A. Niklasson, and C. G. Granqvist, “A solar reflecting material for radiative cooling applications: ZnS pigmented polyethylene,” *Sol. Energy Mater. Sol. Cells*, vol. 28, no. 2, pp. 175–193, 1992.

[102] T. M. J. Nilsson and G. a. Niklasson, “Radiative cooling during the day: simulations and experiments on pigmented polyethylene cover foils,” *Sol. Energy Mater. Sol. Cells*, vol. 37, no. 1, pp. 93–118, 1995.

[103] Y. Mastai, Y. Diamant, S. T. Aruna, and A. Zaban, “TiO2 nanocrystalline pigmented polyethylene foils for radiative cooling applications: Synthesis and characterization,” *Langmuir*, vol. 17, no. 22, pp. 7118–7123, 2001.

[104] G. A. Niklasson and T. S. Eriksson, “Radiative Cooling With Pigmented Polyethylene Foils,” *Opt.*

Mater. Technol. Energy Effic. Sol. Energy Convers. VII, vol. 1016, no. May, p. 89, 1989.

[105] L. Cai *et al.*, "Spectrally Selective Nanocomposite Textile for Outdoor Personal Cooling," *Adv. Mater.*, vol. 30, no. 35, pp. 1–7, 2018.

[106] E. D. Palik and A. Addamanio, "Zinc Sulfide (ZnS)," in *Handbook of Optical Constants of Solids*, Washington, DC, 1998, pp. 597–619.

[107] C. F. Bohren, "Absorption and scattering of light by small particles," *Absorpt. Scatt. Light by small Part.*, 1983.

[108] G. Auer, W.-D. Griebler, and B. Jahn, "White Pigments," in *Industrial Inorganic Pigments*, Weinheim, FRG: Wiley-VCH Verlag GmbH & Co. KGaA, 2005, pp. 51–97.

[109] D. E. Chasan and G. Norwitz, "Infrared determination of inorganic sulfates and carbonates by the pellet technique," Philadelphia, 1969.

[110] Vicus Technologies LLC, "Development of Zinc Sulfide Seeker Window Material," Kennebunk, ME, 2005.

[111] M. D. Rintoul and S. Torquato, "Precise determination of the critical threshold and exponents in a three-dimensional continuum percolation model," *J. Phys. A. Math. Gen.*, vol. 30, no. 16, 1997.

[112] Z. Han and A. Fina, "Thermal conductivity of carbon nanotubes and their polymer nanocomposites: A review," *Prog. Polym. Sci.*, vol. 36, no. 7, pp. 914–944, 2011.

[113] W. Lv, S. Sultana, A. Rohskopf, K. Kalaitzidou, and A. Henry, "Graphite-high density polyethylene laminated composites with high thermal conductivity made by filament winding," *Express Polym. Lett.*, vol. 12, no. 3, pp. 215–226, 2018.

[114] J. C. Maxwell, *A Treatise on Electricity and Magnetism, Vol. I*, 3rd ed. Oxford University Press, 1904.

[115] SkyCool Systems Inc, "Technology - SkyCool Systems," 2021. [Online]. Available: https://www.skycoolsystems.com/.

[116] C. Feng *et al.*, "Bilayer porous polymer for efficient passive building cooling," *Nano Energy*, vol. 85, p. 105971, Jul. 2021.

[117] D. Aviv, M. Moradnejad, A. Ida, Z. Wang, E. Teitelbaum, and F. Meggers, "Hydrogel-Based Evaporative and Radiative Cooling Prototype for Hot-Arid Climates," no. June, pp. 279–286, 2020.

[118] A. Leroy *et al.*, “High-performance subambient radiative cooling enabled by optically selective and thermally insulating polyethylene aerogel,” *Sci. Adv.*, vol. 5, no. 10, pp. 1–9, 2019.

[119] S. Wilcox and W. Marion, “Users manual for TMY3 data sets,” Citeseer, 2008.

[120] X. Yin, R. Yang, G. Tan, and S. Fan, “Terrestrial radiative cooling: Using the cold universe as a renewable and sustainable energy source,” *Science*, vol. 370, no. 6518, pp. 786–791, 2020.

[121] E. Verploegen, O. Sanogo, and T. Chagomoka, “Evaluation of low-cost evaporative cooling technologies for improved vegetable storage in Mali,” in *2018 IEEE Global Humanitarian Technology Conference (GHTC)*, 2018, pp. 1–8.

[122] Radi-Cool, “Radiative Cooling Environment-Friendly Cooling Technologies with Zero Energy Consumption,” 2021. [Online]. Available: http://radi-cool.com/.

[123] SkyCool Systems Inc, “Using Sky Cooling to Increase Efficiency of Super Market Refrigeration Systems,” 2020.

[124] D. Kalyani, “IBISWorld Industry Report 44511 - Supermarkets & Grocery Stores in the US,” 2019.

[125] M. Deru *et al.*, “U.S. Department of Energy commercial reference building models of the national building stock,” *Publ.*, no. February 2011, pp. 1–118, 2011.

[126] M. C. Baechler, “High-performance home technologies: Guide to determining climate regions by county,” US Department of Energy, Energy Efficiency & Renewable, 2010.

[127] I. (ASHRAE) American Society of Heating, Refrigerating and Air-Conditioning Engineers, “2018 ASHRAE® Handbook - Refrigeration (SI Edition) - 15. Retail Food Store Refrigeration and Equipment.,” no. Ornl, 2018.

[128] I. (ASHRAE). (2020) American Society of Heating, Refrigerating and Air-Conditioning Engineers, “39. Condensers,” *2020 ASHRAE Handbook - HVAC Systems and Equipment (SI Edition)*, no. 1. American Society of Heating, Refrigerating and Air-Conditioning Engineers, Inc. (ASHRAE), 2020.

[129] I. Ekmekçi and K. Ermics, “Air cooled condensers and their effect on energy efficiency,” 2015.

[130] *ASHRAE Handbook - HVAC Systems and Equipment*. American Society of Heating, Refrigerating and Air-Conditioning Engineers, Inc. (ASHRAE)., 2020.

[131] I. H. Bell, J. Wronski, S. Quoilin, and V. Lemort, “Pure and Pseudo-pure Fluid Thermophysical

Property Evaluation and the Open-Source Thermophysical Property Library CoolProp," *Ind. Eng. Chem. Res.*, vol. 53, no. 6, pp. 2498–2508, Feb. 2014.

[132] I. (ASHRAE). (2020). American Society of Heating, Refrigerating and Air-Conditioning Engineers, "40. Cooling Towers," *2020 ASHRAE Handbook - HVAC Systems and Equipment (SI Edition)*, no. Figure 2. American Society of Heating, Refrigerating and Air-Conditioning Engineers, Inc. (ASHRAE), pp. 19–31, 2020.

[133] Baltimore Aircoil Company, "Evaporative Condenser Engineering Manual," 2021.

[134] F. Ran, D. Feldman, and R. Margolis, "U.S. Solar Photovoltaic System Cost Benchmark: Q1 2018," Golden, CO:, 2018.

[135] National Renewable Energy Laboratory, "PVWatts Calculator," *Version 6.1.4*. [Online]. Available: https://pvwatts.nrel.gov/. [Accessed: 15-May-2021].

[136] I. (ASHRAE). American Society of Heating, Refrigerating and Air-Conditioning Engineers, "2019 ASHRAE® Handbook Heating, Ventilating, and Air-Conditioning Applications (S-I Edition) - Chapter 50 - Water treatment: deposition, corrosion, and biological control," *American Society of Heating, Refrigerating and Air-Conditioning Engineers, Inc. (ASHRAE)*. pp. 1–24, 2019.

[137] D. Sickinger, O. Van Geet, S. Belmont, T. Carter, and D. Martinez, "Thermosyphon Cooler Hybrid System for Water Savings in an Energy-Efficient HPC Data Center: Modeling and Installation," Golden, CO, 2018.

[138] J. Mandal *et al.*, "Porous Polymers with Switchable Optical Transmittance for Optical and Thermal Regulation," *Joule*, vol. 3, no. 12, pp. 3088–3099, Dec. 2019.